Title: Paleoseismological constraints of the Anghiari normal fault (Northern Apennines, Italy) and potential implications for the activity of the Altotiberina low-angle normal fault

Authors: A. Testa[1]; P. Boncio[1]; S. Baize[2]; F. Mirabella[3]; S. Pucci[4]; B. Pace[1]; M. Riesner[5]; C. Pauselli[3], M. Ercoli[3], L. Benedetti[5], A. Di Chiara[4]; R. Civico[4]

Affiliations:

1. Department of Engineering and Geology, Università degli Studi G. d'Annunzio Chieti e Pescara, Italy.
2. IRSN/PSE-ENV/SCAN/BERSSIN, Institut de Radioprotection et de Sureté Nucléaire, Fontenay-Aux-Roses 92262, France..
3. Dipartimento di Fisica e Geologia, Università di Perugia, Italy.
4. Istituto di Geofisica e Vulcanologia, Via di Vigna Murata 605, 00143 Rome, Italy.
5. University of Aix Marseille, CNRS, IRD, INRAE, CEREGE, Aix-en-Provence, France

Key words: Northern Apennines, extensional tectonics, paleoseismology, capable faults, low angle normal fault.

Key points:

- Revealed the Late Pleistocene - Holocene slip history of the Anghiari fault, considered a synthetic splay of a low-angle normal fault.
- The capability of the Anghiari fault to rupture the surface during M>6 earthquakes has been ascertained.
- The results have potential implications for the activity and seismogenic behavior of a continental low-angle normal faults.

Abstract: The NE-dipping Anghiari normal fault (AF), bounding to the west the Sansepolcro basin in the Upper Tiber Valley (northern Apennines), is supposed to be a synthetic splay of the

Altotiberina (ATF) low-angle normal fault (LANF), an active ENE-dipping extensional detachment whose seismogenic behavior is debated.

In order to assess the AF capability to break the surface during strong earthquakes and be the source of historical earthquakes, we acquired high resolution topographic data, performed field survey and geophysical investigations (Seismic reflection, Ground Penetrating Radar (GPR), Electrical Resistivity Tomography (ERT)) and dug three paleoseismological trenches across different fault sections of the AF.

The acquired data reveal for the first time the Late Pleistocene to historical activity of the AF, constraining the age of seven paleo-earthquakes over the last 25 ka, the youngest of which is comparable with one of poorly constrained historical earthquakes of the Sansepolcro basin. The yielded slip rate is > 0.2 mm/yr averaged over the last 25 ka and the recurrence interval is about 2500-3200 years. The magnetic susceptibility analysis in one of the trenches indicates continuous extensional stress field across the entire trenched stratigraphy.

Our results confirm the ability of the AF to nucleate surface faulting earthquakes and suggest that the ATF (LANF) could have a seismogenic behavior, generating M>6 earthquakes, if the AF is soling at depth into the LANF.

Plain Language Summary: In this study we analyzed the capability of the Anghiari fault (Upper Tiber Valley, Northern Apennines of Italy) to reach and break the topographic surface during a strong earthquake. This fault belongs to the Altotiberina low-angle normal fault (ATF), a detachment fault accompanied by a system of synthetic splays whose seismogenic behavior is still debated because of a lack of seismological and paleoseismological data. Thanks to geological, morphotectonic and geophysical analyses, four sites have been selected for paleoseismological investigation.

The paleoseismological data revealed the seismic history of the Anghiari fault, assessing its capability to recurrently break the surface during strong earthquakes.

In addition, an analysis of the anisotropy of the magnetic susceptibility performed in one of the paleoseismological trenches indicates that the stress field was extensional, acting continuously during the sedimentation of the entire trenched stratigraphy.

Our results suggest that the AF is capable to break the surface during strong earthquakes. This has potential implications on the seismogenic behavior of the ATF low-angle normal fault, as the strong earthquakes should nucleate on the low-angle fault plane if the AF is soling at depth into that detachment.

1. Introduction

The NE-dipping Anghiari normal fault (AF) is the northernmost part of the Anghiari-Città di Castello main fault which bounds the western flank of the Sansepolcro basin (Upper Tiber Valley, Northern Apennines of Italy).

The AF is featured by the greatest evidence of recent activity as it raises Early-Middle Pleistocene continental deposits in its foot-wall in correspondence of the Anghiari ridge (Fig. 1) The faults belonging to the Sansepolcro basin fault system are supposed to be synthetic and antithetic splays of the debated Altotiberina (ATF) low-angle normal fault (LANF) (Fig. 1), considered as a major engine of the extension in the Upper Tiber Valley (UTV) (Boncio et al., 2000; Chiaraluce et al., 2007; Delle Donne et al., 2007; Brozzetti et al., 2009; Pucci et al., 2014). The ATF is among one of the worldwide potentially active continental LANFs (Webber, 2018), deserving the developments of a Near Fault Observatory (NFO) long term research infrastructure (https://www.epos-eu.org/tcs/near-fault-observatories/about).

The complex seismotectonic context of the UTV is emphasized by Brozzetti et al. (2009) who highlighted the different behavior between the northern sector, corresponding to the Sansepolcro

basin, and the southern sector, corresponding to the area SSE of Città di Castello. The occurrence of strong (M>5.5) earthquakes in historical times suggests that it is possible to find geological evidence of either primary (i.e., tectonic surface ruptures) or secondary (i.e., shaking-induced features) evidence of past earthquakes (McCalpin, 2009). However, paleoseismologic studies aimed at discovering chronologically constrained field evidence of prehistoric strong surface rupturing earthquakes related to the Sansepolcro basin fault system are still missing. Only a few tectonic geomorphology and Quaternary geology studies (Cattuto et al., 1995; Sani et al., 2009; Pucci et al., 2014; Benvenuti et al., 2016;), locally implemented with near-surface geophysical investigations (Delle Donne et al., 2007), are available.

Since the morphotectonic expression of the Anghiari fault is pronounced, we focused on this latter, in order to investigate its capability to break the topographic surface during strong earthquakes. We performed detailed geological and geomorphological mapping of the Anghiari fault by means of traditional field work and digital topographic data, including high-resolution digital surface model (DSM) from satellite imagery and local very high-resolution LIDAR digital terrain model (DTM). Near-surface geophysical techniques including Seismic Reflection (SR), Ground Penetrating Radar (GPR) and Electrical Resistivity Tomography (ERT) were used to plan and accurately locate the sites for paleoseismological trenching and analysis.

In this paper we will show present evidence of the Anghiari fault activity, data on its discrete, recurrent surface faulting events, likely associated with large earthquakes. The implications for the activity and seismogenic behavior of a continental LANF are also discussed.

2. Geological and seismotectonic setting

2.1. Geological background

The Northern Apennines are a NE-verging fold-and-thrust belt resulting from the overlapping of different tectonic units during the Miocene. From west to east, the involved units are the ophiolite-

bearing Ligurian unit, the Tuscan unit, and the inner and outer Umbria units (Pialli et al., 1998; Brozzetti et al., 2009; Barchi, 2010). Since the Late Pliocene, the resulting compressional structures have been superimposed by an extensional phase driven by an eastward-propagating set of low-angle detachments dipping ENE, imaged by seismic reflection profiles (e.g., CROP 03, Pialli et al., 1998). The youngest and still active fault is the ATF, a ~70 km-long structure dipping 15°–20° which bounds the western flank of the Quaternary UTV (Barchi, 2010). The ATF has accumulated up to 10 km of extension since the Pliocene (Mirabella et al., 2011; Caricchi et al., 2015). GPS data reveal 2-3 mm/yr of present-day extension rate across the entire extending Apennines (Serpelloni et al., 2005; Mantenuto, 2008; D'Agostino et al., 2009; Hreinsdóttir & Bennett, 2009; Bennett et al., 2012). This is similar to the long-term geologic slip rate of the ATF (2.7 mm/yr Mirabella et al., 2011). The most recent synthetic splays of the ATF appear to be segmented by step-over relay zones that separate three tectonically-controlled Quaternary basins, the northernmost of which is the Sansepolcro basin (Fig.1), characterized by a more intense Quaternary normal fault activity, in particular along the Anghiari fault (Pucci et al., 2014).

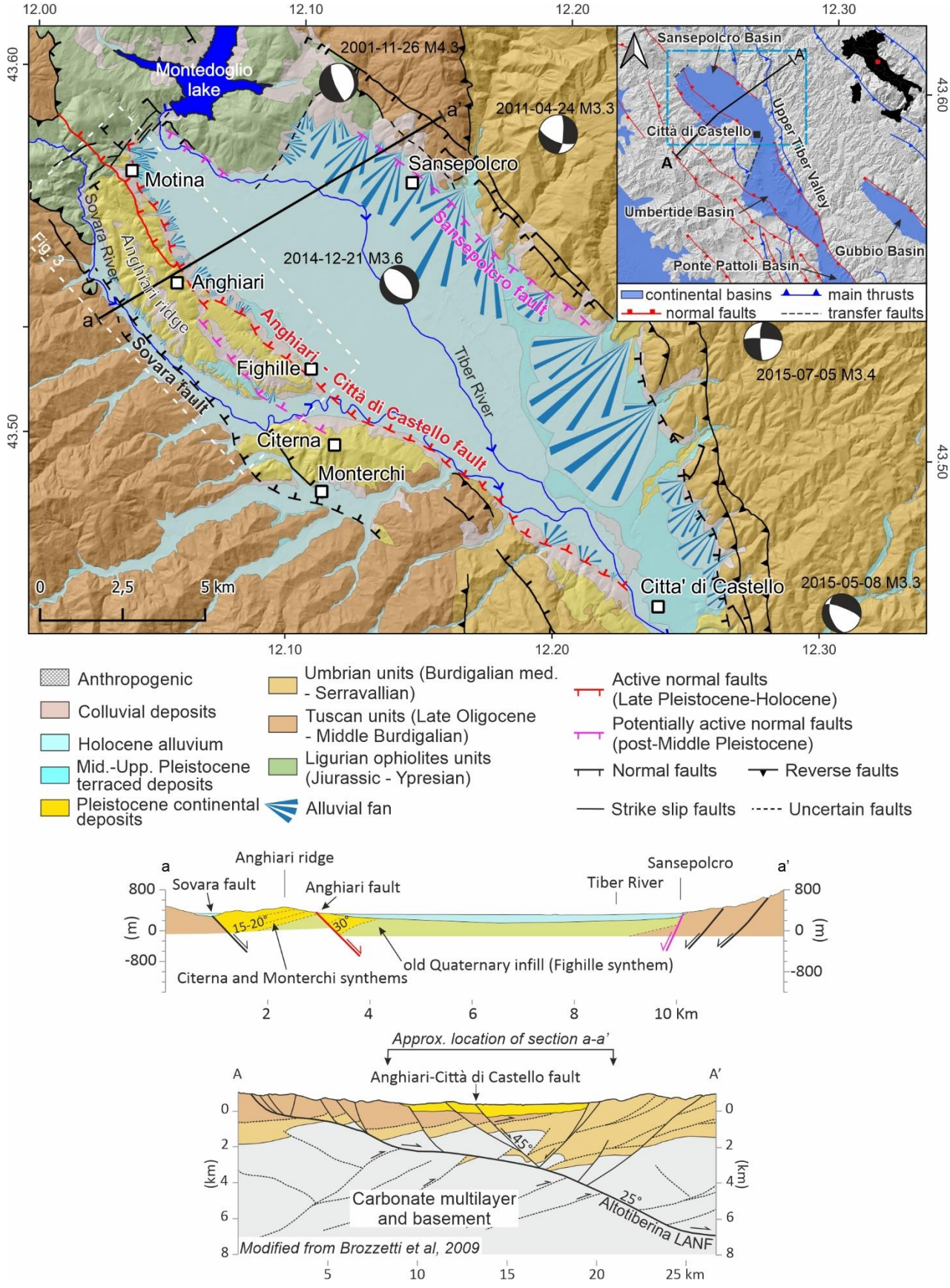

117

118 Fig. 1. Simplified geological map of the Sansepolcro basin showing the main tectonic units, the distribution of the

continental Pleistocene-Holocene deposits and the trace of the main faults. The faults affecting Upper Pleistocene-Holocene deposits are defined as active faults, while the faults displacing Middle Pleistocene deposits or morphologies, without more tightening age constraints, are defined as potentially active. The focal mechanisms are taken from RCMT (available at http://rcmt2.bo.ingv.it/ last access Nov. 2022) and TDMT catalogs (available at http://terremoti.ingv.it/tdmt last access Nov. 2022). The geological setting of the basin at shallow depth is shown in the cross-section a-a'. The regional cross-section A-A', derives from the deep seismic line CROP3 (Barchi et al., 1998a), modified from Brozzetti et al. (2009). The inset shows the location of both geological map and trace of section A-A', along with the main tectonic features and basins of the Upper Tiber Valley.

The Sansepolcro basin is an asymmetric graben primarily controlled on the SW flank, by the NE-dipping Anghiari-Città di Castello main fault and bounded, to the NE, by a SW-dipping antithetic normal fault (Sansepolcro fault). This basin is infilled by a ~1.0-1.2 km-thick continental succession (Barchi & Ciaccio, 2009; Mirabella et al, 2011; Pucci et al, 2014) (Fig. 1).

The Sansepolcro basin exposes mainly Holocene alluvial sediments within the valley, with outcrops of Pleistocene deposits found mainly along its western side at the normal faults footwall (Fig.1). The Quaternary continental deposits are made up of fluvio-lacustrine units, unconformable covered by Middle Pleistocene to Holocene alluvial and colluvial deposits (ISPRA, 2011).

The Paleo Tiber River and its western and eastern tributaries fed the Sansepolcro basin with a Quaternary deposition dominated by a fluvial-lacustrine/palustrine paleo-environment. Since the Lower Pleistocene the opening of a wide extensional graben caused large infill of fine-grained sediments in the depocenter and coarse sediments along its margins. In the Middle Pleistocene the extensional activity started exhume the Anghiari ridge, with consequent interruption of the western outflow and, determining the current basin physiography (Cattuto et al., 1995). Then, the drainage of the basin has been affected also by the activity of the SW-NE striking faults that bound the basin to the north, with consequent anomalies in the hydrographic network, such us fluvial deviations, of the Tiber and Sovara Rivers (Cattuto et al., 1995; Benvenuti et al., 2016; Sani et al., 2009). After the

145 Middle Ages anthropogenic channeling shifted further east the Tiber River thalweg from the foot of
146 the Anghiari ridge (Cattuto et al., 1995).

147 There are no chronologic constraints for the sedimentary units infilling the basin, therefore
148 the unit ages and the stratigraphic frame is not univocal in the literature (e.g., ISPRA, 2011; Pucci et
149 al., 2014; Benvenuti et al., 2016). In this paper, we follow the basic stratigraphic frame defined in the
150 1:50,000-scale geologic map of Italy, consisting of three Pleistocene synthems (i.e., unconformity-
151 bounded stratigraphic units) (Fighille: FIG, Citerna: CTA and Monterchi: MTC) covered by Middle
152 Pleistocene to Holocene alluvial and colluvial deposits (ISPRA, 2011).

153 The oldest outcropping continental deposits belong to the Fighille synthem. It consists of
154 massive or planar-laminated clay and silt, with subordinate sandy and gravelly layers, deposited in a
155 fluvial-lacustrine/palustrine environment (i.e., periodically flooded alluvial plain, with ponds,
156 wetlands, rare braided streams, and alluvial fans) characterized by alternating dry and humid climate.
157 The clayey silts contain abundant plant remains, peats and lignite levels and calcareous nodules. The
158 Fighille synthem is at least 120 m-thick (the bottom never crops out) and is tilted westward (up to 25°
159 in the southern Anghiari ridge; Fig. 1). Its deposition started before 1.8 Ma, given the mollusk
160 assemblage and mammal faunas (late Villafranchian; Ciangherotti & Esu, 2000; Argenti, 2004;
161 Masini & Sala, 2007).

162 The Citerna synthem is characterized by coarse-grained facies association, with clast-
163 supported gravels in a sandy matrix, sand lenses and layers, clay lenses, and buried red paleosols of
164 a braided fluvial plain environment. In the footwall of the Anghiari fault, the Citerna beds are tilted
165 westward 15-20°, on average, while in the hanging wall of the fault the dip can be as high as ~30°
166 (see section a-a' in Fig. 1). The thickness of the unit is estimated in this work to be $\geq$ 150 m. Due to
167 the absence of radiometric dating, its age is inferred to be Early Pleistocene (Pucci et al., 2014) or
168 Middle Pleistocene (Benvenuti et al., 2016) only on the basis of stratigraphic relationships.

169 The Pleistocene fluvio-lacustrine sequence is closed upwards by the Anghiari sub-synthem
170 (member of the Monterchi synthem) which is made of reddish clayey silts, fine sands, and gravel
171 layers made of arenaceous, calcareous, and immature siliceous clasts. The thickness of the Anghiari
172 sub-synthem is estimated in this work to be in the order of 20-25 m, and the beds are tilted westward
173 5-10°. The top of this unit is highly weathered and presents stacks of paleosols with Mg-Fe-oxide
174 nodules and carbonate nodules, suggesting an alluvial environment affected by frequent subaerial
175 exposures during interglacial periods. Cattuto et al. (1995) suggested that the paleosol could be
176 formed during the Mindel-Riss interglacial, but a different age cannot be excluded, as there are no
177 chronological constraints for the age of the Anghiari sub-synthem and the overlying paleosols.
178 The Middle Pleistocene (upper part) to Late Pleistocene and Holocene alluvial deposits,
179 mostly made of gravels and sands, include terraced fluvial sediments of the Sovara and Tiber Rivers
180 and alluvial fans of variable thickness. Their age is constrained by morpho-stratigraphic relations
181 with the older units, by sparse radiocarbon dating and by archaeological constraints (Benvenuti et al.,
182 2016).
183 The deposition inside the Upper Tiber Valley has been influenced by the interaction between
184 regional uplift and tectonic subsidence. The geological and geomorphological evidence for
185 Quaternary activity along the UTV is concentrated within the Sansepolcro basin, where NE-dipping
186 splays reach the surface and bound to the west the Quaternary, fluvio-lacustrine deposits (Barchi et
187 al, 1998b; Boncio et al, 2000; Martini et al, 2001; Barchi e Ciaccio, 2009; Sani et al, 2009; Pucci et
188 al, 2014) (Fig. 1). In particular, the tectonic evidence consists of morphological fault scarps affecting
189 the Quaternary deposits, back-tilted Pleistocene alluvial terraces and syn-tectonic sedimentary
190 wedges that have been imaged by shallow high-resolution seismic profiles (Cattuto et al., 1995, Delle
191 Donne et al., 2007, Brozzetti et al., 2009). According to Pucci et al. (2014), the Sansepolcro basin
192 presents a lower vertical incision and elevated aggradation with respect to the southern basins,
193 suggesting that the subsidence rate, controlled by the Sansepolcro basin fault system, strongly

194 counteracts the regional uplift rate, as documented by the limited distribution of erosive forms such
195 as fluvial terraces (see Fig. 1). The main NE-dipping faults are the Sovara fault and the Anghiari -
196 Città di Castello main fault. The Sovara fault juxtaposes the pre-continental deposits bedrock to the
197 Pleistocene continental units, bounding the western side of the basin, along the Sovara River valley
198 (Fig. 1), and is presently buried under the Holocene alluvial deposits of the Sovara River. Present-
199 day extension is accommodated by the Anghiari - Città di Castello main fault: it is a >20 km-long
200 NE-dipping normal fault including two NW-SE aligned faults, the Anghiari fault to the north and the
201 Città di Castello fault to the south, separated by the Sovara River Valley (Fig. 1) (Testa et al., 2021).
202 The average throw-rate of the Anghiari fault was inferred to be ~0.25 mm/yr since the Middle
203 Pleistocene, derived by the interpretation of a seismic reflection profile (Delle Donne et al., 2007),
204 whilst 0.6-0.8 mm/yr was inferred for the Late Quaternary period based on the tilting of a fluvial
205 terrace tread (Brozzetti et al., 2009). None of those numbers have been constrained by faulted dated
206 markers (Fig. 1).
207
208 **2.2. Seismicity and seismotectonic**
209 Active extension across the Upper Tiber Valley is indicated by geodetic data (D'Agostino et
210 al., 2009) and earthquake focal mechanisms (Pondrelli et al., 2002) (Fig. 1). The area of maximum
211 extension is concentrated across a 30–40 km-wide zone where the strongest tectonic moment is
212 released (D'Agostino et al., 2009). The correlation between the present extensional tectonics and the
213 activity of the NE-dipping ATF is widely agreed in the literature (e.g., Barchi et al., 1998a; Boncio
214 et al., 2000; Piccinini et al., 2003; Chiaraluce et al., 2007; Mirabella et al., 2011; Pucci et al., 2014;
215 Anderlini et al., 2016; Gualandi et al., 2017; Valoroso et al., 2017). Based on the distribution and
216 characteristics of the instrumental and historical seismicity, two sectors of the ATF were identified
217 along the UTV and east of it: the northern sector, corresponding to the Sansepolcro basin studied in
218 this paper, and the southern sector, SSE of Città di Castello.

219 The southern sector is characterized by diffuse, frequent microseismicity, located along the
220 zone around the ATF and within the ATF hanging wall, including doublets of repeating
221 microearthquakes, aseismic slip and small-magnitude slow-slip events (Piccinini et al., 2003,
222 Chiaraluce et al., 2007; Gualandi et al., 2017; Valoroso et al., 2017). Here, the most energetic
223 earthquakes are expected to be released by SW-dipping, NW-SE-striking antithetic normal faults
224 (e.g., the Gubbio normal fault, Mirabella et al., 2004; Pace et al., 2006) (Fig. 1). The northern sector,
225 i.e., the Sansepolcro basin, is characterized by much lower microseismicity activity, compared to its
226 southern counterpart, and was struck by several destructive historical earthquakes (Fig. 2). This has
227 been interpreted as the evidence that this segment is locked (Brozzetti et al., 2009), and supposedly
228 slipping during moderate to large earthquakes that nucleate at shallow depths on steeper ramps (25-
229 30°) of the ATF and/or on high-angle synthetic splays. In particular, the ATF ramp at 3-7 km-depth
230 and its continuation up to the surface along the Anghiari fault (see section A-A' in Fig. 1) has been
231 considered as the major potential seismogenic source of the area (named Città di Castello in Brozzetti
232 et al., 2009).
233 Dense network of GPS data, yield ~2-2.5 mm/yr of extension driven by the ATF, mostly
234 accommodated with creep below depths of 4-5 km (H Hreinsdóttir and Bennett, 2009; Anderlini et
235 al., 2016 The modeled geodetic strain (Anderlini et al., 2016) suggest that the ATF is mainly locked
236 down to 4-5 km of depth, whereas creeps at a rate of 1.7±0.3 mm/yr between 4-5 and 7 km, with a
237 deep locked patch between 7 and 10 km. According to Anderlini et al. (2016), one of the main shallow
238 locked patches is in the Sansepolcro basin. The main creeping portion correlates well with the area
239 of intense microseismicity SSE of Città di Castello. Such a fault architecture and slip behavior
240 produce a positive stress build up on the shallow locked portion of the ATF, and on most of the
241 hanging wall splays, including the Anghiari fault. Based on the size and Strain rate of the inferred
242 locked patches, Anderlini et al, (2016) estimated a seismic potential of the ATF up to Mw 6.5-6.7

over a time interval of 10^3 years. On the other hand, seismic slip on hanging wall splays might favor potential seismic slip or transient acceleration of creep on deeper portions of the ATF.

Figure 2 shows the epicentral macroseismic intensities of the earthquakes that hit the Sansepolcro basin in the past centuries. The main events ($M_w \geq 5.5$) are the 1352 (M_w 6.3, Mercalli-Cancani-Sieberg macroseismic intensity - I_0 - IX-X), 1389 (M_w 6.0, I_0 IX), 1458 (M_w 5.8, I_0 VIII-IX), 1789 (M_w 5.8, I_0 X), 1917 (M_w 6.0, I_0 IX-X) earthquakes (Rovida et al, 2022). Other significant events ($5 \leq M_w \geq 5.5$) are the 1489 (M_w 5.1, I_0 VII), 1558 (M_w 5.1, I_0 VII) and 1919 (M_w 5.0, I_0 VI) earthquakes (Rovida et al, 2022). Based on the distribution of the intensity data points, Brozzetti et al. (2009) proposed that the 1389, 1458 and 1789 could have nucleated on the southern sector of the Anghiari-Città di Castello main fault, while the 1917 Monterchi earthquake could have nucleated on a western and shallower synthetic splay of the ATF. Similarly, as possible evidence of NE-dipping source of the 1917 earthquake, Delle Donne et al. (2007) consider as primary surface faulting the ~1 km-long, NW-SE-striking coseismic ground failure occurred near Monterchi and described by Oddone (1918) (although the latter did not exclude its landslide genesis). A different interpretation of the 1917 earthquake is proposed by Caciagli et al. (2019), who reanalyzed instrumental historical data and calculated a relatively deep hypocentral location (~8±4 km-depth), a relatively high magnitude (Mw 5.8) and a first-arrival focal solution. The most plausible solution proposed by these authors is a NE-striking right-lateral strike-slip fault in the footwall of the ATF, possibly related to a transfer fault responsible for the segmentation of the ATF.

None of the seismotectonic interpretations mentioned above is constrained by paleoseismological evidence in historical or Holocene layers that might prove the activity of the fault(s) up to the surface.

In this paper we present constraints on the Late Pleistocene and Holocene activity of the Anghiari fault.

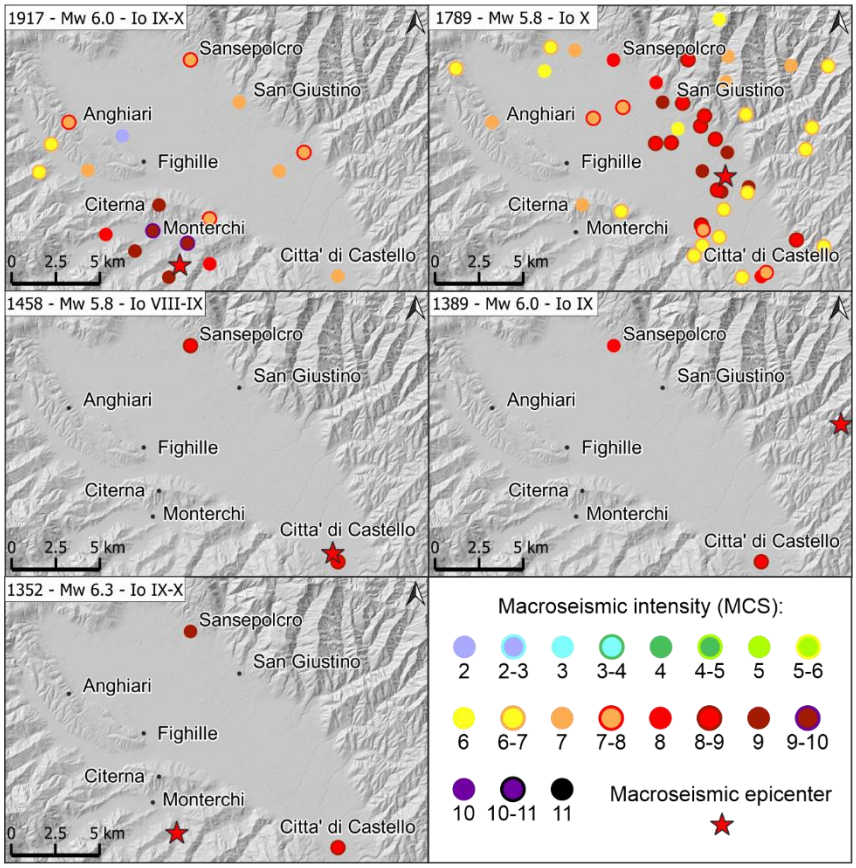

Fig. 2. Distribution of the macroseismic intensities related to the main historical earthquakes ($M_w \geq 5.5$) occurred in the Sansepolcro basin. In detail the following events are represented in order: 1917 (M_w 6.0, Mercalli Cancani Sieberg macroseismic intensity I_0 IX-X); 1789 (M_w 5.8, I_0 X); 1458 (M_w 5.8, I_0 VIII-IX); 1389 (M_w 6.0, I_0 IX); h) 1352 (M_w 6.3, I_0 IX-X) (Rovida et al, 2022).

3. Methods

3.1. Field and remote sensing surveys

Field investigations and geological and geomorphological mapping were carried out along the eastern side of the Anghiari ridge in order to map the surface trace of the Anghiari fault as well as to identify faulted stratigraphic and topographic markers constraining the fault slip history and slip rate. Most of the geologic and geomorphic features such as fault traces and the contacts of Quaternary geological bodies were identified integrating both conventional field mapping and remote sensing

techniques: the former was performed using a field tablet integrating a commercial GPS device and a dedicated digital mapping suite (Field Move Software Suite, Petroleum Experts); the latter included the acquisition and analysis of LiDAR data, airborne-acquired through a Riegl miniVUX Sys DL laser scanner mounted on a DJI Matrice 600 pro drone. This acquisition produced a dense point cloud (300 pts/m^2) from which a very high-resolution Digital Terrain Model (DTM) (0.2-m pixel size) of 1.45 $km^2$was built. Then, the derivatives shaded relief, slope and aspect maps, were jointly and carefully analyzed (Figure 4). Moreover, at the scale of the Sansepolcro basin we used the 10 m resolution TINITALY Digital Elevation Model (DEM) (Tarquini et al., 2012) and a newly acquired Digital Surface Model (DSM) derived from stereo pairs of Pleiades satellite optical images (50 cm resolution).

3.2. Geophysical investigations (GPR, Seismic, ERT)

Following the field and geomorphological mapping, we carried out a geophysical campaign aimed at determining the most accurate position of the fault traces which could be the target for paleoseismological trenching. Across some site with morphological fault expressions, we have used/combined high-resolution seismic reflection (SR), ground-penetrating radar (GPR) and electrical resistivity tomography (ERT) acquisitions. Among the acquired datasets, here we present only the results achieved combining high-resolution SR and GPR at the Villa Sterpeto site (location in Fig. 3 and 4) and the ERT at the Anghiari site A (location in Fig. 4), surveyed at the paleoseismological investigation area and at the paleoseismological trench floor.

The SR profile was 167 m-long, ~58°N oriented, and acquired across the scarp between the slope made of Citerna synthem and the paleo-surface curved on the Anghiari sub-synthem.

A 24-bit DoReMi seismograph, manufactured by SARA Electronic Instruments (https://www.sara.pg.it) and equipped with 72 channels linked to vertical geophones (40 Hz), was

used for the acquisition of P-waves. The geophone spacing was set up to 1 m and thus 0.5 m was the CDP spacing. To increase the resolution along the near surface portion of the seismic section, a GPR profile 62 m-long and ~67°N oriented was collected crossing the possible fault trace, aiming to better constrain the fault geometry at shallow depth. The GPR line was recorded using a Zond-12e GPR system, equipped with a 100 MHz antenna (Tx and Rx), using a survey wheel and Topcon GR-5 GNSS device in NRTK configuration, to record the coordinates and elevation of each trace. Despite the clear high conductivity of the soil at the study site, limiting the probing depth to ~2 m, the processed GPR profile shows an improved image of the shallow geometries. The processed SEG-Y files were finally imported in the seismic interpretation software OpendTect Pro v.6.4 (academic license courtesy of dGB Earth Science, https://www.dgbes.com, last access: 3 January 2023) for an enhanced display obtained by the calculation of selected seismic attributes (Taner, 1979) computed on the GPR signal amplitude and phase, already proven to be effective detecting fractures and faults (Forte et al., 2012; Ercoli et. al., 2015). In particular, the instantaneous phase (Cinti et. al., 2015) enhances the interpretability of the reflections' geometry and the enhancement of lateral discontinuity. Being independent on the reflection strength, this attribute is also effective in strongly attenuated areas characterized by weak reflectivity (Ercoli et al., 2021a), thus propaedeutic for ground truthing. The latter aids not only the stratigraphic interpretation but also enhances lateral geophysical discontinuities associable to shallow fracturing and/or faulting.

A MAE XM612EM+ equipment has been used to acquire an ERT profile along the floor of the trench Anghiari site A, with a maximum electric voltage of 200V and a minimum electricity of 150 mA. The resulting resistivity profile has a maximum depth of 7-8 m and a spatial resolution of 0.5.

Further details about the acquisition and processing of the geophysical analysis are given in the supporting information (Text S1).

3.3. Paleoseismological trenching

The paleoseismological investigations were conducted between winter 2021 and summer 2022 in two sites across the Micciano fault section (Villa Sterpeto, Podere Todari sites) and two sites across the supposed trace of the Anghiari-Motina fault section (Anghiari sites A and B) (Figure 4). First we dug by backhoe a semi-benched trench, 60°-trending, 50 m-long and 3 m-deep at the Villa Sterpeto site, across the fault trace highlighted by the high-resolution SR and GPR data interpretation.

At the Podere Todari site, we widened and rectified by backhoe a pre-existing, 80°-trending anthropogenic roadcut exposing faulted colluvial deposits across a synthetic splay of the Micciano fault section. The wall of the rectified roadcut was 7 m-long and 2.5 m-high.

Finally, we dug two trenches by backhoe at the Anghiari sites A and B across the supposed trace of the Anghiari-Motina fault section. The trench of site A was 50°-trending, 55 m-long, 3 to 4 m-deep, with a benched layout. The trench of site B was 60°-trending, 40 m-long, 3 m-deep, with a benched layout. The location of the trench Anghiari Site A was chosen based on an outcrop of the Citerna synthem at the base of the scarp below the road S.P. 47 suggesting that the scarp is in the footwall of the fault and that the fault is located a few meters downslope. The location of the trench Anghiari site B would have to cross the supposed trace of the Anghiari-Motina fault section in order to compensate for the lack of unequivocal evidence in the site A. However, this trench is completely located within the hanging wall of the fault.

In all the four sites, the trench walls were accurately smoothed and cleaned. The faults and the main stratigraphic contacts were identified, flagged with colored pins, and logged. Wall logs were drawn at 1:50 scale for Villa Sterpeto and Anghiari sites and 1:20 scale for Podere Todari site. As a basis for the wall logs, four orthophotomosaics were generated from ground-based 24-megapixel imagery, acquired using a Canon 850d camera, and processed by structure-from-motion photogrammetry through Agisoft Metashape®. High-resolution orthophotomosaics are reported in supporting information (Figures S1, S2, S3 and S4).

In order to constrain the age of the earthquakes we performed a Bayesian analysis in OxCal v4.4.4 (Bronk Ramsey, 1995 and 2009; atmospheric calibration model by Reimer et al., 2020) using the Boundary-Zero Boundary model (Bronk Ramsey, 2008). This approach allowed us to compute the probability density function for the ages of the events, forcing the model to skew the age based on geological evidence interpreted as developed immediately before (i.e., earthquake horizons) or immediately after (colluvial wedges) the earthquakes. Therefore, the earthquake ages computed using OxCal are narrower than the time windows between each couple of samples, and the probability density function has a skewness through the sample that, according to our interpretation, fits much better with the age of the events.

3.4. Sample dating

We collected 18 samples from paleoseismological trenches for radiocarbon dating, 8 at the Villa Sterpeto, 6 at the Todari, and 4 at the Anghiari A sites. Charcoal was found and dated in 3 samples (Anghiari site A), the other samples consist of organic sediment, for which we dated the bulk organic fraction. The radiocarbon dating was performed with accelerator mass spectrometry technique in the laboratories of Beta Analytic for 13 samples (https://www.radiocarbon.com/, last access: 26 August 2022) and in the Laboratory Plateforme Nationale LMC14, France (http://lmc14.lsce.ipsl.fr/, last access: 21 March 2022), for 5 samples (complete list of the samples and samples age in Tab. 1). The uncalibrated ages given from the LMC14 laboratory were calibrated by us using the IntCal20 atmospheric calibration model (Reimer et al., 2020) in OxCal. The original reports of the dating, and the results of the calibration (referring to the samples dated in the Laboratory Plateforme Nationale LMC14) are reported in the additional supporting information.

The age of six pottery shards collected in the Anghiari site A trench was estimated by O. Menozzi, archeological expert of the University of Chieti - Pescara (personal communication).

3.5. Anisotropy of magnetic susceptibility

The anisotropy of magnetic susceptibility (AMS) can be used as a proxy for rock fabrics (Hrouda, 1982; Borradaile, 1988; Tarling & Hrouda, 1993; Borradaile & Henry, 1997; Borradaile & Jackson, 2004), reflecting the preferred orientation of grains, grain distributions and/or the crystal lattices of minerals that contribute to the magnetic susceptibility of a rock (e.g., Tarling & Hrouda, 1993; Borradaile & Jackson, 2004).

In particular, AMS is extremely sensitive to incipient strain in fine-grained sediments well before other macro and mesoscopic strain features (such as cleavage) can be observed in the field. In general, in compressive tectonic settings, the magnetic lineation (the maximum susceptibility axis) is commonly parallel to fold axes and thrust faults, while in extensional regimes, it is perpendicular to normal faults and parallel to bedding dip directions (e.g., Borradaile & Jackson, 2004; Maffione et al., 2012).

In order to understand the relations between these units and the fault activity, the anisotropy of the magnetic susceptibility (AMS) of clay layers, the paleosol and the colluvial deposits was investigated in the Villa Sterpeto trench. Eight blocks were collected using a Bosch Professional 18V System GOP multitool. Each block was oriented with a Brunton magnetic compass and extracted, numbered from 1 to 8, where the latter is the closest to the fault in the Villa Sterpeto trench. Blocks ANG01 to 05 were collected in clays, ANG06 and 07 on the paleosol and ANG08 on the colluvial deposits. From each block, 5 to 8 oriented ~1.5 cm^3 cubes were cut using a diamagnetic saw, in the rock preparation laboratory at INGV, Rome. For each of the 50 samples, the bulk susceptibility and the low field AMS was measured on all samples on a AGICO KLY-3S Kappabridge and the results were processed using the AGICO software Anisoft (https://www.agico.com/text/software/anisoft/anisoft.php). Further information about this methodology is given in Supporting Information (Text S2)

4. Results

4.1. Anghiari fault from geological and geomorphological mapping

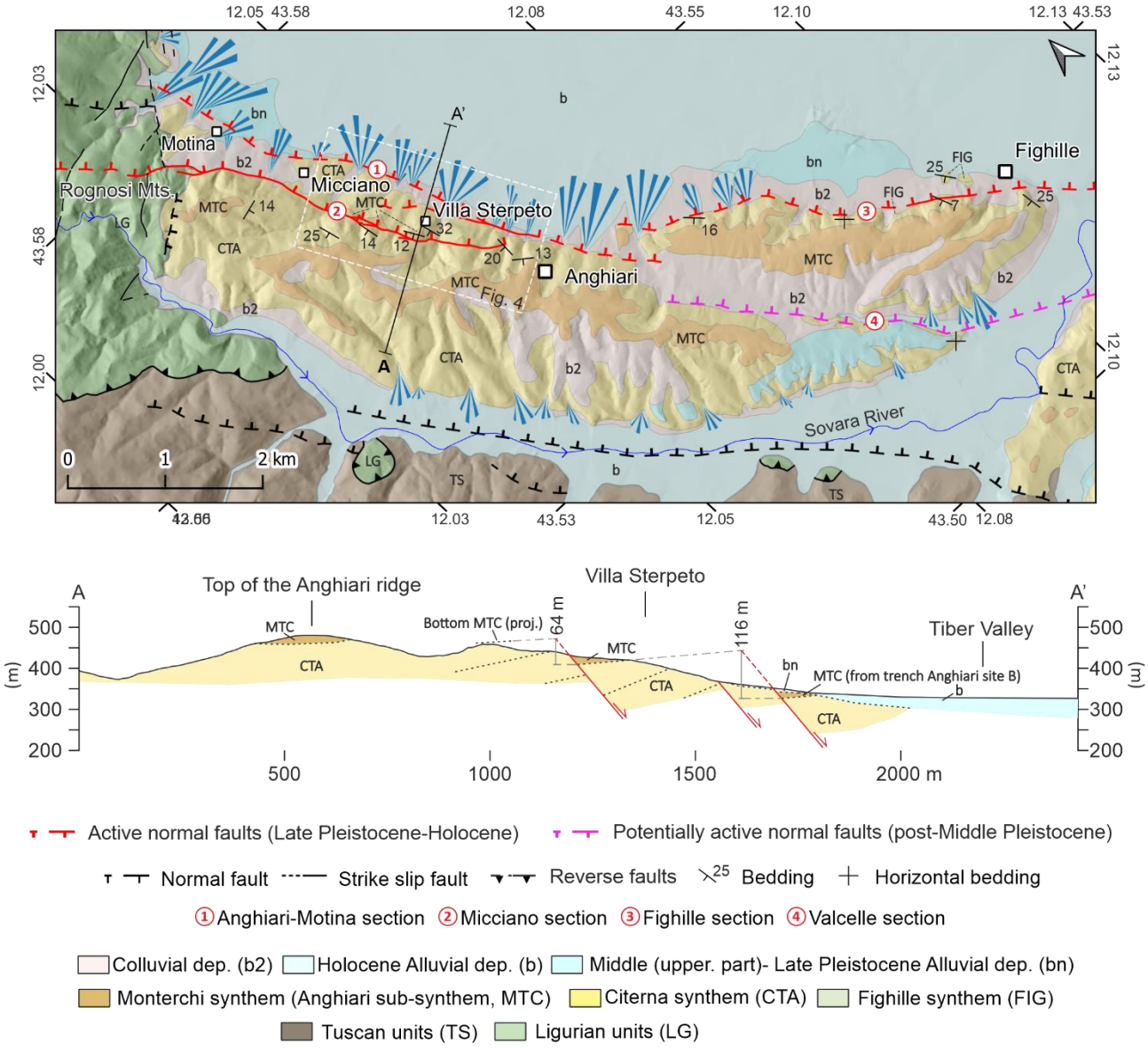

Fig. 3. Detailed geological map of the Anghiari ridge showing the distribution of the main geologic units and the segmentation of the Anghiari fault, based on ISPRA (2011) and integrated with original field survey. The measured displacement of each segment of the Anghiari fault is shown in the geologic cross section A-A' (no vertical exaggeration). Dashed lines indicate buried or inferred fault traces. See the caption of Fig. 1 for the definition of active and potentially active faults. The white dashed square indicates the location of the map in figure 4.

409 The Anghiari normal fault is characterized by a segmented pattern in map view, formed by at
410 least four fault sections, namely the Anghiari-Motina, Micciano, Fighille and Valcelle sections (1,2,3
411 and 4, respectively, in Fig. 3).

412 The 5.5 km-long Anghiari-Motina section bounds the eastern side of the Anghiari ridge,
413 separating the Citerna synthem (CTA) in the footwall from the Holocene colluvial and alluvial
414 deposits in the hanging wall. The fault trace is barely visible in the field and is often concealed by
415 anthropogenic modifications. Its trace was mapped using first-order morphological evidence, such as
416 escarpments on the CTA sediments uplifted in its footwall block, and the alignment of apexes of the
417 youngest generation of alluvial fans developing in its hanging wall. The fault location is further
418 constrained by data acquired within trenches A and B near Anghiari. The average strike of the
419 Anghiari-Motina section is N150. A 1.5 km-long, WNW-striking secondary splay (Fig. 4), crossed
420 by the geologic section in Fig. 3, branches out from the principal fault trace and displaces some
421 paleosurfaces located between the Anghiari-Motina and Micciano fault sections.

422 The 6 km-long Micciano section runs within the Anghiari ridge, from the Rognosi Mts. to the
423 northern part of the Anghiari town. In its northern sector, the fault separates the Meso-Cenozoic
424 bedrock (Ligurian units) from the Lower-Middle Pleistocene CTA unit and then continues to the NW
425 within the bedrock. The fault is characterized by prominent morphotectonic evidence, such as
426 triangular facets, deeply incised gullies, and down thrown paleosurfaces (See Fig. 4 for details). The
427 average strike of the Micciano section is N145.

428 The 4.8 km-long Fighille section runs at the base of the Anghiari ridge, from the southern part
429 of the Anghiari town to the Sovara River valley. A left step-over separates this section from the
430 Anghiari-Motina section. As first-order geomorphic evidence, the fault separates the Lower-Middle
431 Pleistocene CTA sediments of the Anghiari ridge from the Tiber River alluvial plain. At a closer
432 view, the fault trace is often concealed by anthropogenic modifications and its trace can be inferred

thanks to aligned escarpments on the CTA sediments and the alignment of the youngest generation of alluvial fans in the hanging wall. The average strike of the Fighille fault section is N130.

The 5 km-long Valcelle fault section is located within a NW-SE-oriented valley that crosses the Anghiari ridge, from the Anghiari town to the southern side of the Sovara River valley. It is confined within the CTA synthem, without prominent geomorphic expression, except for the southern part, where the fault crosses the Sovara River and forms a straight scarp within the CTA synthem, on the southern side of the valley (Fig. 1). The average strike of the Valcelle fault section is N130. This fault section is imaged as potentially active in Fig. 3 since it only affects Early-Middle Pleistocene deposits.

The geologic section A-A' in Fig. 3 crosses orthogonally both the Micciano and Anghiari-Motina fault sections, showing a throw component of 64-116 m of the MTC bottom, respectively

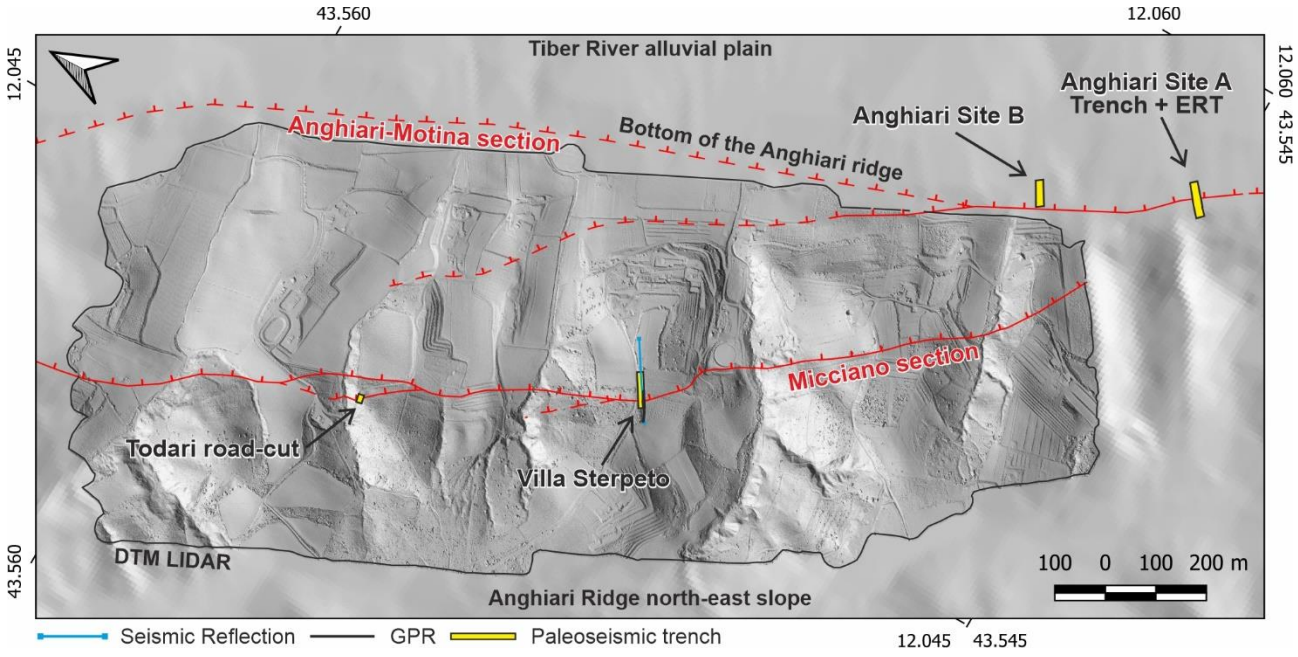

Fig. 4. Location map of the geophysical investigations and Paleoseismological trenches. The topographic maps are the 10 m/pixel DTM TINITALY (Tarquini et al., 2012) and the newly acquired, 0.2 m/pixel DTM LIDAR. The traces of the Anghiari-Motina and Micciano fault sections are shown in red.

448 ## 4.2. Villa Sterpeto site

449 The following paragraphs illustrate the results of both geophysical and paleoseismological
450 investigations conducted at Villa Sterpeto

451 ### *4.2.1. Geophysics*

452 The seismic reflection profile reveals two high amplitude, low frequency reflections, due to a
453 strong acoustic impedance contrast, gently dipping toward east and located between 15 and 35 m of
454 depth (Fig. 5a). Given the general WSW dip of the bedding in the area, we consider the dip of these
455 reflections as apparent due to the seismic line strike and lack of depth migration. At distance 60 m,
456 these two reflections are interrupted and displaced at depths of 15-20 m. This offset is interpreted as
457 due to a NE-dipping normal fault. The projection at the surface of the interpreted fault (red line in
458 Fig. 5a) intercepts the topography at distance between 45 and 60 m. However, the seismic line has a
459 low reflectivity within the first ~ 10 m depth interval, insufficient to provide more details and insights
460 on the stratigraphy and potential fault offsets. Another reflection discontinuity is visible between the
461 distances 104-116 m (Fig. 5a), although the poorly coherent reflections, and the lack of displacement,
462 do not constrain a reliable fault image.

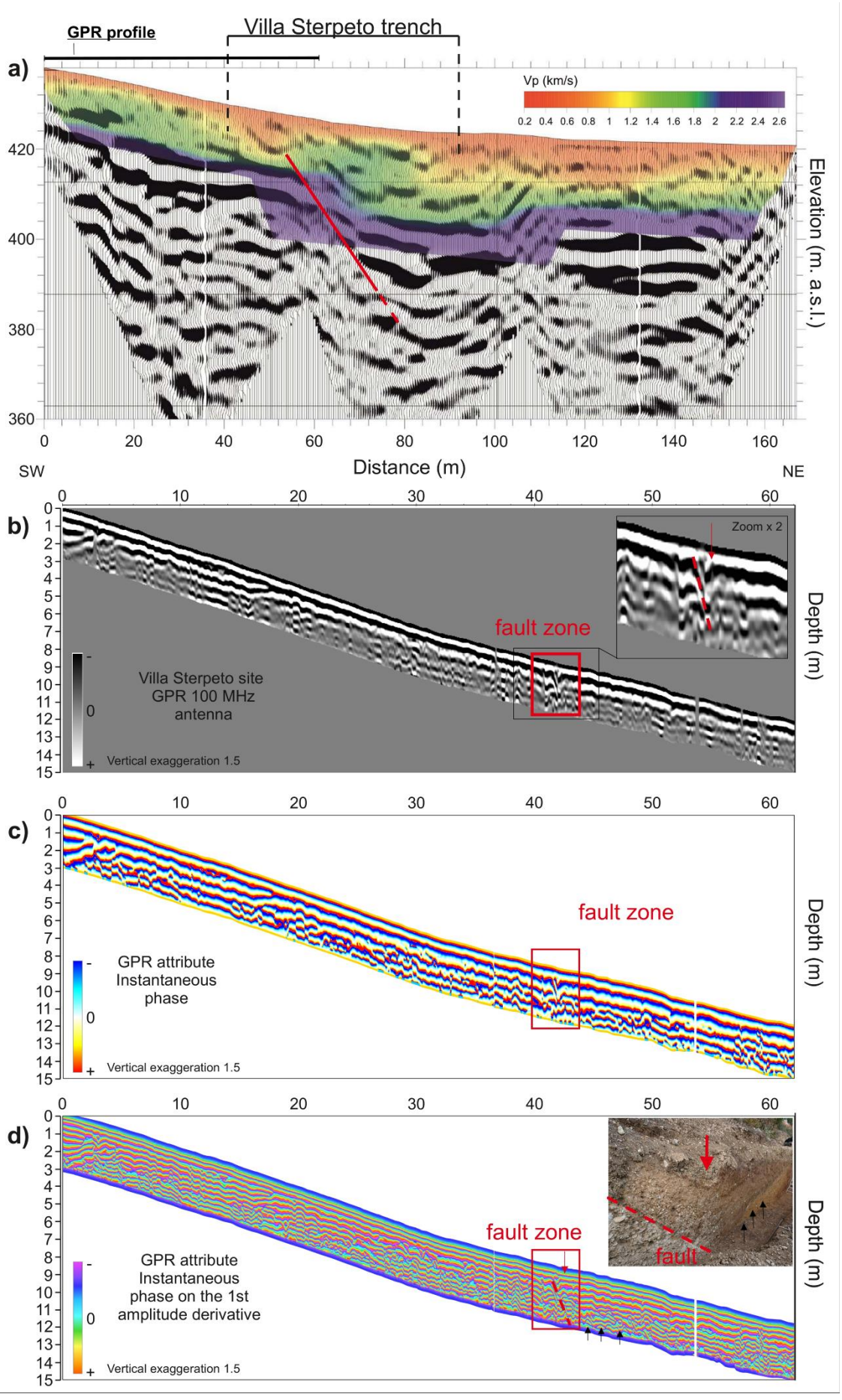
GPR profile
Villa Sterpeto trench
a)
Vp (km/s)
0.2 0.4 0.6 0.8 1 1.2 1.4 1.6 1.8 2 2.2 2.4 2.6
420
400
380
360
Elevation (m. a.s.l.)
0 20 40 60 80 100 120 140 160
SW
Distance (m)
NE
b)
Zoom x 2
fault zone
Villa Sterpeto site
GPR 100 MHz
antenna
Vertical exaggeration 1.5
Depth (m)
c)
fault zone
GPR attribute
Instantaneous
phase
Vertical exaggeration 1.5
Depth (m)
d)
fault zone
fault
GPR attribute
Instantaneous
phase on the 1st
amplitude derivative
Vertical exaggeration 1.5
Depth (m)

463

Figure 5: Geophysical data interpretation at the Villa Sterpeto site. a) Seismic reflection profile overlapped by refraction tomography model (details in supporting information, Text S1), and by the interpreted normal fault (red line); b) GPR profile; the red box points out the lateral radar discontinuity interpreted as a possible fault zone. c) instantaneous phase attribute enhancing the continuity of reflections as well as the fault zone; d) the GPR attributes enhances the geometries of the subsurface stratigraphy also in deeper sectors (3 m depth) characterized by low GPR reflection amplitudes caused by high-attenuation, as well as across the fault zone; the GPR attributes aid the interpretation due to higher level of details in comparison to b).

The GPR profile images the near surface portion of the transect, and it is characterized by continuous shallow reflections in the first two meters. At depth down to 3 m, the strong attenuation caused by the moderate to high conductivity of the deposits (ERT data available on the area show resistivity generally <50 Ωm in the shallow subsurface) does not allow to clearly interpret the stratigraphy. Analyzing more carefully the geometry of the shallower reflections, these show SW-dipping reflections at distances 0-5 m and 16-18 m, which could represent the conglomerates mapped in the footwall. A clear subvertical (E-dipping) discontinuity of GPR signal at ~ 42 m along the profile, could be compatible with a fault, being a GPR signature including reflection truncation, dip change and diffraction hyperbola (e.g., Ercoli et al., 2013, 2021b). This GPR signature appears as the surface projection of the fault zone seen on the seismic line (Fig. 5a). This GPR discontinuity was thus inferred as a possible fault zone, and it was later confirmed by ground trenching. Notice that the GPR attributes displayed in Figs. 5c and 5d offer a higher degree of detail in comparison to the conventional GPR profile of Fig. 5b. This consideration is confirmed not only by the enhancement of the phase discontinuity across the fault (red dashed line), but also by the emphasized gentle inflection of the shallower (hanging wall) deposits close to the fault, possibly including colluvial wedges (red arrow). In addition, the stratigraphic mapping of the deposits geometry is also strongly improved not only along the entire GPR profile, but also down to 3 m depth, where the attenuation, possibly due to conductive clayey layers, reduced the reflections amplitude in Fig. 5b. This fact is particularly visible

490 within the basal contact between the gently W-dipping reflections (black arrows in Fig. 5d) and the
491 overlying layers. The latter profile demonstrates the capability of GPR attributes to recover
492 information which are hardly visible in conventional GPR profiles, increasing the data interpretability
493 also in relatively unfavorable conditions caused by conductive materials.
494
495
496

Sample name	Long.	Lat.	Trench name	Depositional unit	Material (dated material)	Method - Lab.	Date of sampling (d/m/y)	Conventional radiocarbon age BP	Calendar calibrated results (%)
VS_C01	12.0459 E	43.5521 N	Villa Sterpeto	6	organic sediment (bulk organic fraction)	AMS - Beta Analytic	18/11/2021	20600 +/-70 BP	23126-22626 BCE (95.4%)
VS_C02	12.0459 E	43.5521 N	Villa Sterpeto	5	organic sediment (bulk organic fraction)	AMS - Plateforme Nationale LMC14	18/11/2021	13210 +/-60 BP	14106 - 13717 BCE (95.4%)
VS_C03	12.0459 E	43.5521 N	Villa Sterpeto	5	organic sediment (bulk organic fraction)	AMS - Plateforme Nationale LMC14	18/11/2021	14330 +/-70 BP	15863 - 15321 BCE (91.2%) 15286 - 15198 BC (4.3%)
VS_C06bis	12.0459 E	43.5521 N	Villa Sterpeto	3	organic sediment (bulk organic fraction)	AMS - Plateforme Nationale LMC14	18/11/2021	5650 +/-35 BP	4551 - 4436 BCE (78.5%) 4430 - 4363 BCE (16.9%)
VS_C07	12.0459 E	43.5521 N	Villa Sterpeto	Fz1	organic sediment (bulk organic fraction)	AMS - Plateforme Nationale LMC14	01/12/2021	1990 +/-30 BP	46 - 85 CE (88.2%) 95 - 117 CE (7.3%)
VS_C08	12.0459 E	43.5521 N	Villa Sterpeto	Fz1	organic sediment (bulk organic fraction)	AMS - Plateforme Nationale LMC14	01/12/2021	5330 +/-30 BP	4315 - 4300 BCE (3.1%) 4252 - 4151 BCE (45.4%) 4145 - 4050 BCE (47%)
VS_C12	12.0459 E	43.5521 N	Villa Sterpeto	5	organic sediment (bulk organic fraction)	AMS - Beta Analytic	01/12/2021	11910+/-40 BP	11864 - 11656 BCE (82%) 12054 -11991 BCE (10.7%) 11908 - 11882 BCE (2.7%)
VS_C13	12.0459 E	43.5521 N	Villa Sterpeto	5	organic sediment (bulk organic fraction)	AMS - Beta Analytic	01/12/2021	12940 +/-40 BP	13677 - 13351 BCE (95.4%)
Tod_C01	12.0421 E	43. 5564 N	Todari Roadcut	6	organic sediment (bulk organic fraction)	AMS - Beta Analytic	19/11/2021	6270 +/-30 BP	5318 - 5207 BCE (91%) 5162 - 5125 BCE (4%) 5089 - 5084 BCE (0.4%)
Tod_C02	12.0421 E	43. 5564 N	Todari Roadcut	5	organic sediment (bulk organic fraction)	AMS - Beta Analytic	19/11/2021	4710 +/-30 BP	3468 - 3373 BCE (54.8%) 3534 - 3489 BCE (24.1%) 3626 - 3576 BCE (14.9%) 3571 - 3561 BCE (1.6%)
Tod_C03	12.0421 E	43.5564 N	Todari Roadcut	5	organic sediment (bulk organic fraction)	AMS - Beta Analytic	19/11/2021	2730 +/-30 BP	928 - 810 BCE (95.4%)
Tod_C04	12.0421 E	43. 5564 N	Todari Roadcut	2	organic sediment (bulk organic fraction)	AMS - Beta Analytic	19/11/2021	300 +/-30 BP	1495 - 1602 CE (69.3%) 1610 - 1656 CE (26.1%)
Tod_C05	12.0421 E	43.5564 N	Todari Roadcut	FF	organic sediment (bulk organic fraction)	AMS - Beta Analytic	19/11/2021	470 +/-30 BP	1408 - 1460 CE (95.4%)
Tod_C06	12.0421 E	43.5564 N	Todari Roadcut	4	organic sediment (bulk organic fraction)	AMS - Beta Analytic	14/07/2022	1260 +/-30 BP	668 - 776 CE (73.9%)
TA_C3	125452 E	43.5420 N	Anghiari site A	4b	charcoal (charred material)	AMS - Beta Analytic	08/07/2022	4350 +/- 30 BP	3027 - 2899 BCE (92.8%) 3076 - 3064 BCE (2.6%)
TA_C6	12.0568 E	43.5452 N	Anghiari site A	3a	charcoal (charred material)	AMS - Beta Analytic	08/07/2022	1450 +/- 30 BP	571 - 651 CE (95.4%)
TA_C8	12.0568 E	43.5452 N	Anghiari site A	4b	charcoal (charred material)	AMS - Beta Analytic	08/07/2022	4500 +/- 30 BP	3351 - 3096 BCE (95.4%)

498 Tab. 1. Summary of radiocarbon dating analysis.

499 ### *4.2.2. Stratigraphy and primary tectonic features*

500 The Villa Sterpeto paleoseismological trench was dug to disclose the fault zone imaged by
501 the geophysical investigations (Fig. 6). The trench walls exposed 11 depositional units. The oldest
502 continental unit, formed by gravels of the Citerna synthem (unit 11), is juxtaposed by faulting to the
503 younger sedimentary sequence of the Anghiari sub-synthem (units 7, 8, 9 and 10), colluvium
504 containing paleosols (unit 2, 3, 4, 5 and 6) and anthropogenic deposits (unit 1). The detailed
505 description of the stratigraphy is reported in the supporting information Text S3.

Fig. 6. Interpreted orthophotomosaic of the north-west wall of the Villa Sterpeto trench. The white squares correspond to the location of the pictures in fig. 8. The stereoplot, from left to right, represents respectively: results of AMS analysis (square, triangle and circle are maximum, intermediate, and minimum susceptibility axes, respectively); bedding attitude; and fractures attitude. The rose diagram shows the fracture attitude measured on the trench wall (in orange) and bench (in black).

The fault affects the entire trench wall up to the base of the topmost unit (unit 1), with a sharp contact, 10-20 cm-wide thickening in the upper part, dipping 50° toward NE (Fig. 7). In particular, the fault mean attitude is 052/52 (dip direction/dip) with variable value of dip ranging from 48 to 60 degree; the slip vector measured on striae trends 85°N and the plunge is 57°. Based on its lithological and chromatic features, the fault zone is divided into a stiff light brown fine-grained, organic rich fault zone (FZ1) and a whitish fault zone made of crushed gravel, outcropping in the lower part of the trench (FZ2). Locally, FZ1 and FZ2 are separated by a shear surface. Two samples of FZ1 bulk sediments were collected for radiocarbon dating (VS_C07 and VS_C08), providing ages of 46 - 117 CE and 4,315 - 4,050 BCE, respectively (Tab. 1).

In the hanging wall of the fault, the colluvial unit 4 forms four coarse-grained wedge-shaped bodies of material colluviated from unit 11 that interfinger with unit 5 (CW1-4 in Fig. 7). An additional wedge-shaped fifth body (CW5?) is partially visible in the lowest part of the trench wall. The four wedge-shaped bodies are stacked with similar shape and size. Their geometric settings, suggests an accumulation controlled by episodes of footwall exhumation. A mechanism able to explain all those features is the rapid formation of a scarp due to surface faulting events, and consequent accumulation of scarp-derived colluvial wedges in proximity of the fault due to scarp degradation (colluvial wedge model in McCalpin, 2009).

Based on the gravel fabric, it is possible to estimate a maximum wedge thickness of 45 cm with large uncertainty. The thickness of the wedge CW5 is uncertain since it is partially buried.

CW4 and CW3 have comparable lateral extension and their tip is lying on darker and fine-grained horizons. Particularly, CW3 overlays a 5 to 10 cm-thick weak paleosol, which possibly corresponds to the topographic surface immediately before the onset of coarse-grained colluvial sedimentation (Fig. 7c). Between CW3 and CW4 an open fissure branches from the main fault zone and is infilled with the same material of the wedge.

CW2 is steeper and thicker near the fault, with a few cm-thick fine-grained layer, possibly corresponding to a weak soil horizon, at the base of its tip. CW 1 is the smallest wedge and does not show a clear fine-grained horizon at its base. All the wedges are faulted.

In order to constrain the age of each wedge formation, and thus of related episodes of footwall exhumation, we collected samples for radiocarbon dating of the fine-grained organic layers of unit 5, at their bases, paying attention to collecting the most organic layers. Due to the lack of charcoals in units, the dating was performed on the bulk organic fraction contained in the sediments. Moreover, we sampled the units 6 and 3 which are the lowermost and uppermost boundaries of the entire colluvial unit, respectively.

The hanging wall depositional sequence from unit 6 to 10 is tilted against the fault. The mean layer attitude in the trench is 265/12 (dip direction/dip). The dip of the boundary between units 6 and 7 becomes progressively steeper toward the fault, from 5° to 25°, suggesting syn-depositional back-tilting. In the nearby of the trench, in the hanging wall of the fault, the Citerna synthem is tilted up to 35° towards the west. This geometrical setting can be interpreted as large-scale, fault-related hanging wall back-tilting that created accommodation space for the deposition of units 1 to 5.

To measure the displacement of the fault we used the buried paleosol of unit 6, the top of which should correspond to an ancient topographic surface. The top of unit 6 is displaced about 4 m vertically (5.1 m along-dip slip) with respect to the nowadays topographic surface. Since the topographic surface may have been reshaped, this should correspond to the minimum fault displacement accumulated since the age of unit 6 (23,126 - 22,626 BCE, sample VS_C01) (Tab. 1).

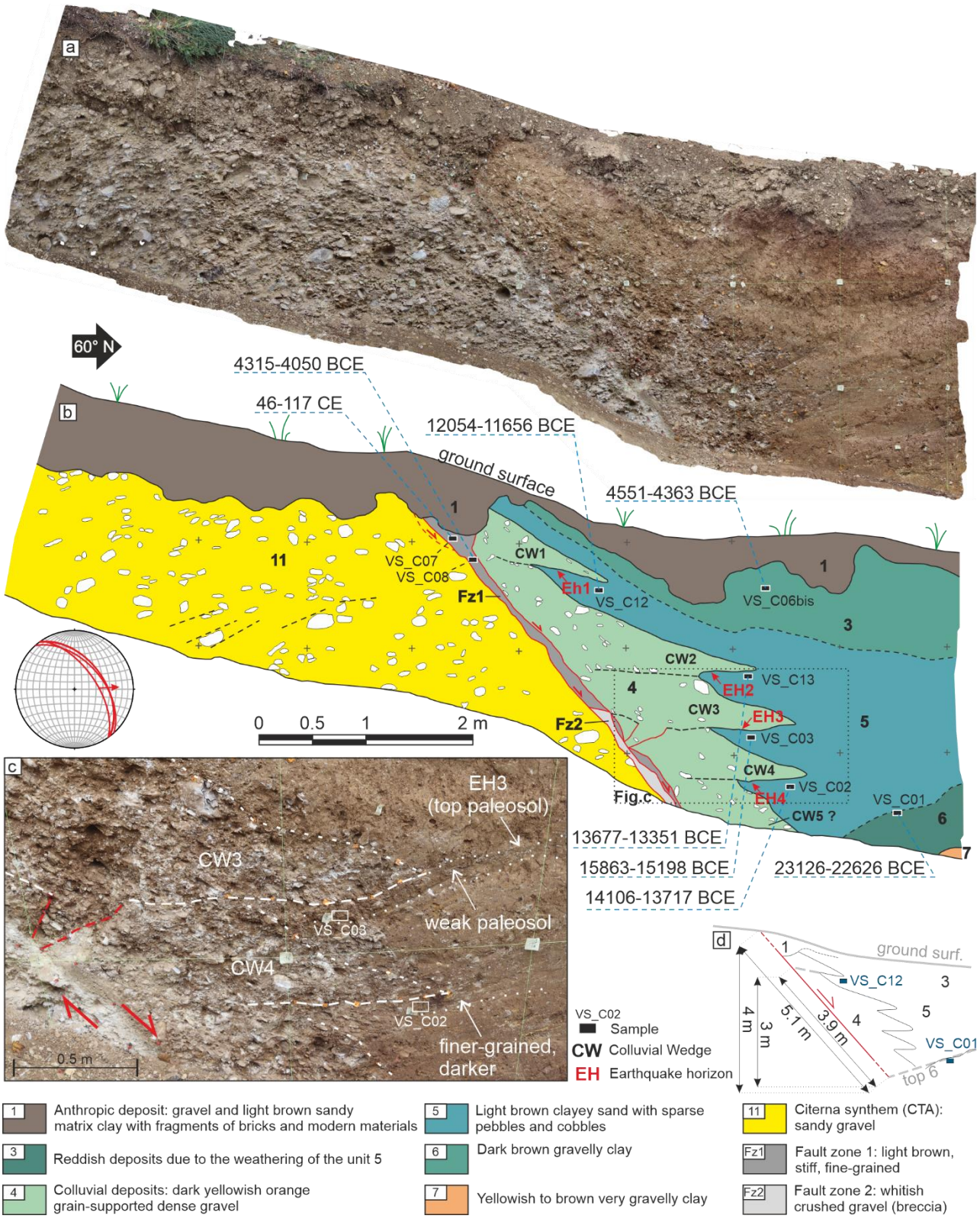

Fig. 7. Detailed view of the fault zone of the Villa Sterpeto trench (a); interpretation of the fault zone of the Villa Sterpeto trench, with the age of the samples (b); detail of the colluvial wedges CW3 and CW4 and the corresponding

563 earthquake horizons (c); simplified scheme of displacement measure to compute the slip rate (d); The attitude of the fault
564 and the corresponding slip vector are shown in the stereo plot.

565 ### *4.2.3. Fissures and other secondary features*

566 Many fractures, fissures and other soft-sediment deformation affect units 9 and 8 (Fig. 6). A sharp
567 boundary separates unit 9 from the underlying massive gray clays of unit 10 (Fig. 8a). In general, the
568 fissures have an aperture in the order of 0.5 to 2 cm and are infilled with clay material from unit 10.
569 Other fractures, without measurable aperture, are highlighted by a cm-sized bleaching halo,
570 particularly evident in the red-colored unit 8. Unit 9 is pervaded by both layer-parallel and layer-
571 perpendicular (or oblique) fissures (Fig. 8b). Most of them are confined within unit 9, while some of
572 them cut through both units 9 and 8 perpendicularly to the bedding (Fig. 8c). Layer-perpendicular
573 fractures with bleaching halo prevail in unit 8. When observed on the SE-facing wall of the trench,
574 the layer-perpendicular fissures, and fractures dip apparently to the NE, as they are tilted with the
575 hosting sedimentary beds (Fig. 6). Nevertheless, the true dip is nearly vertical; the measured strikes
576 cluster around values of 70±10° (stereonet in Fig. 6). In map view (on the bench floor, Fig. 8d), some
577 fractures form approximately conjugate systems, with acute angles of 45-60°. Overall, the strikes
578 measured on the trench wall and on the bench floor are dispersed between 30° and 120°, with a main
579 cluster at 70±10° (the bisector of the acute angle) and two secondary clusters at 105±5° and 50±15°
580 (rose diagrams in Fig. 6).

581 The boundary between units 8 and 9 is affected by soft-sediment deformation of different
582 types. At places, flames of clay injections fed by fissures from unit 9 intrude into the bottom part of
583 unit 8, forming “jester hat-like features” (Fig. 8b). Often, the stratigraphic transition is characterized
584 by a 10-15 cm-thick breccia layer formed by angular clasts from unit 8 in the matrix of unit 9, which
585 indicates mixing along the boundary between the two units. The breccia layer can intrude slightly
586 into the overlying unit 8, forming flame structures (Fig. 8e), or can be coated by clay material, forming

pseudo-nodules (Fig. 8f). The interpretation of these features as due to earthquake-induced ground shaking would give insights on the recurrence of strong earthquakes on the Sansepolcro basin fault system, as argued in the discussion section.

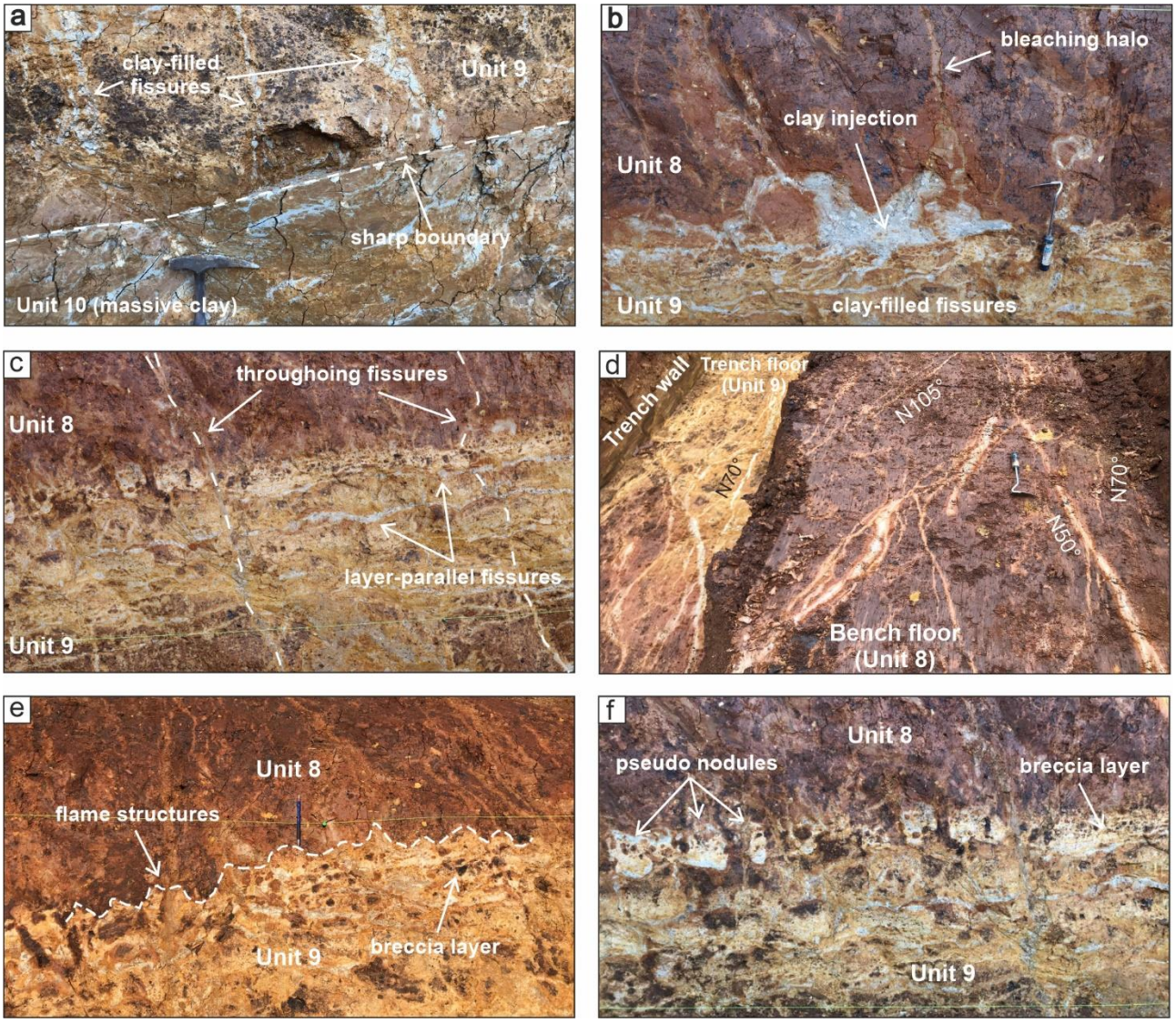

Fig. 8. Detailed views of soft-sediment deformation within units 8 and 9. Clay injections and clay-filled fissures are sourced by unit 10. Location in Fig. 6. Fig. (d) is an oblique view to NNE of the trench and bench floors.

4.2.4. Anisotropy of magnetic susceptibility

The results of the AMS analyses are reported in the supporting information (Figure S5 and Table S1). The mean susceptibility on the sites collected in the clays varies from 139 to 217 e-6 SI, while the sites collected in the paleosol and in the colluvial unit containing the wedges have higher susceptibility, from 888 to 7162 e-6 SI. All sites are characterized by a well-defined AMS tensor. The shape of the ellipsoids, T, varies from weakly oblate (ANGH01, 02, 04, 05) to strongly prolate (ANGH03) and one site is triaxial (ANGH08). The degree of anisotropy, P_j, indicates that the sites vary from weakly anisotropic (4% of ANGH01) to strongly anisotropic (43%, ANGH08), approaching the fault trace. The orientation of the k_{max} axis, that can represent the direction of the magnetic lineation (k_{max}/k_{int}), is mostly shallowly oriented NE-SW, and it is orthogonal to the foliation plane (k_{int} / k_{min}), oriented NW-SE, steeply dipping to the NE. The anisotropy data suggest that a primary sedimentary fabric has been overprinted by an incipient to intense tectonic fabric as confirmed by the evolving AMS tensor shape from purely oblate farther from the fault to oblate and prolate approaching the fault.

The magnetic foliation orientation is mostly NW-SE, thus sub-parallel to the fault plane. The magnetic lineation is orthogonal to the ATF and parallel to the NE–SW-oriented direction of extension revealed by both regional active stress field (Montone et al., 2016) and Quaternary strain indicators (Lavecchia et al., 2022). These results are comparable with the stretching direction inferred by Maffione et al. (2012) through the AMS analysis of the Lower Pleistocene Fighille synthem at a nearby site, south of the Anghiari ridge (their site SANS).

In summary, the AMS indicates continuous extension across the stratigraphy exposed in the trench. When compared with data from the literature, our results suggest that in the study area an extensional stress field has been continuously active since the Early Pleistocene.

620 ### 4.3. Todari site

621 The Todari roadcut was dug across a secondary strand of the Micciano section. The outcrop
622 exposes 7 units, a NE-dipping main normal fault zone and a sub-vertical antithetic splay (Fig. 9). The
623 main fault juxtaposes an Early-Middle Pleistocene unit, part of the Citerna synthem, from a Holocene
624 succession formed by, from the bottom to the top, a paleosol (unit 6), clayey palustrine deposits (unit
625 5), clayey-sandy colluvial units (unit 2 to 4) and the present-day soil (unit 1). An additional unit is
626 the infill of a fissure topped by unit 4 (FF, filled fissure).

627 The detailed description of the stratigraphy is reported in the supporting information Text S3.

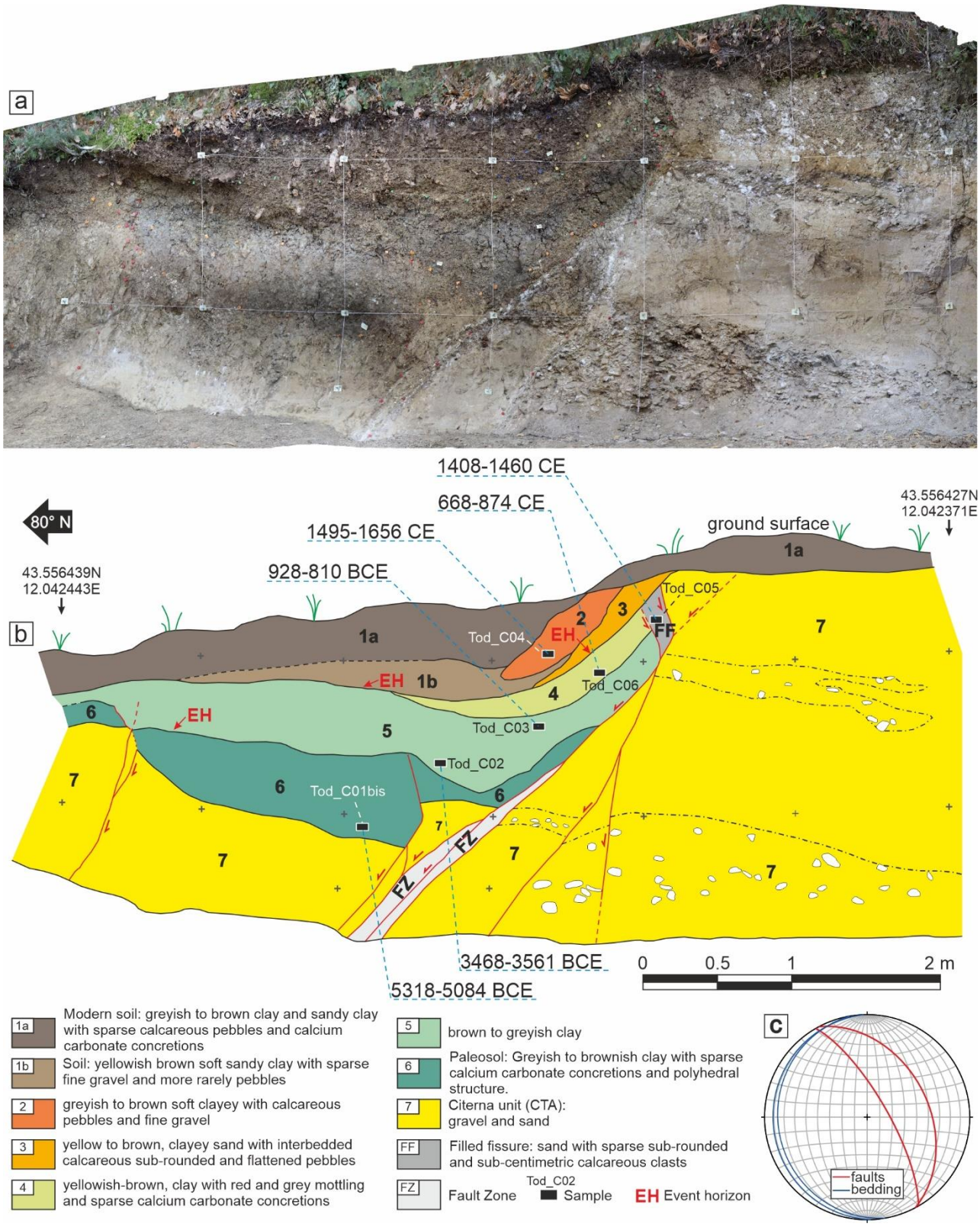

Fig. 9. Detailed view of the Todari roadcut (a); interpretation of the Todari roadcut, with the age of the samples (b); the attitude of the fault and bedding are shown in the stereo plot (c).

4.3.1. Primary tectonics features

The Todari roadcut is characterized by several synthetic normal fault splays dipping 40° to 50° towards NE. The main fault zone (FZ in Fig. 9) is composed of fault brecciated sand coming from the faulting of unit 7. The hanging wall of the main fault zone includes two synthetic splay dipping from 60° to 80° toward NE and connected to the principal fault in the upper part. Another synthetic splay displaces the boundary between units 6 and 7 in the hanging wall of the main fault. This fault dips 50° at the bottom of the trench and becomes progressively steeper upwards, up to overturn close to the surface. Unit 4, 5 and 6 are faulted and dragged against the main fault zone, whereas units 3 and 2 are deposited after the last apparent deformation episode.

A sub-vertical antithetic splay, located in the hanging wall at ~2 m from the main fault, displaces by 20 cm the boundary between units 6 and 7.

643 ## 4.4. Anghiari sites A and B

644 The site A trench was excavated across the trace of the Anghiari-Motina fault section, while
645 the site B trench was excavated in the hanging wall of the fault. The site B trench cut across the MTC
646 synthem and provided constraints on the stratigraphy of the hanging wall, which helped us in
647 constraining the displacement accumulated after the deposition of the MTC (Fig. 3). The
648 orthophotomosaic of the site B trench and its stratigraphic description are provided as supporting
649 information (Fig. S4). In the following, we describe the site A trench, which is characterized by 12
650 depositional units and 3 high-angle tectonic contacts (Fig. 10). The main tectonic contact downthrows
651 to the NE the stratigraphic succession older than unit 2. The youngest unit (unit 1) is an anthropogenic
652 backfill. Units 2 to 8 are colluvial deposits, the youngest of which (unit 2) is historical (contains
653 pottery shards). Unit 9 is a remnant of an alluvial terrace. Unit 10 is made of gravel and sand
654 belonging to the CTA synthem. The clayey unit 11 is the oldest unit, possibly belonging to the Fighille
655 synthem.
656 The detailed description of the stratigraphy is reported in the supporting information Text S3.
657

658 ### *4.4.1. Primary tectonics features (site A)*

659 The site A trench wall exposes three barely visible fault zones (FZ1, 2 and 3 in Fig.
660 10). Between FZ1 and FZ3 the depositional sequence and the faults are cut by a gravitational sliding
661 surface (green line in Fig. 10) with slip direction to the NE (i.e., downslope). The gravitational sliding
662 postdates the faults and is covered by unit 2 (containing reworked pottery shards of VII-XIV century
663 CE).
664 The main fault zone (FZ1, Fig. 10) is formed by two nearly parallel high-angle fault strands
665 downthrowing by a minimum of 1.75 m to the NE the contact between units 4b and 5. In the hanging
666 wall of the main fault there are two colluvial units (3a and 3b). Unit 3b is wedge-shaped and thickens

667 close to the fault, suggesting that its sedimentation can be related to the fault. It is not clear if unit 3b
668 is faulted or simply rests on the fault surface. The geometry of unit 3a is undetermined, as its western
669 edge is cut by the gravitational sliding surface and its upper part is truncated by unit 2. The possible
670 meaning of units 3a and 3b in relation to the fault activity will be discussed in the next section. The
671 fault zone is sealed by the gravitational sliding surface and by unit 2, which has an age not older than
672 VII-XIV centuries CE, or younger, on the basis of the findings of reworked pottery shards.
673 A sharp, high-angle lateral contact between unit 7 and unit 11 (FZ2, Fig. 10), located 3 m
674 upslope FZ1, can be interpreted as a tectonic contact sealed by the upper part of unit 7.
675 The third fault zone (FZ3, Fig. 10), formed by two antithetic strands downthrowing by ~10 cm to the
676 SW the base of unit 4b, is sealed by unit 2.
677 In order to constrain the fault prosecution at depth, we acquired an ERT along the trench floor. The
678 ERT profile reported in Fig. 10 was obtained by the joint inversion of the Wenner and dipole-dipole
679 acquisitions. The contact between the gravels of the Citerna synthem and the underlying clays and
680 silts is evident in the first meters of the profile. A sharp lateral resistivity variation, from <40 **Ω**m to
681 40-50 **Ω**m is present in the center of the profile and corresponds to the down-dip continuation of FZ2.
682 The down-dip continuation of FZ1 is not particularly evident but can be the cause of the eastward
683 lateral transition to lower resistivity values from 40-50 **Ω**m to <15 **Ω**m. There is no evidence in the
684 profile of FZ3, probably because the limited displacement does not produce a lateral resistivity
685 variation.
686

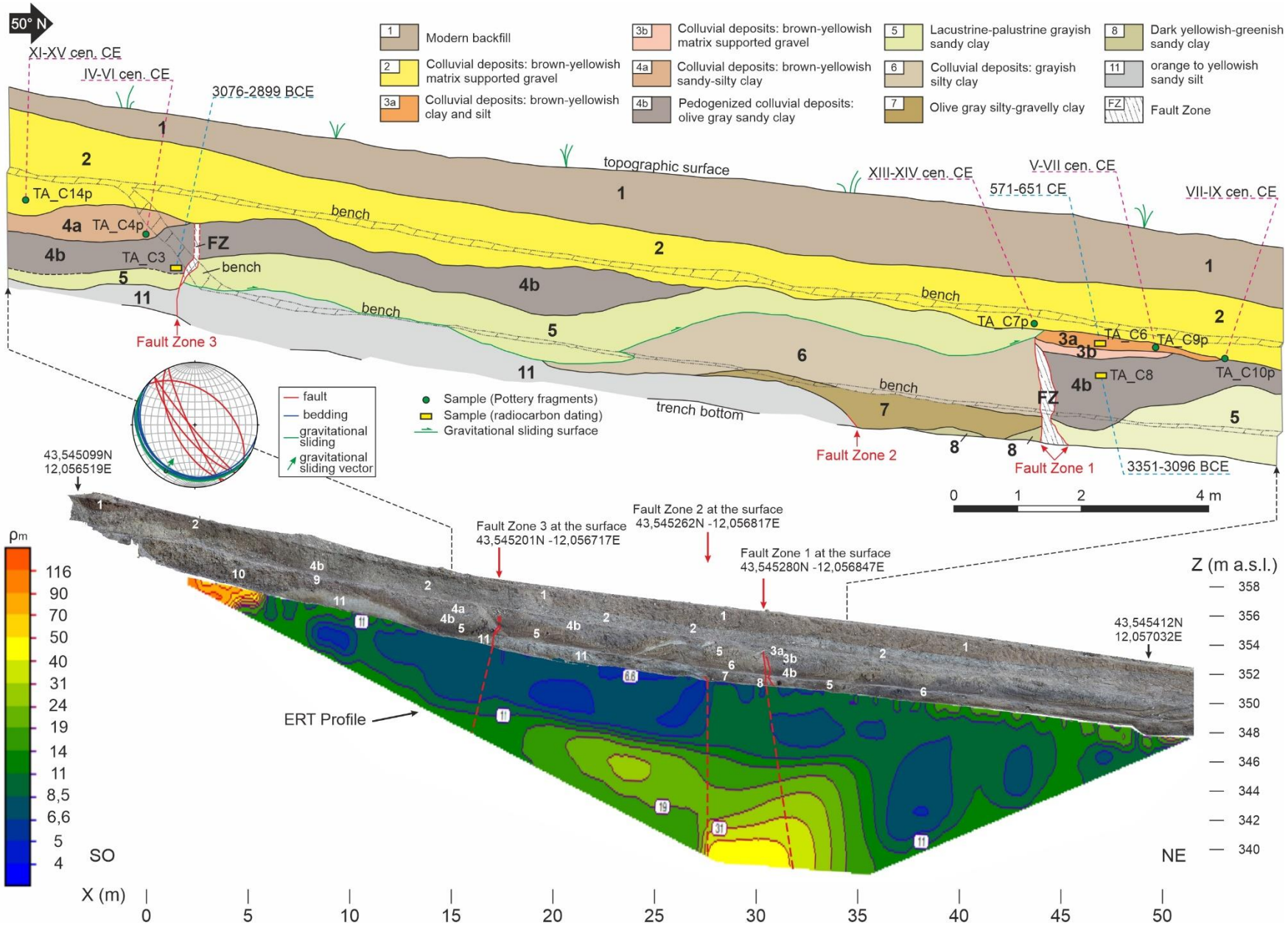
50° N
1 Modern backfill
2 Colluvial deposits: brown-yellowish matrix supported gravel
3a Colluvial deposits: brown-yellowish clay and silt
3b Colluvial deposits: brown-yellowish matrix supported gravel
4a Colluvial deposits: brown-yellowish sandy-silty clay
4b Pedogenized colluvial deposits: olive gray sandy clay
5 Lacustrine-palustrine grayish sandy clay
6 Colluvial deposits: grayish silty clay
7 Olive gray silty-gravelly clay
8 Dark yellowish-greenish sandy clay
11 orange to yellowish sandy silt
FZ Fault Zone
XI-XV cen. CE
IV-VI cen. CE
3076-2899 BCE
topographic surface
XIII-XIV cen. CE
V-VII cen. CE
571-651 CE
VII-IX cen. CE
TA_C14p
TA_C4p
TA_C3
TA_C7p
TA_C6
TA_C9p
TA_C8
TA_C10p
bench
trench bottom
Fault Zone 3
Fault Zone 2
Fault Zone 1
3351-3096 BCE
fault
bedding
gravitational sliding
gravitational sliding vector
Sample (Pottery fragments)
Sample (radiocarbon dating)
Gravitational sliding surface
0 1 2 4 m
43,545099N
12,056519E
Fault Zone 3 at the surface
43,545201N -12,056717E
Fault Zone 2 at the surface
43,545262N -12,056817E
Fault Zone 1 at the surface
43,545280N -12,056847E
43,545412N
12,057032E
ρm
116
90
70
50
40
31
24
19
14
11
8,5
6,6
5
4
ERT Profile
SO
NE
X (m)
0 5 10 15 20 25 30 35 40 45 50
Z (m a.s.l.)
358
356
354
352
350
348
346
344
342
340

Fig.10. Orthophotomosaic of the Anghiari site A trench and ERT profile acquired along the trench floor with interpreted down-dip continuation of the fault zones (bottom) and interpreted log of the stratigraphy and main fault zones with age of samples (top). The attitude of bedding, gravitational sliding surface, faults and slip vectors are shown in the stereoplot.

5. Discussion

5.1 Paleoearthquakes

At the Villa Sterpeto site the presence of five stacked colluvial wedges (CW in Fig. 7) against the fault suggests the occurrence of as many discrete and recurrent surface faulting earthquakes. Each earthquake is supposed to have produced a coseismic fault scarp at the surface (free face). The erosion of the exhumed scarp would have caused the deposition of colluvial material in the hanging wall of the free face, on top of the downthrown ground surface. This hypothesis is supported by the presence of fine-grained, moderately organic layers below the wedges, particularly developed beneath CW3 (i.e., the weak paleosol at the base of CW3, see Fig. 7c). Those fine-grained organic layers can be interpreted as the earthquake horizons (hereinafter EH), i.e., the topographic surface at the time of the surface faulting earthquakes. Moreover, the termination of the open fissure located below CW3, possibly corresponds to the boundary between CW3 and CW4, i.e., the earthquake horizon EH3 (see Fig. 7).

In addition, a fault activity during the colluvial accumulation is required to explain the formation of the space necessary for the stacking of the wedges in the hanging wall of the fault and their later faulting. Based on the above considerations, we interpreted the colluvial wedges as tectonic in origin .

Thanks to the radiocarbon dating, we tried to constraint the age of each EH and therefore hopefully the closest *pre faulting* age of each earthquake. The reconstructed chronology of the surface faulting earthquakes is reported in Fig. 11 and in Tab. 2.

CW1 was deposited immediately after 12,054 - 11,656 BCE (sample VS_C12, collected below the wedge), and before 4,551 - 4,363 BCE (sample VS_C06bis), collected within unit 3).

713 Therefore, the age window for E1VS is between 12,054 and 4,363 BCE. CW2 was deposited
714 immediately after 13,677 - 13,351 BCE (sample VS_C13, collected below the wedge), and before
715 12054-11656 BCE (sample VS_C12, collected above the wedge). Therefore, the age windows for
716 E2VS is between 13,677 and 11,656 BCE.
717 Because of the out of sequence ages of the samples VS_C03 and VS_C02 we advanced two different
718 hypotheses concerning the age of the events E3VS and E4VS:
719 1) Hypothesis 1 excludes sample VS_C03 due to significant age inheritance, beyond the
720 calibrated age uncertainty, caused by contamination from old material reworking. CW3 and CW4
721 would have deposited both between 14,106-13,1717 BCE and 13,677-13,351 BCE (samples VS_C02
722 and VS_C13). Therefore, E3VS and E4VS both occurred between 14,106 and 13,351 BCE.
723 2) Hypothesis 2 excludes sample VS_C02, thus assuming contamination by young carbon that
724 provides an age younger than the overlying sediments. CW3 would have deposited immediately after
725 15,863 - 15,198 (sample VS_C03) and before 13,677 - 13,351 BCE (sample VS_C13). CW4 would
726 have deposited after 23,126 - 22,626 BCE (sample VS_C01) and before 15,863 - 15,198 (sample
727 VS_C03) (Fig. 7). Therefore, E3VS occurred between 15,863 and 13,351 BCE, while E4VS occurred
728 between 23,126 and 15,863 BCE. Since the base of the wedge 5 and its chronological relationship
729 with respect unit 6 (sample VS_C01, 23,126 - 22,626 BCE) are buried below the trench floor, it is
730 not possible to exclude that, in the time interval relative to E4VS (23,126 - 15,863 BCE), more than
731 one earthquake has occurred.
732 Hypothesis 1 involves a cluster of earthquakes in a short time window, while hypothesis 2 provides
733 a more regular slip history. Hypothesis 1 appears more reasonable, because it implies the discard of
734 a sample (VS_C03) contaminated by old carbon, which has been demonstrated to be likely (Rockwell
735 et al., 2022). Nevertheless, sample VS_C03 was collected in one of the most evident buried paleosol
736 within the colluvial unit. This makes the sample more reliable than others. On the other hand, we
737 cannot exclude that younger carbon could have contaminated sample VS_C02. Since earthquake

738 clustering is quite common in the Apennines (as Chlorine 36 studies suggest, e.g., Benedetti et al.,
739 2013; Cowie et al., 2017; Mildon et al., 2022; Schlagenhauf et al., 2011), there are no particular
740 criteria to prefer one hypothesis to the other.
741 Since CW1 is faulted, there is evidence of at least an earthquake younger than E1_VS. Such event(s)
742 would be compatible with the tectonic folding of the unit 3 bottom (4,551 – 4,363 BCE, sample
743 VS_C06bis). According to the age of the organic material trapped and sheared within the fault zone
744 (sample VS_C08) this earthquake could be post 4,315 - 4,050 BCE.
745 At the Todari roadcut, the restoration of the tectono-stratigraphic setting allowed us to
746 reconstruct three surface faulting events (Fig. 12). The oldest event (earthquake E3 Tod) caused the
747 displacement of the boundary between units 6 and 7 along the synthetic and antithetic splays in the
748 hanging wall of the main fault (Fig. 12b). This earthquake occurred after 5,318 - 5,084 BCE, age of
749 unit 6 (sample Tod_C01bis) and before 3,468 - 3,561 BCE, age of unit 5 (sample Tod_C02). The net
750 slip measured on the synthetic splay was 18 cm, with a minimum net throw of 14 cm. This can be
751 considered as the minimum surface displacement of the earthquake because some slip could have
752 occurred along the main fault, which shows no visible piercing points (Fig. 12b). After E3 Tod, an
753 erosional event, possibly caused by water running parallel to the fault, reshaped the top of unit 6,
754 erasing the evidence of slip along the synthetic fault (Fig. 10c). The age of E3 Tod could be
755 comparable to the age of the earthquake faulting CW1 at the Villa Sterpeto trench.
756 Earthquake E2 Tod occurred after 928-810 BCE, age of unit 5 (sample Tod_C03) and before 668-
757 874 CE, age of unit 4 (sample Tod_C06) (Fig. 12e). This event caused a minimum net slip along the
758 main fault of 52 cm (minimum throw of 35 cm), including the dragging of units 5 and 6 and rotation
759 of the high angle splay in the upper part of the main fault (Fig. 12e). The subsequent erosion of the
760 fault scarp caused the deposition of a colluvial wedge (unit 4) (Fig. 12f). The most recent earthquake
761 (MRE Tod) caused the opening of a fissure in correspondence of the rotated synthetic splay and the
762 dragging of units 4, 5 and 6 (Fig. 12g). The minimum net displacement along the main fault was 35

cm (minimum throw of 23 cm). After the MRE, because of the erosion of the scarp, the fissure was filled and another colluvial wedge was formed (unit 3) (Fig. 12h). The MRE occurred after 668-874 CE, age of unit 4 (sample Tod_C06) and immediately before 1408-1460 CE, age of the infilling of the fissure (sample Tod_C05). The fissure infill is rich in organic matter. It is likely that the fissure was infilled by material from the soil at the time of the surface faulting. Therefore, the age of the infill should be close to the occurrence of the event. The minimum cumulative net slip of the last three earthquakes is 1.05 m (minimum cumulative throw of 0.72 m) accumulated since 5,318 - 5,084 BCE. The age constraints bracketing the event windows for the Villa Sterpeto and Todari sites are summarized in Fig. 11a and Tab. 2. Using the Boundary-Zero Boundary model, we performed a Bayesian analysis in OxCal v4.4.4 at the Villa Sterpeto site skewing the age of the earthquakes thanks to the samples collected immediately below the colluvial wedges, i.e., within the earthquake horizons. At the Todari roadcut we used the same methodology to constrain the age of MRE_Tod close to the age of the infilling of the fissure (sample Tod_C05); the age of E2_Tod close to the deposition of the colluvial wedge corresponding to unit 4 (sample Tod_C06); and the age of E3_Tod close to the age of the base of unit 5. The obtained ages are reported in Fig. 11b.

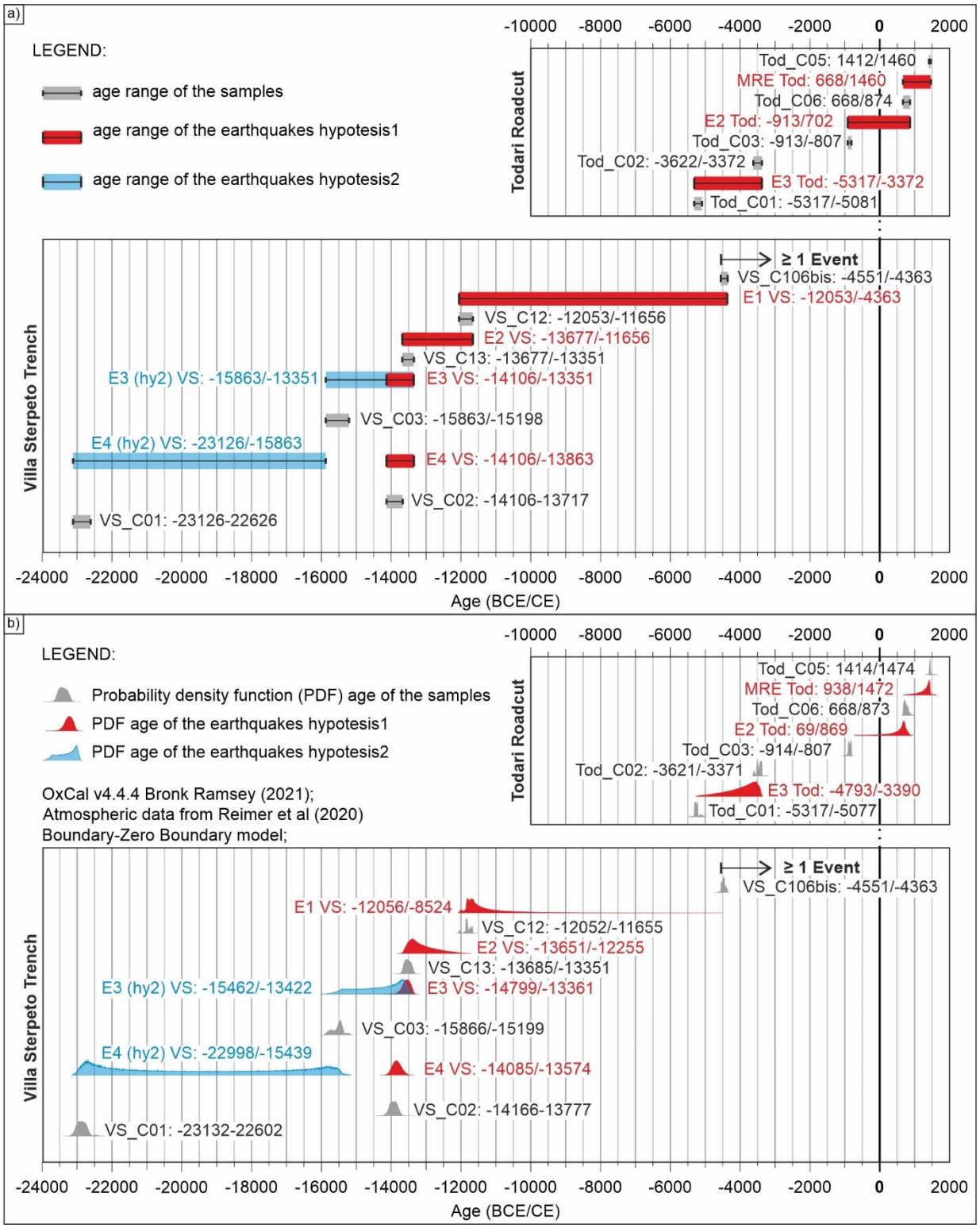

780

781 Fig. 11. a) Summary of the seismic history of the Anghiari fault showing the age windows of each earthquake
782 corresponding to the time window between the age of a couple of samples. Referring to E4_VS and E3_VS the hypothesis
783 2 is represented in blue. b) Summary of the seismic history of the Anghiari fault showing the probability density function

related to the age of each sample and each earthquake, computed using the Boundary-Zero Boundary approach in OxCal. Referring to E4_VS and E3_VS the hypothesis 2 is represented in blue.

Trench	Fault	Coord. of the fault at surface		fault attitude (imm./incl.)	Event n.	Evidence	Maximum age		Sample	Minimum age		Sample	Preferred age (OxCal Byesian model)	Maximum vertical thickness(hC W, m)	Displacement (D, m)	Type D
		Long.	Lat.				Max	Min		Max	Min					
Todari Roadcut	Micciano Sec	12.0423	43.5563	058/40	MRE Tod	FF - D	874 CE	668 CE	Tod_C06	1460 CE	1408 CE	Tod_C05	938 - 1472 CE	0.25	0.35	FF; D
Todari Roadcut	Micciano	12.0423	43.5563	058/40	E2 Tod	D	928 BCE	810 BCE	Tod_C03	874 CE	668 CE	Tod_C06	69 CE - 869 BCE	0.3	0.52	D
Todari Roadcut	Micciano	12.0423	43.5563	058/40	E3 Tod	S	5318 BCE	5084 BCE	Tod_C01bis	3561 BCE	3468 BCE	Tod_C02	4793 BCE - 3390 BCE	/	0.18	V
Villa Sterpeto	Micciano	12.0457	43.552	052/51	E1 VS	CW	1205 4 BCE	1165 6 BCE	VS_C 12	4551 BCE	4363 BCE	VS_C 06 bis	12056 BCE - 8524 BCE	0.45	/	C W
Villa Sterpeto	Micciano	12.0457	43.552	052/51	E2 VS	CW	1367 7 BCE	1335 1 BCE	VS_C 13	1205 4 BCE	1165 5 BCE	VS_C 12	13651 BCE - 12255 BCE	/	/	C W
Hypothesis1 (No sample C03)																
Villa Sterpeto	Micciano	12.0457	43.552	052/51	E3 VS	CW	1410 6 BCE	1371 7 BCE	VS_C 02	1367 7 BCE	1335 1 BCE	VS_C 13	14799 BCE - 13361 BCE	0.45	/	C W
Villa Sterpeto	Micciano	12.0457	43.552	052/51	E4 VS	CW	1410 6 BCE	1371 7 BCE	VS_C 02	1367 7 BCE	1335 1 BCE	VS_C 13	14085 BCE - 13574 BCE	0.45	/	C W
Hypothesis2 (No sample C02)																
Villa Sterpeto	Micciano	12.0457	43.552	052/51	E3 VS	CW	1586 3 BCE	1519 8 BCE	VS_C 03	1367 7 BCE	1335 1 BCE	VS_C 13	15462 BCE - 13422 BCE	0.45	/	C W
Villa Sterpeto	Micciano	12.0457	43.552	052/51	E4 VS	CW	2312 6 BCE	2250 3 BCE	VS_C 01	1586 3 BCE	1519 8 BCE	VS_C 03	22998 BCE - 15439 BCE	0.45	/	C W

Tab. 2. Summary of the paleoearthquakes ages and features. MRE = Most Recent Earthquakes; V = Vertical displacement; S = Dislocation of stratigraphic horizon; CW = Colluvial Wedge; D = Dragging; FF = Filled Fissure

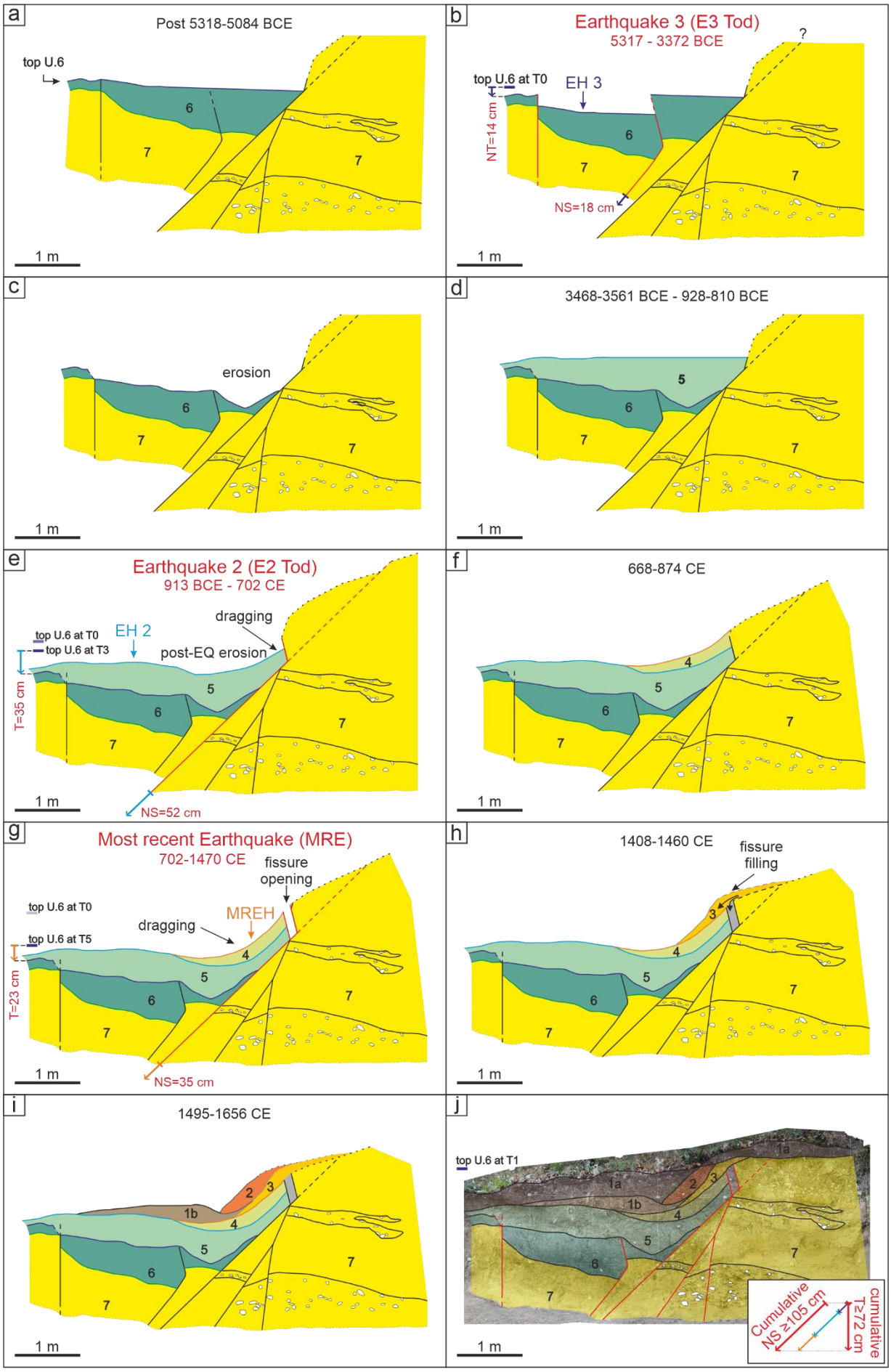

EH = earthquake horizon (ground surface at the time of earthquake surface faulting);T = throw NT = net throw; NS = net slip

Fig.12. Restoration of the Todari roadcut starting from the pre E3_Tod to the nowadays configuration. a) Pre E3_Tod and post 5318-5084 BCE configuration; b) E3_Tod (between 5317 and 3372 BCE), the top of unit 6 is displaced by synthetic and antithetic splays of the main fault; c) after E3_Tod the top of unit 6 is reshaped by erosional events; d) between 3468-3561 BCE and 928-810 BCE unit 5 is deposited; e) E2_Tod (between 913 BCE and 702 CE) unit 5 and 6 are displaced by the main fault and its antithetic splay and dragged by the main fault. The top of unit 5 is reshaped by erosional events; f) after E2_Tod (between 668 and 874 CE) the colluvial wedge corresponding to unit 4 is deposited; g) MRE_Tod (between 702 and 1470 CE) caused the dragging of unit 4, 5 and 6 and the opening of a fissure; h) After MRE_Tod and close to the 1408-1460 CE the fissure is infilled and the colluvial wedge corresponding to unit 3 is deposited; i) Around 1490-1656 CE unit 2 is deposited; j) nowadays configuration.

At the Anghiari site A the colluvial wedge 3a, possibly faulted, suggests the occurrence of one or two surface faulting earthquakes occurred between 3,351 - 3,096 BCE and XIV century (or shortly after, considering that the pottery shards are reworked), the ages of unit 4b and 2, which are comparable with the time windows of the youngest events of the Todari roadcut site.

The youngest recognized earthquake occurred in historical time (938 - 1472 CE, Fig. 11b). Two historical earthquakes hit the Sansepolcro basin in that time interval or close to it, the 1458 and 1489 earthquakes (Fig. 2), with the 1458 being the strongest (epicentral intensity VIII-IX, Mw 5.8). Therefore, the youngest surface faulting event might correspond to one of these two earthquakes, possibly the 1458 event, which fit the time window of the surface faulting event. Unfortunately, the 1458 event is poorly constrained by macroseismic data. The Anghiari town, the nearest town to the studied fault, has no macroseismic information on both the 1458 and 1489 events. The 1458 earthquake produced damages of intensity VIII-IX in both Città di Castello, in the southern edge of the basin, and in Sansepolcro, 15 km north of Città di Castello and only 7.5 km east of Anghiari. Damage of intensity VII-VIII was documented for a locality sited 13 km south of Città di Castello. In this context, it seems unlikely that the earthquake did not damage Anghiari, at a distance of 17 km to Città di Castello and 7.5 km to Sansepolcro, within the same sedimentary basin. The lack of macroseismic information in Anghiari is possibly due to a gap in the historical documentation.

Therefore, we suggest that the 1458 earthquake was caused by reactivation of the Anghiari fault, and possibly of the entire Anghiari-Città di Castello main fault.

In summary, combining the data from all the paleoseismological investigations, we recognized nine different earthquakes in the last 22 ka and an additional one possibly older than 25 ka. The most recent event possibly corresponds to the 1458 historical earthquake. These events broke the surface along the Micciano section of the Anghiari fault (Villa Sterpeto site), the secondary splay located in its footwall (Todari roadcut) and, at least the two most recent earthquakes also could have broken the Anghiari-Motina section (Anghiari site A). These sites might show two different parts of the same seismic history: i) the oldest part (22,000 to 4,500 BCE) at the Villa Sterpeto site; ii) the youngest part (5,200 BCE to 1,437 CE) at the Todari roadcut and Anghiari site A sites.

5.2 Recurrence intervals and coefficient of variation

The mean recurrence time interval has been estimated from our paleoseimological earthquake time series and its uncertainties in dating, with a Monte Carlo simulation approach through the tool RP included in the FISH tools package for seismic hazard assessment (Pace et al., 2016, code available at http://fault2sha.net/wp-content/uploads/2020/07/FiSHvers1.02.zip). Given the time windows of a series of paleo-events the RP tool produces a number of earthquake catalog simulations and computes the average recurrence time and its coefficient of variation (CV), namely the standard deviation of the recurrence times over their mean. CV is a critical parameter for time-dependent seismic hazard estimates, it is often poorly constrained (e.g. Ellsworth et al., 1999; Visini and Pace, 2014), and small differences in the values can lead to large differences in earthquake probability evaluation.

In tab. 3 are reported the computed values of mean recurrence time intervals based on the constrained age of the paleoearthquakes for both the earthquake ages hypotheses and considering both the time windows between each couple of samples (see Fig. 11a) and the earthquakes age obtained using

OxCal v4.4.4 (see Fig. 11b).

Considering that, in hypothesis 2 (quasi-periodic slip history), within the time windows related to the event E4_VS more than one earthquake may have occurred, this event has been excluded from the computation. While, for hypothesis 1 (clustering) all the events have been considered.

Using only the age of the samples as constraints for the age of the earthquakes, the mean recurrence time interval ranges between 2495 years and 3104 years, with a CV of 0.94-0.65 (for hypothesis 1 and hypothesis 2 respectively).

Using the earthquake time windows from the Bayesian model computed in OxCal, the mean recurrence time interval ranges between 2562 years and 3230 years with a CV of 0.92-0.62 (for hypothesis 1 and hypothesis 2 respectively).

Both the Recurrence time interval and the CV are affected by the choice of the hypothesis, while they are not affected by the ages used as input in the computations (age of the samples rather than OxCal). In general: i) for hypothesis 1 the recurrence time interval is shorter, but the CV is higher, indicating a non-periodic behavior. Ii) for hypothesis 2 the recurrence time interval is higher, but the CV is lower, indicating a more periodic behavior.

Paleoearthquakes age constraints	Paleoearthquekes age hypothesis	Recurrence interval (years)	Coefficient of variation
Age of the samples	1	2495	0.94
Age of the samples	2	3104	0.65
OxCal	1	2562	0.92
OxCal	2	3230	0.62

Tab .3. Recurrence time interval and coefficient of variation computed using the RP tool of the FISH tools package (Pace et al., 2016) for both the earthquakes ages hypothesis and using only the age of the samples or the ages obtained using OxCal.

907 **5.3 Slip rates**

908 The minimum fault displacement measured at the Villa Sterpeto site (5.1 m accumulated since
909 the age of unit 6, i.e., after 23,126 - 22,626 BCE) provides an average post-25 ka BP slip rate of 0.2
910 mm/yr. This slip rate is apparent, as it includes both closed and open seismic cycles. In order to
911 consider only closed seismic cycles, the displacement of the top of unit 6 can be measured compared
912 to the topographic surface immediately before the sedimentation of wedge CW1. In this case the
913 displacement is about 3.9 m in a time window between 23,126 - 22,626 BCE and 12,054 - 11,656
914 BCE (Fig. 7b). This corresponds to a slip rate of 0.29 - 0.31 mm/yr.

915 At the Todari roadcut site the total amount of displacement of 1.05 m accumulated after 5,318
916 - 5,084 BCE (formation of unit 6), provides an average post-5 ka slip rate of 0.14-0.15 mm/yr for this
917 secondary strand.

918 At the Anghiari trench site A, the presence of the gravitational sliding surface makes it
919 difficult to measure a reliable displacement. A minimum of 1.75 m of displacement accumulated from
920 3,351 -3,096 BCE, estimated by means of the base of the unit 4b (sample TA_C8, assuming a small
921 amount of motion of the sliding. With this assumption, the calculated slip rate is 0.35 mm/yr.

922

923 **5.4 Interpretation of secondary features**

924 In the following we discuss a number of points that collectively support an earthquake-
925 induced origin of the observed secondary features (Fig. 8) under the current extensional stress regime.

926 Hydrofracturing due to pressurized fluids seems to be the most plausible mechanism for
927 explaining the pervasive occurrence of fractures and fissures. High fluid pressure would have caused
928 the opening of fractures, and fluid circulation probably led to the formation of bleaching halos.
929 Fissures infilled by gray clay from unit 10 indicate that this clay was fluidized, probably due to a
930 combination of poor lithification and high content of water at elevated pressure. The upward direction
931 of fluid escape is indicated by the symmetry of flame and injection structures observed at the top of

unit 9 (Fig. 8). Moreover, the number of fractures and clay-filled fissures reduce drastically passing from unit 9 to unit 8. This suggests that the clayey paleosol of unit 8 behaved as a cap to upward-directed fluid flow. Different types of soft-sediment deformation in clayey material, generally associated with high hydraulic pressure, were documented in different geologic contexts (e.g., Van Loon, 2009 and references therein), including clay-rich clastic dykes and sills injected due to seismic-induced hydrofracturing and fluidization (e.g., Levi et al., 2006; Montenat et al., 2007).

The breccia layer at the top of unit 9 suggests mixing of material from units 9 and 8. Soft-sediment folding of different intensity, in places further deformed into mixed breccia layers, were documented in the Dead See graben (Marco et al., 1996), and are explained with mechanisms of Kelvin–Helmholtz instability due to layer-parallel shear during earthquake shaking (Heifetz et al., 2005). If the shear is unidirectional, such as for gravitational sliding along a sloping surface, folds are asymmetric. In the Villa Sterpeto trench, there are only symmetric flame structures and breccia, suggesting relative shear between the two layers sufficiently intense to produce brecciation and mixing, but not unidirectional. Back and forth displacement due to cyclic shear stress during seismic shaking can be the source of shear energy. The boundary between units 9 and 10 has no evidence of mixing and brecciation. It is very sharp, resembling a shear surface rather than a stratigraphic contact. This could be explained considering relative sliding between two units which are decoupled one from the other along a very weak interface. In other words, seismic shaking would have determined relative displacement, but because of the fluidization of clay within unit 10, the two units were completely decoupled, producing localized shear along the stratigraphic interface. This sharp boundary might appear in conflict with the observation that material from unit 10 intruded into the overlying unit 9, forming clay-filled fissures. Nevertheless, this could be explained if relative shear overprints clay injection, also during the same deformation event when fluidization, clay injection and relative shear are semi-contemporaneous.

956 The conjugate fissures observed in map view (Fig. 8d) may suggest, at first glance, a tectonic
957 origin under strike-slip regime. The fissures have significant opening and form a conjugate system,
958 suggesting hybrid extensional shear fractures (e.g., Sibson, 1998) under horizontal σ1 bisecting the
959 acute angle and vertical σ2. Nevertheless, a regional-scale strike-slip stress regime is unlikely for
960 explaining the observed fissures, for three reasons: 1) the main tectonic feature in the trench is a NE-
961 dipping normal fault; 2) AMS results (sec. 4.2.4) are consistent with NE-trending extensional stress;
962 3) fractures and fissures are not localized in a fault zone, but are pervasively distributed within the
963 sedimentary layers, suggesting volumetric deformation. Cyclic shear stress due to seismic shaking
964 might have determined deviatoric stresses within the sheared layer, with local, temporary sub-
965 horizontal σ1 that, in combination with high fluid pressure, would have originated conjugate sets of
966 hybrid extensional shear fractures.
967 Different events of fracturing and fissuring occurred in the site, as testified by thoroughgoing
968 fissures that cut previously formed fissures and breccia layers. This evidence of recurrent events,
969 together with the above considerations on the possible occurrence of shaking-induced shear stress
970 within the sedimentary layers, suggest an earthquake-induced origin for the soft-sediment
971 deformation. The causative earthquakes should have nucleated not very far from the site, as suggested
972 by the dependency of the occurrence of liquefaction features with epicentral distance (e.g., Galli,
973 2000). Possibly, the earthquakes nucleated on the Anghiari normal fault, or on one of the Sansepolcro
974 basin system faults. The earthquakes should be relatively old, when sediments were soft and below
975 the water table, not in the present morphologic setting. Those ancient events occurred before tilting,
976 as the fissures are tilted with the hosting sedimentary layers. Moreover, despite the tilting, the 70°-
977 striking fissures remained subvertical (see stereonet in Fig. 6), indicating that rotation occurred
978 around an axis nearly orthogonal to that direction, which is nearly-parallel to the strike of the Anghiari
979 normal fault. This suggests that tilting is linked to progressive slip on the Anghiari fault.
980 In summary, the secondary features observed in the Villa Sterpeto trench suggest that the site was

affected by i) pervasive soft-sediment deformation under conditions of upward-directed pressurized fluids; ii) differential bedding-parallel shear, with effects at the boundary between units with different rheologies causing mixing or localized shear; iii) superposition of different consecutive deformation events; iv) shaking-induced shear stress due to strong earthquakes on the Sansepolcro basin fault system as the most plausible mechanism for their formation; and v) progressive tilting in the hanging wall of the Anghiari normal fault.

5.5 Seismogenic potential and average extensional rate in the Sansepolcro basin

We calculated the expected maximum magnitude (Mmax) from the mapped fault length using empirical regressions (Wells & Coppersmith, 1994; Leonard, 2014; Galli et al., 2008). From the obtained Mmax we derived the expected average (AD) and maximum displacement (MD). These values, summarized in the tab. 4, refer to two different rupture scenarios: S1) a rupture scenario which involves only the Anghiari fault (from the northern tip of the Micciano section to the southern tip of the Fighille section, total length ~12 km); S2) a rupture scenario which involves the whole Anghiari-Città di Castello main fault (total length ~25.5 km).

On average, the maximum expected magnitude derived from different empirical regressions ranges from 6.2 to 6.7 depending on the scenario. The displacements per event measured in the trenches (≥0.45 m estimated from the thickness of the wedges in the Villa Sterpeto trench and 0.18 to 0.52 m at the Todari roadcut) are comparable with the AD expected for S1 and are smaller, but not very different from the AD expected for S2. The values of displacement estimated from the wedges in the Villa Sterpeto trench (≥0.45 m) and the displacement related to E2_Tod (0.52 m) are also comparable with the expected MD for S1. This is consistent with the observation that the trenches are located in the zone with the greatest morphological expression along the Micciano fault section.

The data collected studying in depth the Anghiari fault can be used to sensibly improve the seismic

hazard assessment in the Sansepolcro basin. In fact, the fault parameters obtained with paleoseismological investigations are fundamental for fault-based seismic hazard assessments, especially where only a few macroseismic information are available from historical catalogs.

A key component in fault-based seismic hazard assessment is the slip rate. Our study provides slip rates based on chronologically constrained Late Quaternary - Holocene offsets. Nevertheless, some doubts arise when comparing the paleoseismological slip rates with the extensional rates from geodetic data. Anderlini et al. (2016) calculated GPS extension rates of ~2 mm/yr along a transect located ~30 km SE of the center of the Sansepolcro basin (across the Ponte Pattoli - Gubbio basins, see Fig. 1). In the Sansepolcro basin the extension is probably less than 2 mm/yr, as extension rate along the Apennines is known to decrease to the NW (Bennet et al., 2012; D'Agostino et al., 2009; D'Agostino, 2014; Anderlini et al., 2016). For example, in D'Agostino (2014) the strain rate across the central Sansepolcro basin (12 to 25 nstrain/yr) is ~40% less than the strain rate across the Ponte Pattoli - Gubbio basins (27 to 35 nstrain/yr). Therefore, the extension rate across the Sansepolcro basin can be estimated to be between 1.5 and 2.0 mm/yr. Even considering the highest calculated paleoseismological slip rate (0.35 mm/yr), the corresponding horizontal extension for an average fault dip of 45° (the Anghiari fault up to 3 km-depth) would be ~0.25 mm/yr, which is ~⅙ of the minimum estimated GPS extension. Assuming that a comparable amount of extension is accommodated by the Sansepolcro antithetic fault, there is still ~1 mm/yr of GPS extension to be explained. This suggests one or probably a combination of the following:

- a large part of the geodetic extension is accommodated by distributed deformation between major faults, not detectable by classical geologic investigations;
- we underestimate the slip rate as we possibly missed some secondary splaying faults and/or missed the sites of maximum displacement on the Anghiari fault;
- other splays of the ATF, such as the Sovara synthetic splay, accommodate part of the extension.

A work aimed at estimating the slip rate of the fault system systematically and at a wider scale, also using geologic and geomorphic markers covering a time range wider than that constrained in this work can help a better understanding of the extensional rate of the basin during its recent evolution.

Rupture Scenario	Length (km)	M max					AD (m)			MD (m)		W (km)		
		WC94 N	WC94 all	L14 DS	G08	Average	WC94 N	WC94 all	L14 DS	WC94 N	WC94 all	WC94 N	WC94 all	L14 DS
Anghiari Fault	12	6.28	6.33	6.27	6.13	6.25	0.32	0.37	0.5	0.49	0.54	11.47	10.38	8.62
Anghiari-Città di Castello main fault	25.5	6.72	6.71	6.79	6.63	6.71	0.60	0.68	0.91	1.20	1.11	16.25	13.73	14.17

Tab.4. Expected value of max magnitude (Mmax), average displacement (AD) and maximum displacement (MD) for two rupture scenarios involving the Anghiari fault or the whole Anghiari-Città di Castello main fault, according to the empirical relations by Wells and Coppersmith (1994) normal fault and all kinematics (WC94 N and WC94 all), Leonard 2014 deep slip (L14 DS) and Galli et al 2008 (G08).

5.6 Potential implications for activity and seismogenic behavior of a continental LANF

The evidence of surface faulting earthquakes along the Anghiari fault has potential implications in our understanding of the present activity and the seismogenic behavior of LANFs. The Anghiari fault is considered as the easternmost active synthetic splay of the ATF LANF by some authors (e.g., Barchi et al., 1998a; Brozzetti et al., 2009; Pucci et al., 2014; Bonini et al., 2016). The present activity of the ATF LANF was inferred mostly on the basis of microseismicity recorded SE of the Upper Tiber River valley, combined with seismic reflection data (Chiaraluce et al., 2007). The creeping versus seismogenic behavior, and the link with the Anghiari fault are the two major issues to address about the ATF LANF.

Although the frictional fault reactivation theory predicts that slip on LANF is extremely unlikely (Collettini, 2011), the ATF capacity to source moderate to strong earthquakes (i.e., $Mw \geq 6$) has been inferred from regional seismotectonic considerations. Brozzetti et al. (2009) claimed that the southern sector of the UTV (SSE of Città di Castello) is characterized by creeping, as suggested by the intense microseismicity and the lack of historical strong earthquakes, while the northern sector

(the Sansepolcro basin) is characterized by a seismogenic behavior, as suggested by the low microseismicity and the occurrence of strong historical earthquakes. High-resolution seismologic and geodetic data documented mixed-mode (seismic and aseismic) slip behavior along the ATF (Anderlini et al., 2016; Valoroso et al., 2017) and swarm-like events on its high-angle splay faults (Gualandi et al. 2017). Particularly, according to geodetic data, Anderlini et al. (2016) argue that the ATF LANF shows both locked and creeping patches, in agreement with the possibility to nucleate strong earthquakes in the Sansepolcro basin.

To address the issue of the link with the Anghiari fault, first we have to reconcile the ground surface observations and the deep model of this low-angle fault. At the surface, the Anghiari fault does not dip at low-angle. The dip is 48-60° in the Villa Sterpeto trench, from 40° to 74° in the Podere Todari road cut, and 46° and 70-80° (two synthetic splays) in the Anghiari trench (site A). In high-resolution shallow seismic reflection profiles, the fault dips ~53° up to depths of ~40 m (Micciano section, Villa Sterpeto site, Fig. 5) and ~51° up to depths of ~300 m (Anghiari-Motina section, Delle Donne et al., 2007). There are two possible interpretations about the link between the ATF LANF and the Anghiari fault:

1) the Anghiari fault dips steeply in the near-surface and becomes progressively less inclined at depth, soling into the ATF LANF at depths of 3-4 km as indicated in section A-A' of Fig. 1 (from Brozzetti et al., 2009);

2) the Anghiari fault dips steeply across the entire brittle crust and offset the ATF LANF.

The first option follows the classical model of LANF, and the second one is not yet supported by data. Such information would require additional investigations. There is no high-resolution geophysical data that can image with sufficient detail the fault intersection in the 3-5 km-depth interval, and there is no detailed aftershock data of earthquakes sufficiently large to illuminate an appreciable size of the Anghiari fault.

Field observations do not allow us to discriminate between these two hypotheses. The sedimentary succession in the hanging wall of the Anghiari fault is tilted against the fault and the tilting decreases from older to younger sediments (up to 30° the CTA beds; 5-15° the MTC beds, <5° the bottom of Late Pleistocene colluvium; Figs. 3, 6). Moreover, the CTA beds are tilted in the footwall of the Anghiari fault (Fig. S1, S3), suggesting that the Anghiari fault cuts through an already tilted succession in the hanging wall of the Sovara parallel fault. This evidence can suggest progressive hanging wall rollover due to listric faulting (e.g., Dula, 1991) during syn-tectonic sedimentation with an extensional model of imbricated listric normal faults rejuvenating in the direction of extension and soling into the same detachment level (Wernicke & Burchfiel, 1982). On the other hand, this would also be expected in a domino-style tilt block model of faulting (Wernicke & Burchfiel, 1982; Leeder & Gawthorpe, 1987) also observed in seismic reflection datasets (Jackson et al., 2017). Only high-resolution geophysical data can solve this uncertainty.

If the Anghiari fault is detaching on the ATF LANF at depths of ~3.5 km as in section A-A' of Fig. 1, its down-dip width is ~5 km (average dip of 45°). To generate a M≈6.2 earthquake, a rupture width (W) of about 9-11 km is expected (Wells & Coppersmith, 1994; Leonard, 2014). This implies that at least 4-5 km of the ruptured W should be on the ~25°-dipping ATF LANF (up to depths of 5-6 km). For a M≈6.7 earthquake, the expected W is about 13-16 km. Therefore, the expected down-dip ruptured portion of the LANF is about 8-11 km, which is close to the entire 25°-dipping ramp of the LANF in section A-A' of Fig. 1 (up to depths of ~7 km).

In synthesis, field data could support an active, seismogenic behavior of the ATF LANF, especially of the youngest and easternmost NE-dipping Anghiari splay and its down-dip continuation into the low-angle (dip≤25°) detachment. But high-resolution geophysical data in the 3-5 km-depth range appears essential for solving this issue.

Karlsson et al. (2021) came to similar conclusions by studying the case of the Cañada David detachment (Baja California-Mexico). They suggest that this severely misoriented LANF is capable

of nucleating strong surface faulting earthquakes, as well as other well-oriented faults in the system. As a possible mechanical explanation, they propose the "keystone fault hypothesis" formulated by Fletcher et al. (2016). The severely misoriented LANF would act as a keystone fault, able to regulate slip of other faults in the system. During interseismic loading, optimally-oriented faults would bleed off the excess shear stress in small slip events and creep determining continuous stress built-up on the keystone LANF until its seismogenic failure together with other high-angle faults in its hanging wall.

6. Conclusions

We revealed for the first time the slip history of the Anghiari fault, a 12 km-long normal fault considered in the literature to be a synthetic splay of a low-angle normal fault (Altotiberina LANF). The Anghiari fault displaces Lower-Middle Pleistocene to Holocene deposits and is capable of faulting the ground surface during strong earthquakes. The magnetic susceptibility anisotropy analysis indicates a continuously active extensional stress field. Pervasive soft-sediment deformation within the tilted Pleistocene deposits suggests repeating severe ground shaking due to strong earthquakes on the Sansepolcro basin normal fault system, and progressive tilting in the hanging wall of the Anghiari normal fault.

The most recent surface faulting earthquake (MRE_Tod) is compatible with the poorly-constrained 1458 earthquake, which damaged the Città di Castello and Sansepolcro towns within the Sansepolcro basin.

According to empirical regressions, the expected maximum magnitude is on average between 6.2 and 6.7, depending on the rupture scenario.

The paleoseismological slip rate of the Anghiari fault varies between 0.14 (over the last 7 ka) and 0.35 mm/yr (over the last 5 ka), depending on the considered fault section, with a mean value >0.2 mm/yr over the last 25 ka, measured in the Villa Sterpeto trench.

The mean recurrence interval ranges from about 2500 and 3200 years, depending on the different earthquakes age hypotheses considered. The coefficient of variation of the recurrence time is between about 0.6 and 0.9, suggesting a non-periodic behavior.

If the Anghiari fault is actually the surface expression of a LANF that steepens progressively within the shallowest 3-5 km of depths and breaches the ground, our work can be among the few ones worldwide documenting the geological evidence of an active and seismogenic LANF, suggesting that earthquakes on LANFs can be less rare than previously thought. Even though only a large seismogenic rupture can solve the issue unambiguously, very high-resolution geophysics in the 3-5 km-depth interval can help to prove the connection between the paleoseismological evidence of earthquake surface faulting and the deep low-angle plane, which is challenging for future research.

Acknowledgements

We are grateful to the Editor Laurent Jolivet, Zoë Mildon and the other anonymous reviewer who have significantly improved this manuscript with their suggestions and comments. This work was funded by “Ente Acque Umbre Toscane (EAUT), Arezzo, Italy", which is warmly acknowledged (Conventions 2019 and 2020 between EAUT and Universities of Chieti - Pescara - Resp.: P. Boncio - and Perugia - Resp.: F. Mirabella, code: MIRF2019EAUT and MIRFEAUT2021). This work is also partially funded by the EQTIME ANR-project (Resp.: L. Benedetti). We wish to thank F. Florindo (INGV) for the financial support in the paleomagnetic data collection and analysis to ADC. The AMS analysis was conducted at the INGV Paleomagnetism and Environmental Magnetism Laboratory. We also thank F. Carboni and A. Akimbekova for the support during GPR data collection, and M. Urbani and A. Sabatini for laser scanning of the trench in the Anghiari site A. Finally, CNES is warmly acknowledged for providing us the Pléaides satellite images through the ISIS program.

Data Availability Statement

All datasets presented in this study are included in the article and in the Supporting Information.

References

Anderlini, L., Serpelloni, E., & Belardinelli, M. (2016). Creep and locking of a low-angle normal fault: Insights from the Altotiberina fault in the Northern Apennines (Italy), Geophys. Res. Lett., 43, 221–4329, doi:10.1002/2016GL068604.

Argenti, P. (2004). Plio-Quaternary mammal fossiliferous sites of Umbria (Central Italy). Geol. Romana 37.

Barchi, M.R., (2010). The Neogene-Quaternary evolution of the Northern Apennines: crustal structure, style of deformation and seismicity, in: Beltrando, M., Peccerillo, A., Mattei, M., Conticelli, S., Doglioni, C. (Eds.), The Geology of Italy. Journal of Virtual Explorer. https://doi.org/10.3809/jvirtex.2009.00220

Barchi, M. R. & Ciaccio, M. G. (2009). Seismic images of an extensional basin, generated at the hanging wall of a low-angle normal fault: The case of the Sansepolcro basin (Central Italy). Tectonophysics, 479, 3–4, 285-293.

Barchi, M., Minelli, G. & Pialli, G. (1998 a). The CROP 03 Profile: a synthesis of results on deep structures of the Northern Apennines. Mem. Soc. Geol. It., 52, 383-400.

Barchi, M.R., De Feyter, A., Magnani, M.B., Minelli, G., Pialli, G., & Sotera, B.M. (1998b). Extensional tectonics in the Northern Apennines (Italy): Evidence from the CROP03 deep seismic reflection line. Mem. Soc. Geol. It., 52, 527-538.

Benedetti, L., ManigheG, I., Gaudemer, Y., Finkel, R., Malavieille, J., Pou, K., Arnold, M., Aumaître, G., Bourlès, D., & Keddadouche, K. (2013). Earthquake synchrony and clustering on

Fucino faults (Central Italy) as revealed from in situ ^{36}Cl exposure dating. Journal of Geophysical Research: Solid Earth, 118(9), 4948–4974. h^ps://doi.org/10.1002/jgrb.50299

Bennett, R.A., Serpelloni, E., Hreinsdóttir, S., Brandon, M.T., Buble, G., Basic, T., Casale, G., Cavaliere, A., Anzidei, M., Marjonovic, M., Minelli, G., Molli, G., & Montanari, A. (2012). Syn-convergent extension observed using the RETREAT GPS network, northern Apennines, Italy. Journal of Geophysical Research 117(B04408). https://doi.org/doi:10.1029/2011JB008744

Benvenuti M., Bonini M. & Moroni A. (2016) - Tectonic control on the Late Quaternary hydrography of the Upper Tiber Basin (Northern Apennines, Italy). Geomorphology, 269, 85-103.

Boncio, P., Brozzetti, F., & Lavecchia, G. (2000). Architecture and seismotectonic of a regional low-angle normal fault zone in Central Italy, Tectonics 19, 1038–1055.

Bonini M., Corti G., Delle Donne D., Sani F., Piccardi L., Vannucci G., Genco R., Martelli L. & Ripepe M. (2016). Seismic sources and stress transfer interaction among axial normal faults and external thrust fronts in the Northern Apennines (Italy): A working hypothesis based on the 1916–1920 time–space cluster of earthquakes, Tectonophysics, 680, 67-89, doi.org/10.1016/j.tecto.2016.04.045.

Borradaile, G.J. & Henry, B. (1997). Tectonic applications of magnetic susceptibility and its anisotropy. Earth Sci Rev 42(1–2):49–93. doi:10.1016/S0012-8252.

Borradaile, G.J. & Jackson, M. (2004). Anisotropy of magnetic susceptibility (AMS): magnetic petrofabrics of deformed rocks. In: Martı´n-Herna´ndez F, Lu¨neburg C, Aubourg C, Jackson M (eds) Magnetic Fabric methods and applications. Geol Soc Lond Spec Publ 238:299–360

Borradaile, G.J. (1988). Magnetic susceptibility, petrofabrics and strain. Tectonophysics 156(1–2):1–20. doi:10.1016/0040-1951.

Bronk Ramsey, C. (2009) Bayesian Analysis of Radiocarbon Dates, Radiocarbon, 51, 337–360, https://doi.org/10.1017/S0033822200033865.

Bronk Ramsey, C. (2008). Deposition models for chronological records. Quaternary Science Reviews, 27(1-2), 42–60, https://doi.org/10.1016/j.quascirev.2007.01.019.Bronk Ramsey, C. (1995). Radiocarbon Calibration and Analysis of Stratigraphy: The OxCal Program Radiocarbon 37(2) 425-430.

Brozzetti, F., Boncio, P., Lavecchia, G., & Pace, B. (2009). Present activity and seismogenic potential of a low-angle normal fault system (Cittá di Castello, Italy): Constraints from surface geology, seismic reflection data and seismicity, Tectonophysics 463, 31–46.

Caciagli, M., Pucci, S., Batlló, J., Cesca, S., & Braun, T. (2019). Did the Deadly 1917 Monterchi Earthquake Occur on the Low-Angle Alto Tiberina (Central Italy) Normal Fault? Seismological Research Letters, 90(3), 1131-1144.

Caricchi, C., Aldega, L., Barchi, M.R., Corrado, S., Grigo, D., Mirabella, F., & Zattin, M. (2015). Exhumation patterns along shallow low-angle normal faults: an example from the Altotiberina active fault system (Northern Apennines, Italy). Terra Nova 27, 312–321. https://doi.org/doi:10.1111/ter.12163.

Cattuto, C., Cencetti, C., Fisauli, & M., Gregori, L. (1995). I bacini Pleistocenici di Anghiari e Sansepolcro nell'alta valle del Tevere. Il Quaternario 8, 119–128.

Chiaraluce, L., Chiarabba, C., Collettini, C., Piccinini, D., Cocco, & M. (2007). Architecture and mechanics of an active low-angle normal fault: Alto Tiberina fault, northern Apennines, Italy, J. Geophys. Res. 112, doi: 10.1029/2007jb005015.

Ciangherotti, A., & Esu, D. (2000). Paleoecologic and biochronologic meaning of the early Pleistocene molluscan fauna from the Anghiari basin (Tiber River upper valley, central Italy). Boll. Soc. Paleontol. Ital. 39 (2), 217e224., 67e78.

Cinti, F. R., Pauselli, C., Livio, F., Ercoli, M., Brunori, C. A.,Ferrario, F., Volpe, R., Civico, R., Pantosti, D., Pinzi, S., DeMartini, P. M., Ventura, G., Alfonsi, L., Gambillara, R., & Michetti, A. M. (2015). Integrating multidisciplinary, multi-scale ge-ological and geophysical data to image the

1227 Castrovillari fault (Northern Calabria, Italy), Geophys. J. Int., 203, 1847–
1228 1863,https://doi.org/10.1093/gji/ggv404, 2015.
1229 Collettini, C. (2011). The mechanical paradox of low-angle normal faults: Current
1230 understanding and open questions. Tectonophysics, 510(3-4), 253-268.
1231 Cowie, P. A., Phillips, R. J., Roberts, G. P., McCaffrey, K., Zijerveld, L. J. J., Gregory, L. C.,
1232 Faure Walker, J., Wedmore, L. N. J., Dunai, T. J., Binnie, S. A., Freeman, S. P. H. T., Wilcken, K.,
1233 Shanks, R. P., Huismans, R. S., Papanikolaou, I., Michetti, A. M., & Wilkinson, M. (2017). Orogen-
1234 scale uplift in the central Italian Apennines drives episodic behaviour of earthquake faults. Sci. Rep.,
1235 7(November 2016), 1–10. https://doi.org/10.1038/srep44858
1236 D'Agostino, N., Mantenuto, S., D'Anastasio, E., Avallone, A., Selvaggi, G., Barchi, M.,
1237 Collettini, C., Radicioni, F., Stoppini, A., & Fastellini, F. (2009). Contemporary crustal extension in
1238 the Umbria-Marche Apennines from regional CGPS networks and comparison between geodetic and
1239 seismic deformation. Tectonophysics 476(1–2), 3–12.
1240 D'Agostino, N. (2014). Complete seismic release of tectonic strain and earthquake recurrence
1241 in the Apennines (Italy). Geophysical Research Letters, 41, 1155–1162.
1242 Delle Donne, D., Piccardi, L., Odum, J.K., Stephenson, W.J., & Williams, R.A. (2007). High-
1243 resolution shallow reflection seismic image and surface evidence of the Upper Tiber Basin active
1244 faults (Northern Apennines, Italy). Bollettino della Societá Geologica Italiana 126(2), 323–331.
1245 Dula, W. F. (1991). Geometric models of listric normal faults and rollover folds, AAPG Bull.,
1246 75, 1609-1625, doi.org/10.1306/0C9B29B1-1710-11D7-8645000102C1865D.
1247 Ellsworth, W.L., Matthews, M.V., Nadeau, R.M., Nishenko, S.P., Reasen- berg, P.A. &
1248 Simpson, R.W. (1999). A physically based earthquake recur- rence model for estimation of long-term
1249 earthquake probabilities, Open- File Rep., U.S. Geol. Surv. 99–522.

1250 Ercoli, M., Pauselli, C., Frigeri, A., Forte, E. & Costanzo, F. (2013). "Geophysical
1251 paleoseismology" through high resolution GPR data: A case of shallow faulting imaging in Central
1252 Italy, Journal of Applied Geophysics, 90, 27-40, https://doi.org/10.1016/j.jappgeo.2012.12.001.
1253 Ercoli, M., Pauselli, C., Cinti, F.R., Forte, E. & Volpe, R. (2015). Imaging of an active fault:
1254 Comparison between 3D GPR data and outcrops at the Castrovillari fault, Calabria, Italy,
1255 Interpretation, 3, SY57–SY66.
1256 Ercoli, M., Bizzarri, R., Baldanza, A., Bertinelli, A., Mercantili, D., Pauselli, C. (2021a). GPR
1257 Detection of Fossil Structures in Conductive Media Supported by FDTD Modelling and Attributes
1258 Analysis: An Example from Early Pleistocene Marine Clay at Bargiano Site (Central Italy).
1259 Geosciences, 11, 386. https://doi.org/10.3390/geosciences11090386.
1260 Ercoli, M., Cirillo, D., Pauselli, C., Jol, H. M., & Brozzetti, F. (2021b). Ground-penetrating
1261 radar signature of Quaternary faulting: a study from the Mt. Pollino region, southern Apennines, Italy,
1262 Solid Earth, 12, 2573–2596, https://doi.org/10.5194/se-12-2573-2021.
1263 Fletcher, J., Oskin, M. & Teran, O. (2016). The role of a keystone fault in triggering the
1264 complex El Mayor–Cucapah earthquake rupture. Nat. Geosci.9, 303–307. https://doi .org /10 .1038
1265 /ngeo2660.
1266 Forte, E., Pipan, M., Casabianca, D., Di Cuia, R. & Riva, A. (2012). Imaging and
1267 characterization of a carbonate hydrocarbon reservoir analogue using GPR attributes, J. Appl.
1268 Geophys, 81, 76-87.
1269 Galli, P. (2000). New empirical relationships between magnitude and distance for
1270 liquefaction, *Tectonophysics*, 324(3), 169-187. https://doi.org/10.1016/S0040-1951(00)00118-9
1271 Galli, P., Galadini, F., & Pantosti, D. (2008). Twenty years of paleoseismology in Italy, Earth
1272 Sci. Rev., 88(1–2), 89– 117, https://doi.org/10.1016/j. Earscirev.2008.01.001.

1273 Gualandi, A., Nichele, C., Serpelloni, E., Chiaraluce, L., Anderlini, L., Latorre, D.,
1274 Belardinelli, M.E. & Avouac, J.P. (2017). Aseismic deformation associated with an earthquake
1275 swarm in the northern Apennines (Italy), Geophys. Res. Lett., 44, doi:10.1002/2017GL073687.
1276 Heifetz, E., Agnon, A., & Marco, S. (2005). Soft sediment deformation by Kelvin Helmholtz
1277 Instability: A case 1314 from Dead Sea earthquakes. Earth Planet. Sci. Lett., 236, 497–504,
1278 doi:10.1016/j.epsl.2005.04.019.
1279 Hreinsdóttir S. & Bennett R. A. (2009). Active aseismic creep on the Alto Tiberina low-angle
1280 normal fault, Italy, Geology, 37, 683-686, doi: 10.1130/G30194A.1.
1281 Hrouda, F. (1982). Magnetic anisotropy of rocks and its application in geology and
1282 geophysics. Surv Geophys 5(1):37–82. doi:10.1007/BF01450244
1283 ISPRA. (2011). Carta Geologica d'Italia alla scala 1:50.0000, F. 289 Città di Castello. ISPRA,
1284 Roma.
1285 Jackson, C. A.-L., Bell, R. E., Rotevatn, A., & Tvedt, A. B. M. (2017). Techniques to
1286 determine the kinematics of synsedimentary normal faults and implications for fault growth models.
1287 Geol. Soc. London, Spec. Publ., SP439.22. https://doi.org/10.1144/SP439.22
1288 Karlsson, K. W., Rockwell, T. K., Fletcher, J. M., Figueiredo P. M., Cambron J. F., Gontz A.
1289 M., Naik, S.P., Lacan, P., Spelz, R. M., Owen, L. A., d, PeñaVilla, I.A. & Loya, R.L. (2021). Large
1290 Holocene ruptures on the Cañada David detachment, Baja California, Mexico; implications for the
1291 seismogenesis of low-angle normal faults. Earth andPlanetaryScienceLetters570(2021)117070.
1292 https://doi.org/10.1016/j.epsl.2021.117070
1293 Lavecchia, G., Bello, S., Andrenacci, C., Cirillo, D., Ferrarini, F., Vicentini, N., … &
1294 Brozzetti, F. (2022). Quaternary fault strain INdicators database-QUIN 1.0-first release from the
1295 Apennines of central Italy. Scientific Data, 9(1), 1-16.

Leeder, M. R., & Gawthorpe, R. L. (1987). Sedimentary models for extensional tilt-block/halfgraben basins. Geological Society, London, Special PublicaAons, 28(1), 139–152. https://doi.org/10.1144/GSL.SP.1987.028.01.11

Leonard, M. (2014). Self-consistent earthquake fault-scaling relations:Update and extension to stable continental strike-slip faults, Bull.Seismol. Soc. Am. 104, 2953–2965.

Levi, T., R. Weinberger, T. Aïfa, Y. Eyal, & Marco, S. (2006). Injection mechanism of clay-rich sediments into dikes during earthquakes, Geochem. Geophys. Geosyst., 7, Q12009, doi:10.1029/2006GC001410.

Maffione, M., Pucci, S., Sagnotti, L. & Speranza, F. (2012). Magnetic fabric of Pleistocene continental clays from the hanging-wall of an active low-angle normal fault (Altotiberina Fault, Italy). Int J Earth Sci (Geol Rundsch) (2012) 101:849–861 DOI 10.1007/s00531-011-0704-9.

Mantenuto, S. (2008). The Active Deformation in the Central-Northern Apennines (Abruzzo and Umbria-Marche Region, Italy) Through the Analysis of GPS Data (PhD thesis). University of Perugia, 156 pp.

Marco, S., Stein, M., Agnon, A., & Ron, H. (1996). Long term earthquake clustering: a 50,000-year paleoseismological record in the Dead Sea Graben. J. Geophys. Res. 101, 6179–6192, doi.org/10.1029/95JB01587C.

Martini I., Sagri M. & Colella A. (2001) Neogene-Quaternary basins of the inner Apennines and Calabria arc. In: Martini I. (Ed.), Anatomy of an Orogen - The Apennines and Adjacent Mediterranean Basins, Dordrecht, Netherlands: Kluwer Academic Publisher, 375-400.

Masini, F., & Sala, B. (2007). Large- and small-mammal distribution patterns and chronostratigraphic boundaries from the Late Pliocene to the Middle Pleistocene of the Italian peninsula. Quat. Int. 160, 43e56.

McCalpin, J.P. (2009) (Edited by). Paleoseismology, 2nd Edition. International Geophysics Series 95, Academic Press, Elsevier.

Mildon, Z. K., Roberts, G. P., Faure Walker, J. P., Beck, J., Papanikolaou, I., Michetti, A. M., Tonda, S., Iezzi, F., Campbell, L., McCaffrey K. J. W., Shanks, R., Sgambato, C., Robertson, J., Meschis, M., & Vittori, E. (2022). Surface faulting earthquake clustering controlled by fault and shear-zone interactions. Nature CommunicaAons, 13(1), 7126. https://doi.org/10.1038/s41467-022-34821-5

Mirabella, F., Brozzetti, F., Lupattelli, A., & Barchi, M.R. (2011) - Tectonic evolution of a low angle extensional fault system from restored cross sections in the northern Apennines (Italy). Tectonics, 30, TC6002.

Mirabella, F., Ciaccio, M.G., Barchi, M.R., & Merlini, S., (2004). The Gubbio normal fault (Central Italy): geometry, displacement distribution and tectonic evolution. Journal of Structural Geology 26, 2233–2249.

Montenat, C., Barrier, P., Ott d'Estevou, P. & Hibsch, C. (2007). Seismites: an attempt at critical analysis and classification, Sedimentary Geology, 196, 5–30, doi.org/10.1016/j.sedgeo.2006.08.004.

Montone, P., & Mariucci, M. T. (2016). The new release of the Italian contemporary stress map. Geophysical Journal International, 205(3), 1525-1531.

Oddone, E. (1918). Il terremoto dell'alta valle del Tevere del 26 aprile 1917. Boll. Soc. Sismol. It., 21, 9-27.

Pace, B., Peruzza, L., Lavecchia, G. & Boncio, P. (2006). Layered seismogenic source model and probabilistic seismic-hazard analyses in central Italy. Bulletin of the Seismological Society of America 96(1), 107–132.

Pace, B., Visini, F. & Peruzza, L. (2016). FiSH: MATLAB Tools to Turn Fault Data into Seismic-Hazard Models. Electronic Seismologist.

Pialli, G., Barchi, M., Minelli, G., (1998). Results of the CROP03 deep seismic reflection profile. Memorie della Societá Geologica Italiana 52, 654 pp.

Piccinini, D., Cattaneo, M., Chiarabba, C., Chiaraluce, L., De Martin, M., Di Bona, M., Moretti, M., Selvaggi, G., Augliera, P., Spallarossa, D., Ferretti, G., Michelini, A., Govoni, A., Di Bartolomeo, P., Romanelli, & M., Fabbri, J. (2003). A microseismic study in a low seismicity area of Italy: the Citta di Castello 2000 e 2001 experiment. Ann. Geophys. 46 (6), 1315e1324.

Pondrelli, S. (2002). European-Mediterranean Regional Centroid-Moment Tensors Catalog (RCMT) [Dataset].

Pucci, S., Mirabella, F., Pazzaglia, F., Barchi, M.R., Melelli, L., Tuccimei, P., Soligo, M., & Saccucci, L. (2014). Interaction between regional and local tectonic forcing along a complex Quaternary extensional basin: Upper Tiber Valley, Northern Apennines, Italy. Quaternary Science Reviews 102, 111–132. http://dx.doi.org/10.1016/j.quascirev.2014.08.009.

Reimer, P.J., Austin, W.E.N., Bard, E., Bayliss, A., Blackwell, P.G., Bronk Ramsey, C., Butzin,M., Cheng, H., Edwards, R.L., Friedrich, M., Grootes, P.M., Guilderson, T.P., Hajdas, I.,Heaton, T.J., Hogg, A.G., Hughen, K.A., Kromer, B., Manning, S.W., Muscheler, R.,J. Fan et al. Palmer, J.G., Pearson, C., van der Plicht, J., Reimer, R.W., Richards, D.A., Scott, E.M.,Southon, J.R., Turney, C.S.M., Wacker, L., Adolphi, F., Büntgen, U., Capano, M., Fahrni,S.M., Fogtmann-Schulz, A., Friedrich, R., Köhler, P., Kudsk, S., Miyake, F., Olsen, J.,Reinig, F., Sakamoto, M., Sookdeo & A., Talamo, S. (2020). The IntCal20 Northern Hemisphere Radiocarbon Age Calibration Curve (0-55 cal kBP): Radiocarbon, v. 62, p. 725–757, doi:10.1017/RDC.2020.41.

Rovida, A., Locati, M., Camassi, R., Lolli, B., Gasperini, P., & Antonucci, A. (2022). Catalogo Parametrico dei Terremoti Italiani (CPTI15), versione 4.0. Istituto Nazionale di Geofisica e Vulcanologia (INGV). https://doi.org/10.13127/CPTI/CPTI15.4.

Sani F., Bonini M., Piccardi L., Vannucci G., Delle Donne D., Benvenuti M., Moratt i G., Corti G., Montanari D., Sedda L. & Tanini C. (2009). Late Pliocene–Quaternary evolution of outermost hinterland basins of the Northern Apennines (Italy), and their relevance to active tectonics. Tectonophysics, 476, 336-356.

1371 Schlagenhauf, A., ManigheG, I., BenedeG, L., Gaudemer, Y., Finkel, R., Malavieille, J., &
1372 Pou, K. (2011). Earthquake supercycles in Central Italy, inferred from 36Cl exposure dating. Earth
1373 Planet. Sci. LeG., 307(3–4), 487–500. https://doi.org/10.1016/j.epsl.2011.05.022
1374 Serpelloni, E., Anzidei, M., Baldi, P., Casula, G., Galvani, A., 2005. Crustal velocity and
1375 strain-rate fields in Italy and surrounding regions: new results from the analysis of permanent and
1376 ISPRA non-permanent GPS networks. Geophysical Journal International 161, 861–880.
1377 https://doi.org/10.1111/j.1365-246X.2005.02618.x
1378 Sibson, R.H. (1998). Brittle failure mode plots for compressional and extensional tectonic
1379 regimes. *Journal of Structural Geology*, 20(5), 655-660. https://doi.org/10.1016/S0191-
1380 8141(98)00116-3
1381 Taner, M.T., Koehler, F. & Sheriff, R.E. (1979). Complex Seismic Trace Analysis,
1382 Geophysics, 44, 1041.
1383 Tarling, D.H. & Hrouda, F. (1993). The magnetic anisotropy of rocks. Chapman and Hall,
1384 London 217 pp.
1385 Tarquini, S., Isola, I., Favalli, M., Mazzarini, F., Bisson, M., Pareschi, M.T. & Boschi, E.
1386 (2007). TINITALY/01: a new Triangular Irregular Network of Italy. Annals of Geophysics 50(3),
1387 407–425.
1388 Testa, A., Valentini, A., Boncio, P., Pace, B., Visini, F., Mirabella, F., & Pauselli, C. (2021)
1389 Probabilistic fault displacement hazard analysis of the Anghiari - Città di Castello normal fault (Italy).
1390 Ital. J. Geosci., Vol. 140, No. 3 (2021), pp. 327-346, 13 figs., 1 tab.
1391 (https://doi.org/10.3301/IJG.2021.07).
1392 Valoroso, L., Chiaraluce, L., Di Stefano, R., & Monachesi, G. (2017). Mixed-mode slip
1393 behavior of the Altotiberina low-angle normal fault system (Northern Apennines, Italy) through high-
1394 resolution earthquake locations and repeating events. Journal of Geophysical Research: Solid
1395 Earth,122,10,220–10,240. https://doi.org/10.1002/2017JB014607.

Van Loon, A. J. (2009). Soft-sediment deformation structures in siliciclastic sediments: an overview, Geologos, 15 (1), 3–55.

Visini, F. & Pace, B. (2014). Insights on a key parameter of earthquake forecasting, the coefficient of variation of the recurrence time, using a simple earthquake simulator, Seismol. Res. Lett., 85(3), 703–713.

Webber, S., Norton, K. P., Little, T.A., Wallace, L. M., Elias, S. (2018). How fast can low-angle normal faults slip? Insights from cosmogenic exposure dating of the active Mai'iu fault, Papua New Guinea. Geology 46, 227 - 230. https://doi.org/10.1130/G39736.1

Wells, D. L., & Coppersmith, K. J. (1994). New empirical relationships among magnitude, rupture length, rupture width, rupture area, and surface displacement. Bulletin of the Seismological Society of America, 84, 974-1002.

Wernicke, B. & Burchfiel, B. C. (1982). Modes of extension tectonics, Journal of Structural Geology, 4, 105-115, doi.org/10.1016/0191-8141(82)90021-9.

References from the supporting information

Borradaile, G.J. & Henry, B. (1997). Tectonic applications of magnetic susceptibility and its anisotropy. Earth Sci Rev 42(1–2):49–93. doi:10.1016/S0012-8252.

Borradaile, G.J. & Jackson, M. (2004). Anisotropy of magnetic susceptibility (AMS): magnetic petrofabrics of deformed rocks. In: Martı´n-Herna´ndez F, Lu¨neburg C, Aubourg C, Jackson M (eds) Magnetic Fabric methods and applications. Geol Soc Lond Spec Publ 238:299–360

Borradaile, G.J. (1988). Magnetic susceptibility, petrofabrics and strain.Tectonophysics 156(1–2):1–20. doi:10.1016/0040-1951.

Bronk Ramsey, C. (2009) Bayesian Analysis of Radiocarbon Dates, Radiocarbon, 51, 337–360, https://doi.org/10.1017/S0033822200033865.

Bronk Ramsey, C. (1995). Radiocarbon Calibration and Analysis of Stratigraphy: The OxCal Program Radiocarbon 37(2) 425-430.

Ercoli, M., Pauselli, C., Cinti, F.R., Forte, E. & Volpe, R. (2015). Imaging of an active fault: Comparison between 3D GPR data and outcrops at the Castrovillari fault, Calabria, Italy, Interpretation, 3, SY57–SY66.

Ercoli, M., Pauselli, C., Frigeri, A., Forte, E. & Costanzo, F. (2014). 3-D GPR data analysis for high-resolution imaging of shallow subsurface faults: the Mt Vettore case study (Central Apennines, Italy), Geophysical Journal International, 198, 1, 609-621, https://doi.org/10.1093/gji/ggu156.

Hrouda, F. (1982). Magnetic anisotropy of rocks and its application in geology and geophysics. Surv Geophys 5(1):37–82. doi:10.1007/BF01450244

Jelinek, V. (1978). Statistical processing of magnetic susceptibility on groups of specimens. Stud Geophys Geod 22:50–62.

Jol, H.M. Ground Penetrating Radar Theory and Applications (2009). Jol, H.M., Ed., Elsevier Science: Amsterdam, The Netherlands, 524 pp.

Palmer, D. (1980). The Generalized Reciprocal Method of seismic refraction interpretation, Society of Exploration Geophysicists, 113 pp.

Reimer, P.J., Austin, W.E.N., Bard, E., Bayliss, A., Blackwell, P.G., Bronk Ramsey, C., Butzin,M., Cheng, H., Edwards, R.L., Friedrich, M., Grootes, P.M., Guilderson, T.P., Hajdas, I.,Heaton, T.J., Hogg, A.G., Hughen, K.A., Kromer, B., Manning, S.W., Muscheler, R.,J. Fan et al. Palmer, J.G., Pearson, C., van der Plicht, J., Reimer, R.W., Richards, D.A., Scott, E.M.,Southon, J.R., Turney, C.S.M., Wacker, L., Adolphi, F., Büntgen, U., Capano, M., Fahrni,S.M., Fogtmann-Schulz,

A., Friedrich, R., Köhler, P., Kudsk, S., Miyake, F., Olsen, J.,Reinig, F., Sakamoto, M., Sookdeo & A., Talamo, S. (2020). The IntCal20 Northern Hemisphere Radiocarbon Age Calibration Curve (0-55 cal kBP): Radiocarbon, v. 62, p. 725–757, doi:10.1017/RDC.2020.41.

Rockwell, T. K., Meltzner, A. J., Haaker, E. C. & Madugo, D. (2022). The late Holocene history ofLake Cahuilla: two thousand years of repeated fillings within the Salton Trough, ImperialValley, California. Quat. Sci. Rev. 282, 107456. Tarling, D.H. & Hrouda, F. (1993). The magnetic anisotropy of rocks. Chapman and Hall, London 217 pp.

Tarquini, S., Vinci, S., Favalli, M., Doumaz, F., Fornaciai, A., & Nannipieri, L. (2012). Release of a 10-m-resolution DEM for the Italian territory: Comparison with global-coverage DEMs and anaglyph-mode exploration via the web, Computers & Geosciences, 38, 168-170. https://doi.org/10.1016/j.cageo.2011.04.018

Yilmaz, O. (2001). Seismic Data Analysis: Processing, Inversion, & Interpretation of Seismic Data, Investigations in Geophysics. No. 10 (Vols. 1& 2). Society of Exploration Geophysicists, Tulsa, USA.

Supporting Information for

Paleoseismological constraints of the Anghiari fault in the Altotiberina low-angle normal fault system (Northern Apennines, Italy)

A. Testa[1]; P. Boncio[1]; S. Baize[2]; F. Mirabella[3]; S. Pucci[4]; B. Pace[1]; M. Riesner[5]; C. Pauselli[3], M. Ercoli[3], L. Benedetti[5], A. Di Chiara[4]; R. Civico[4]

1. InGEO Department, Università degli Studi G. d'Annunzio Chieti e Pescara, Italy.
2. IRSN/PRP-ENV/SCAN/BERSSIN, Institut de Radioprotection et de Sˆuret´e Nucl´eaire, Fontenay-Aux-Roses 92262, France.
3. Dipartimento di Fisica e Geologia, Università di Perugia, Italy.
4. Instituto di Geofisica e Vulcanologia,Via di Vigna Murata 605, 00143 Rome, Italy.
5. University of Aix Marseille, CNRS, IRD, INRAE, CEREGE, Aix-en-Provence, France

Contents of this file

Additional Supporting Information

Report of Radiocarbon Dating Analysis

Introduction

The supporting information include additional information regarding the geophysical acquisition and processing (Text S1); additional information about the anisotropy of magnetic susceptibility methodology (Text S2); the detailed description of the stratigraphy of the trenches (Text S3); the orthophoto-mosaic of each trench (Figure S1 to S4); the results of the analysis of the anisotropy of magnetic susceptibility (Fig. S5 and Tab. S1); the results of the radiocarbon datings and the calibration of uncalibrated ages provided by the Laboratory Plateforme Nationale LMC14 (France) (Fig. S6).

Text S1.

Geophysical Acquisition and processing:

Text S1.

Geophysical Acquisition and processing:

Seismic Reflection (SR): A sledgehammer source of 8 kg was used to produce a vertical impact on a metallic plate located on the ground, together with a trigger geophone, and shooting every 2 m (123 shots in total). The acquisition was accomplished using a roll-along scheme, using a channel overlap of 24 and achieving 336 CDP with a max fold number of 42.Upon setting up the geometry, the conventional processing scheme included a data quality control (QC) of the shot gathers and a first break picking across 8860 traces, using the Generalised Reciprocal Method (GRM, Palmer, 1980), and inverted via software Rayfract v. 3.34, obtaining a velocity model with the lowest Root-Mean Square (RMS) value after 19 iterations. Seismic reflections were processed using the commercial software RadExPro to obtain a stack seismic profile with improved S/N ratio (Yilmaz, 2001), achieved after applying these steps: Automatic Gain Control, Top Mute, Spectral Shaping, Bandpass and F-K filters, Spiking Deconvolution, Statics, Velocity Analysis, Normal MoveOut Correction and Stacking, FX-Deconvolution and Depth Conversion (using a smoothed RMS velocity model).

Ground Penetrating Radar (GPR): A 100 ns time window with 1024 samples/trace, and a trace spacing of 0.02 m was used. The processing flow used is based on the schemes already reported in Ercoli et al. (2014, 2015), thus encompassing conventional steps (Jol, 2009) such as trace editing/killing and coordinate/elevation correction, time-zero alignment and correction, dewow and bandpass filtering, amplitude recovery, horizontal smoothing filter, topographic correction and time-to depth conversion (Vem = 0.01 m/ns-1).

Electrical Resistivity Tomography (ERT): The survey has been carried out using 56 one-meter spaced electrodes with both the Wenner-Schlumberger and Dipole-Dipole configuration., for an investigation depth of about 8-10 m.
Data processing was carried out using the ZondRes2D software.

Text S2.

Anisotropy of Magnetic susceptibility

The AMS is a second order tensor ellipsoid characterized by the orientation and magnitude of its principal axes (kmax, kint and kmin, being the maximum, intermediate, and minimum susceptibility axes, respectively, Tarling & Hrouda 1993). The relative magnitude of its axes defines the shape of the AMS ellipsoid: (1) isotropic (kmax=kint=kmin) when crystals have no preferred orientation or when strongly magnetic grains have a random distribution; (2) oblate (kmax≈kint >> kmin) when crystal alignment defines a foliation plane; (3) prolate (kmax>>kint ≈ kmin) when crystal alignment defines a lineation plane; or (4) triaxial (kmin < kint < kmax). The strength of anisotropy can be described by the corrected anisotropy degree (PJ; Jelınek, 1978), where PJ = 1.0 indicates an isotropic fabric and, for example, PJ = 1.05 indicates 5% anisotropy. The shape of the ellipsoid is described by the shape parameter (T), where −1.0 < T < 1.0 with positive/negative values of T indicate oblate/prolate fabrics, respectively (Jelınek, 1978). AMS can be used to distinguish an undeformed sedimentary rock (typically with a weakly oblate fabric) from a weakly to strongly deformed rock (a weakly or strongly prolate or triaxial ellipsoid; see reviews by Hrouda, 1982; Borradaile, 1988; Tarling & Hrouda, 1993; Borradaile & Henry, 1997; Borradaile & Jackson, 2004).

Text S3

Stratigraphy of the Villa Sterpeto trench

The stratigraphy of the Villa Sterpeto trench is described in detail below, starting from the oldest unit.

Unit 11 is made of whitish, grain-supported, polygenic dense conglomerate, with light brown sandy matrix, dominant carbonate and few sandstone and quartz clasts. Sub-rounded pebbles and cobbles prevail but there are also rare boulders. The clasts are imbricated showing a westward flow provenance and the layers apparently dip from 5° to 17° toward west. This unit represents the most prominent relief cropping out only in the footwall of the fault zone.

Unit 10 is made of blue-gray stiff clay, with ochraceous mottling. The upper part is characterized by the presence of calcium carbonate concretions. This unit is the oldest found in the fault hanging wall. The boundary with the overlaying unit 9 is sharp and

dips ~12° westward.

Unit 9 consists of dark yellowish-orange, very dense sand with rare arenaceous pebbles and interbedded layers of black quartz clasts. This unit is featured by several layer-parallel and layer-perpendicular fissures, infilled by gray clay from unit 10. The transition to the upper unit 8 is characterized by breccia horizons and flame structures described in the main text.

Unit 8 is a deeply pedogenised unit that can be divided into three sub-units, from bottom to the top: 8c) very dusky red to blackish red clay without manganese coating; 8b) dark brown to moderate reddish-brown clay with few manganese coating; 8a) dark reddish brown to dusky brown clay with abundant manganese coating. All the three subunits are crossed by layer-perpendicular fractures. This unit is unconformably overlayed by units 1 and 2 and interfingers with unit 7 westward. The maximum thickness of unit 8 is ~6 m. Unit 7 consists of dark yellowish orange to dark brown, very gravelly, very stiff clay with abundant manganese coatings. The clasts are sub-angular pebbles and cobbles and rare boulders, mainly made of altered sandstones and rare black clasts. This unit is featured by irregularly shaped veins filled by gray to green clay. The maximum visible thickness is ~1.5 m.

Unit 6 is a dusky brown paedogenetic horizon (paleosol) made of sandy clay with polygenic, sub-angular pebbles and cobbles and manganese coatings and nodules. The boundary with the underlying unit 7 is marked by a 5 cm-thick clayey layer. The age of unit 6 is constrained by the sample VS_C01 (23,126 – 22,626 BCE, Fig 7, Tab. 1). Unit 5 is a light to moderate brown sandy clay with sparse polygenic, sub-angular pebbles and cobbles. This unit overlays unit 6 and is overlayed by unit 3. The age of unit 5 is constrained by four samples collected within this unit for radiocarbon dating (bulk organic fraction, Tab. 1). From the top to the bottom the radiocarbon dating gave

ages of 12,054 – 11,656 BCE (VS_C12); 13,677 – 13,351 BCE (VS_C13); 15,863 – 15,198 BCE (VS_C03) and 14,106 – 13,717 BCE (VS_C02). The ages are all coherent with each other, except for VS_C02 and VS_C03 which are inverted.
Unit 4 is a colluvial deposit formed by dark yellowish-brown, polygenic, grain-supported, dense gravel with sandy matrix sourced from unit 11. This unit is directly faulted against unit 11 and inter-fingers with unit 5.

Unit 3 is a reddish-brown paleosol with sub-angular blocky structure, deriving from paedogenetic alteration of the underlying unit 5. The age of unit 3 is constrained by the sample VS_C06bis (4,551 – 4,363 BCE; Fig. 7).

Unit 2 is a young colluvium with pottery shards, divided into two sub-units: 2a) moderate brown clayey sand with horizons of polygenic pebbles and cobbles; 2b) moderate brown gravel with polygenic pebbles and cobbles.

Unit 1 is an anthropogenic deposit made of heterometric gravel from unit 11, with light brown clayey sand matrix. It contains pottery shards and modern anthropogenic backfill.

Stratigraphy of the Todari site

The stratigraphy of the Todari site is described in detail below, starting from the oldest unit.

Unit 7 is made of very dense ochraceous fine sand with strata and lenses of dense polygenic, grain-supported gravel with sub-rounded calcareous and subordinately sandstone pebbles and rare cobbles. In the footwall of the main fault, unit 7 is directly overlayed by the present-day soil (unit 1a). The uppermost part of unit 7 is the eluvium of the unit, consisting of light olive brown sandy clay.

In the hanging wall of the main fault, unit 7 is located at the bottom of the outcrop and it is overlayed by unit 6.

Unit 6 is composed of grayish olive to dark yellowish brown very stiff clay with polyhedral structure and sparse calcium carbonate nodules. This unit is a clayey paleosol developed on top of unit 7. It crops out between the main fault and the antithetic fault. According to the sample Tod_C01bis, the age of this unit is between 5,318 and 5,084 BCE (Tab. 1.).

Unit 5 is made of moderate olive brown to grayish olive, moderately firm, thinly laminated clay, and it crops out only in the hanging wall of the main fault. The bottom of this unit is the contact with unit 6, while on top it is covered by units 4 and 1. The unit 5 has an age between the samples Tod_C02 (3,468 - 3,561 BCE) and Tod_C03 (928 - 810 BCE) (Tab. 1).

Unit 4 is made of moderate brown to dark yellowish-brown, soft to firm clay with red and gray mottling and sparse millimetric to centimetric calcium carbonate nodules. This unit constitutes a colluvial wedge delimited by unit 5 at the bottom, units 3 and 1 at the top and the filled fissure (FF) to the west. Sample Tod_C06, collected close to the base of the unit, has an age of 668 - 874 CE.

Unit FF is the infill of a large fissure topped by unit 3. This unit is mainly made of sand with sparse sub-rounded and sub-centimetric calcareous clasts. Sample Tod_C05, collected within the unit, has an age of 1,408 - 1,460 BCE.

Unit 3 is a colluvial wedge bounded by units 1 and 2 at the top, unit 4 at the bottom, and the filled fissure and unit 7 to the west. It consists of dusky yellow to light olive brown, slightly clayey sand with sparse fine gravel and interbedded layers of calcareous sub-rounded and flat small pebbles iso-oriented as the wedge. There are no dated

samples in this unit, but it is younger than unit FF and older than the unit 2. Its age is, therefore, between 1,408 - 1,460 CE (Tod_C05) and 1,495 - 1,656 CE (Tod_C04).

Unit 2 is a grayish brown to dusky brown soft clayey colluvial wedge with calcareous sub-rounded and flattened medium pebbles and granules, iso-oriented as the wedge. This unit is interfingered with the unit 1 and is bounded at the bottom by unit 3 and at the top by unit 1. Sample Tod_C04, collected within unit 2, has an age of 1,495 - 1,656 CE.

Unit 1 is divided into two sub-units: 1a) modern soil made of grayish brown to dark yellowish-brown clay and sandy clay with sparse calcareous pebbles and calcium carbonates nodules; 1b) moderate yellowish brown soft sandy clay with sparse fine gravel and rare pebbles. The base of 1b is marked by a layer of grayish brown to yellowish gray sand. Subunit 1a is the youngest, while subunit 1b interfingers with unit 2, and therefore should have the same age.

Stratigraphy of the Anghiari trench site A

The stratigraphy of the Anghiari trench site A is illustrated in detail below, starting from the oldest unit.

Unit 11 is made of plastic, firm gray-bluish clay, passing upward to stiff and fractured, orange to yellowish, silt and sandy-silt. The unit possibly belongs to the FIG synthem.

Unit 10 is made of grain-supported gravel with a sandy matrix. The clasts are mainly made of calcareous, sub-rounded pebbles and cobbles. This unit has an erosive base and belongs to the CTA synthem.

Unit 9 corresponds to the remnant of an alluvial deposit and is made of grain-supported gravel with a light brown sandy matrix. The clasts are mainly calcareous, sub-rounded pebbles and cobbles. This unit has an erosive base and covers a pedogenised surface.

Unit 8 is a colluvium made of dark yellow to greenish massive, fractured, firm and moderately plastic slightly sandy clay.

Unit 7 is a colluvium made of olive gray massive, fractured, stiff to firm and moderately plastic silty and gravelly clay. The clasts are mainly calcareous large pebbles and cobbles.

Unit 6 is a colluvium made of stiff and plastic grayish slightly silty clay with orange to yellow mottling. It contains rare sandstone sub-angular to sub-rounded granules and cobbles and frequent charcoal. The base is characterized by a discontinuous gravelly clay horizon.

Unit 5 is a lacustrine-palustrine unit made of grayish firm and plastic slightly sandy clay. It contains rare sub-angular to sub-rounded pebbles and cobbles of sandstone. Based on stratigraphic considerations (see below), we interpret the base of this unit (between fault zones 3 and 1; Fig. 10 of the main text), as an abnormal contact, probably a gravitational slide along the former slope. Unit 4b is an olive gray pedogenized colluvial deposit made of fractured, firm, and moderately plastic slightly sandy clay, containing fine gravel and charcoal. It is darker in the upper part. This unit crops out both in the hanging wall and in the footwall of the main fault zone. The age of this unit has been constrained thanks to radiocarbon dating of charcoal. The two samples, collected in the footwall (sample TA_C3) and in the hanging wall (sample TA_C8) of the main fault zone, have ages of 3,076 - 2,899 BCE and 3,351 - 3,096 BCE, respectively.

Unit 4a is a colluvial deposit made of matrix-supported gravel and brown to green-yellowish firm, moderately plastic sandy-silty clay. The clasts are mainly calcareous, sub-rounded to sub-angular granules to large pebbles. Contains pottery shards (sample

TA_C4p) of the IV-VI century CE (ages of pottery shards are from archaeological evaluation by O. Menozzi, Univ. of Chieti-Pescara, pers. comm.).

Unit 3b is a colluvial deposit made of matrix supported gravel with brown-yellowish fine sand and silty matrix. The clasts are mainly calcareous large pebbles and cobbles.

Unit 3a is a colluvial deposit made of brown-yellowish clay and silt with rare granules and coarse sand. It contains charcoal and pottery shards (sample TA_C9p) of the V-VII century CE (ages of pottery shards are from archaeological evaluation by O. Menozzi, Univ. of Chieti-Pescara, pers. comm.). The radiocarbon age of the sample TA_C6 is between 571 and 651 CE, in agreement with the age of the archeological findings.

Unit 2 is a colluvial slope-derived deposit made of matrix-supported gravel with a brown yellowish slightly clayey sandy and silty matrix. The clasts are mainly sub-rounded pebbles and cobbles. It contains reworked pottery shards (samples TA_7p, TA_10p, TA_14p) of the VII-XIV century CE (ages of pottery shards are from archaeological evaluation by O. Menozzi, Univ. of Chieti-Pescara, pers. comm.).

Unit 1 is a modern anthropogenic backfill with plastic remains and very young pottery fragments.

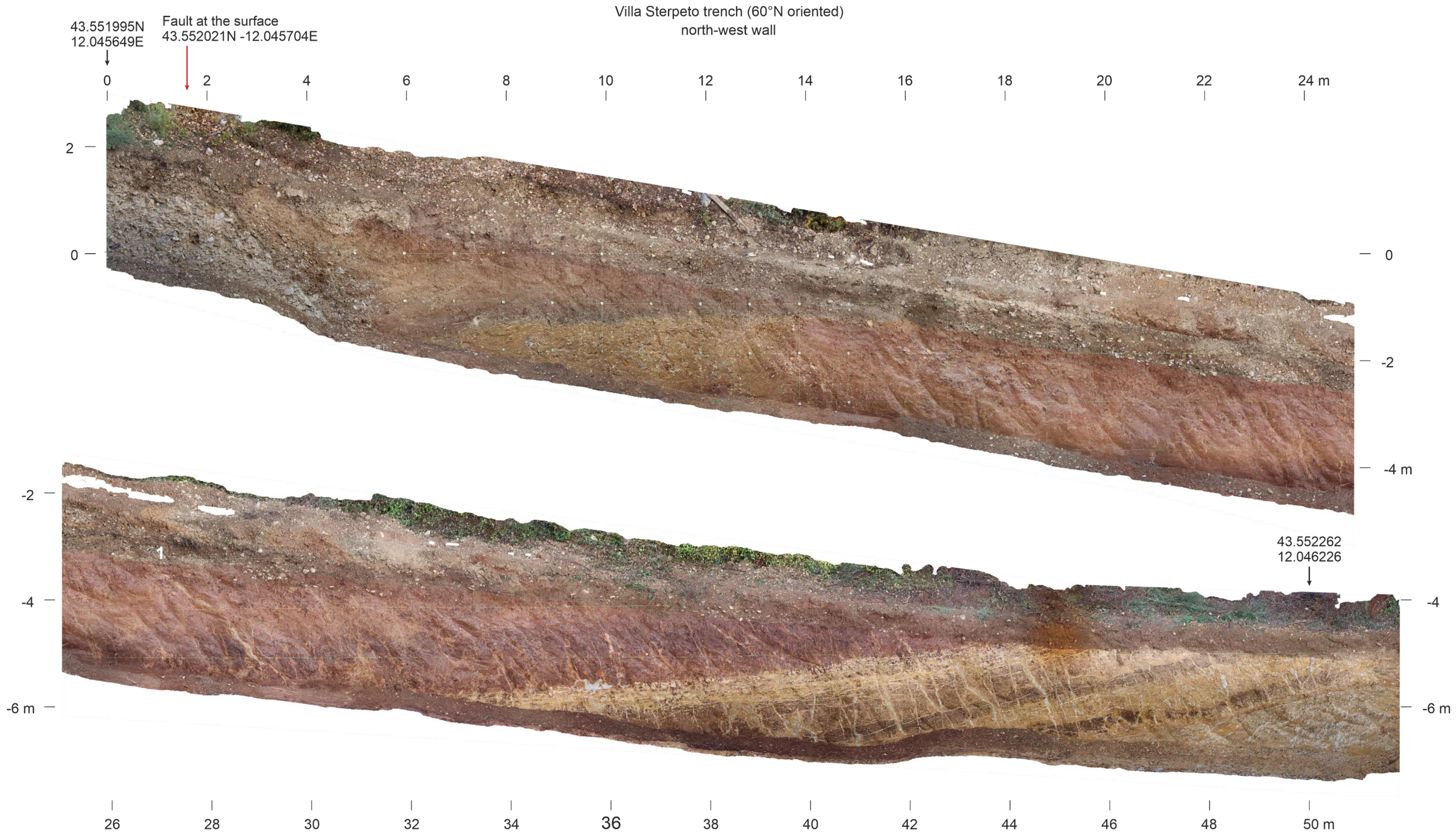

Fig S1. Orthophotomosaic of the north-west wall of the Villa Sterpeto trench.

Fig S2. Orthophotomosaic of the south-east facing Todari roadcut

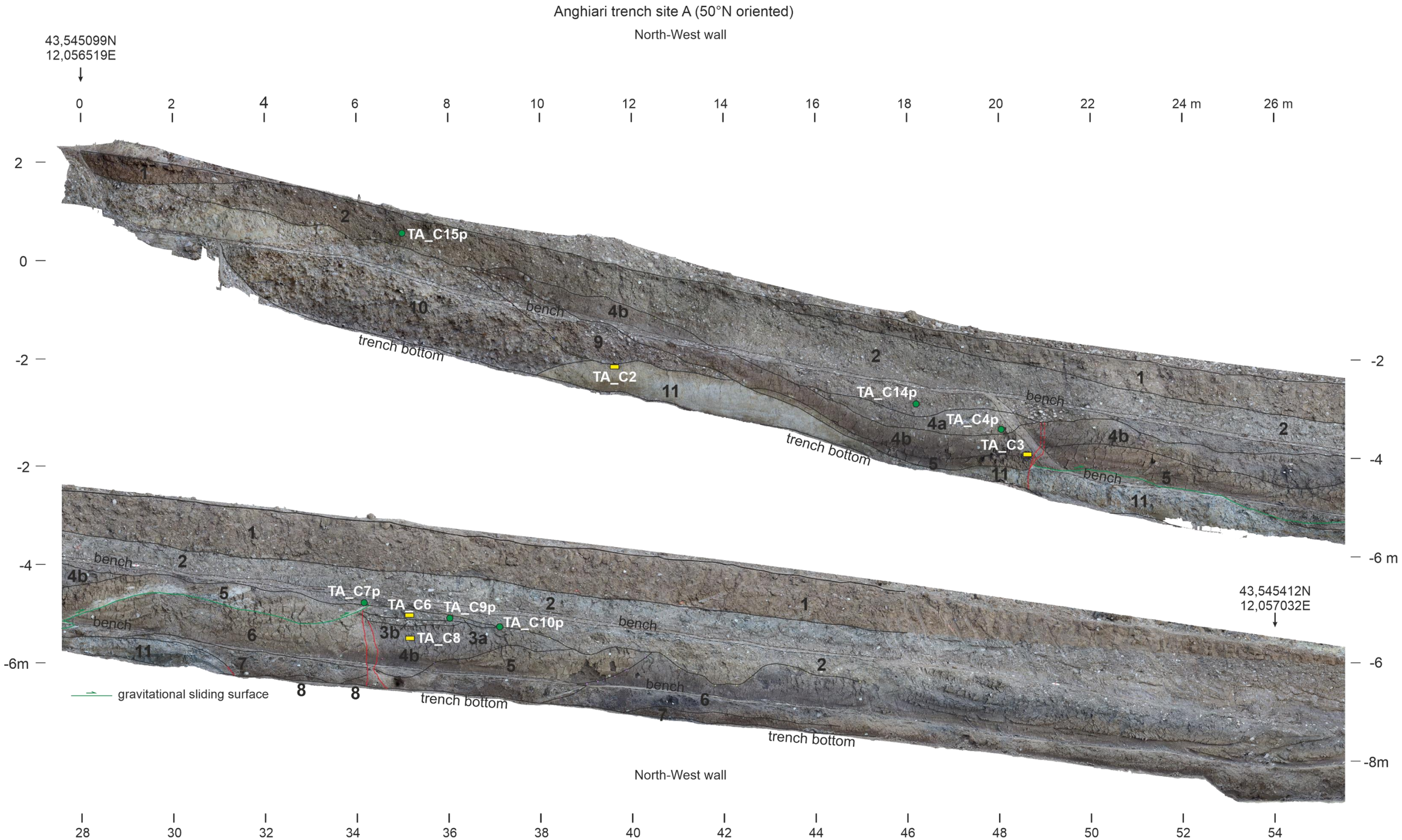

Fig S3. Interpreted orthophotomosaic of the north-west wall of the Anghiari trench site A. Details on the stratigraphic units and samples, text S3 and in the main text.

Supporting Information Figure S4
Orthophoto mosaic of the Anghiari trench site B

1: Anthropic backfill; 2: Olive-brown firm and moderately plastic slightly gravelly clay, with black clasts and manganese patinas. Contains gravelly clay with orange to yellowish mottling and sub angular to sub rounded pebbles; 3: Yellow to greenish firm and highly plastic clay with sparse sandstone pebbles and cobbles and orange to yellow mottling.4: yellow-brown clayey gravel made of sub angular and altered sandstone pebbles and cobbles. Black and quartz clasts are also present. The base is marked by a 20 cm thick gray to yellowish layer of clayey to gravelly dense silt. The top corresponds to a gravitational sliding surface filled with gray clay;5: grain supported gravel with a brown to yellowish sandy clay matrix. The gravel is made of subrounded pebbles and rare cobbles. Black patinas are abundant.

Fig S4. Interpreted orthophotomosaic of the north-west wall of the Anghiari trench site B.

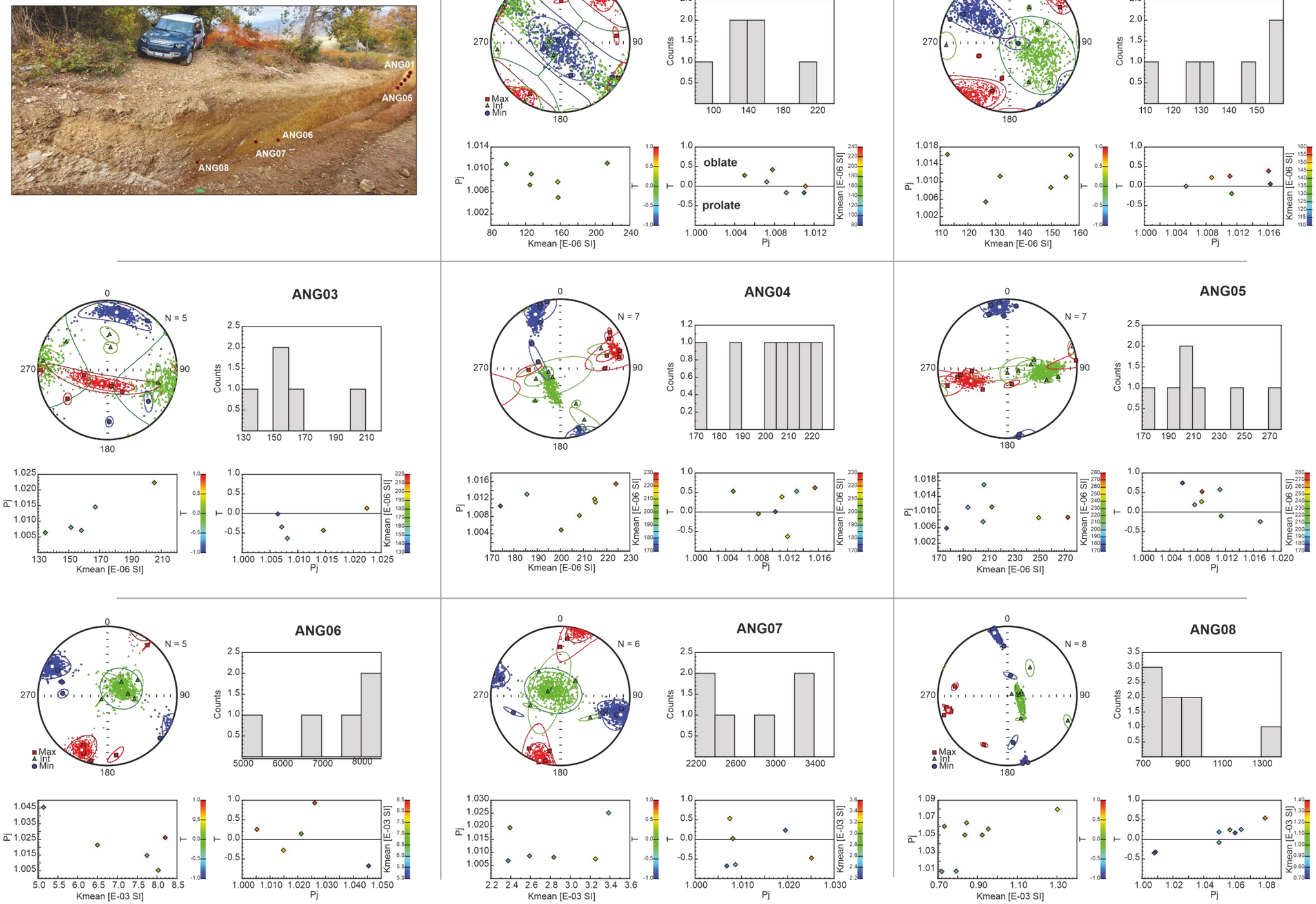

Fig S5. Results of the AMS analyses, including the stereonet with the sample data points, a mean tensor and the confidence ellipses; the distribution of the mean susceptibility per sample, the Pj parameter vs mean susceptibility and then Pj vs T

Site	N	Mean k [x 10^{-6} SI]	Normalised principal susceptibilities			Principal axes			Jelinek parameters	
			k_{max}	k_{int}	k_{min}	k_{max}	k_{int}	k_{min}	P_J	T
ANG01	6	146.2	1.002	0.999	0.998	040/05	309/05	171/82	1.004	-0.442
ANG02	6	138.8	1.004	1	0.996	215/10	112/51	313/41	1.007	-0.017
ANG03	5	163.3	1.004	1	0.996	103/73	100/04	009/17	1.008	0.106
ANG04	6	207.7	1.005	1	0.995	071/19	204/69	334/19	1.01	0.018
ANG05	7	216.9	1.004	1.001	0.995	252/44	094/44	353/11	1.009	0.351
ANG06	5	7126	1.01	0.999	0.991	205/15	062/71	298/10	1.019	-0.104
ANG07	6	2805	1.005	0.999	0.995	198/03	304/79	107/10	1.01	-0.165
ANG08	8	887.9	1.2	1.002	0.978	256/13	108/74	348/08	1.043	0.124

Table S1. Anisotropy of the magnetic susceptibility (AMS) results for the Anghiari section. Site indicates the site (block) name, N is the number of samples measured from each site; k is the mean susceptibility; the normalized principal susceptibilities are the second order tensor axis, where kmax is the maximum axis of susceptibility, kint is the intermediate, and the kmin is the minimum axis. The principal axis orientation of each axis are also reported as azimuth and dip. The Jelinek parameters indicate the grade of anisotropy, Pj, and the shape, T.

Addictional Supporting Information. Complete reports of the radiocarbon dating analyses by Beta Analytic Testing Laboratory and Laboratory Plateforme Nationale LMC14 (France).
The uncalibrated ages of the samples tested by the Laboratory Plateforme Nationale LMC14 have been calibrated by us using OxCal v4.4 (Bronk Ramsey, 1995 and 2009) and the IntCal20 atmospheric calibration model (Reimer et al, 2020), as reported in the last page of this document.
(Sample codes and location in Tab. 1 of the main text).

Order of the samples:

TA_C3
TA_C6
TA_C8
Tod_C01bis
Tod_C02
Tod_C03
Tod_C04
Tod_C05
Tod_C06
VS_C01
VS_C12
VS_C13
VS_C02
VS_C03
VS_C06bis
VS_C07
VS_C08

Beta Analytic, Inc.
4985 SW 74th Court
Miami, FL 33155 USA
Tel: 305-667-5167
Fax: 305-663-0964
info@betalabservices.com

ISO/IEC 17025:2017-Accredited Testing Laboratory

REPORT OF RADIOCARBON DATING ANALYSES

Paolo Boncio

Universita G.D Annunzio Chieti Pescara

Report Date: August 24, 2022

Material Received: August 04, 2022

Laboratory Number	Sample Code Number	Conventional Radiocarbon Age (BP) or Percent Modern Carbon (pMC) & Stable Isotopes
Beta - 635167	**TA_C3**	**4350 +/- 30 BP** IRMS δ13C: -30.0 o/oo

(92.8%)	**3027 - 2899 cal BC**	**(4976 - 4848 cal BP)**
(2.6%)	**3076 - 3064 cal BC**	**(5025 - 5013 cal BP)**

Submitter Material: Charcoal
Pretreatment: (charred material) acid/alkali/acid
Analyzed Material: Charred material
Analysis Service: AMS-Standard delivery
Percent Modern Carbon: 58.19 +/- 0.22 pMC
Fraction Modern Carbon: 0.5819 +/- 0.0022
D14C: -418.14 +/- 2.17 o/oo
Δ14C: -423.18 +/- 2.17 o/oo (1950:2022)
Measured Radiocarbon Age: (without d13C correction): 4430 +/- 30 BP
Calibration: BetaCal4.20: HPD method: INTCAL20

Results are ISO/IEC-17025:2017 accredited. No subcontracting or student labor was used in the analyses. All work was done at Beta in 4 in-house NEC accelerator mass spectrometers and 4 Thermo IRMSs. The "Conventional Radiocarbon Age" was calculated using the Libby half (5568 years), is corrected for total isotopic fraction and was used for calendar calibration where applicable. The Age is rounded to the nearest 10 years and is reported as radiocarbon years before present (BP), "present" = AD 1950. Results greater than the modern reference are reported as percent modern carbon (pMC). The modern reference standard was 95% the 14C signature of NIST SRM 4990C (oxalic acid). Quoted errors are 1 sigma counting statistics. Calculated sigmas less than 30 BP on the Conventional Radiocarbon Age are conservatively rounded up to 30. d13C values are on the material itself (not the AMS 13C). d13C and 15N values are relative to VPDB. References for calendar calibrations are cited at the bottom of calibration graph pages.

Calibration of Radiocarbon Age to Calendar Years

(High Probability Density Range Method (HPD): INTCAL20)

(Variables: d13C = -30.0 o/oo)

Laboratory number **Beta-635167**

Conventional radiocarbon age **4350 ± 30 BP**

95.4% probability

(92.8%)	3027 - 2899 cal BC	(4976 - 4848 cal BP)
(2.6%)	3076 - 3064 cal BC	(5025 - 5013 cal BP)

68.2% probability

(28.9%)	3011 - 2976 cal BC	(4960 - 4925 cal BP)
(25.4%)	2939 - 2910 cal BC	(4888 - 4859 cal BP)
(13.9%)	2966 - 2946 cal BC	(4915 - 4895 cal BP)

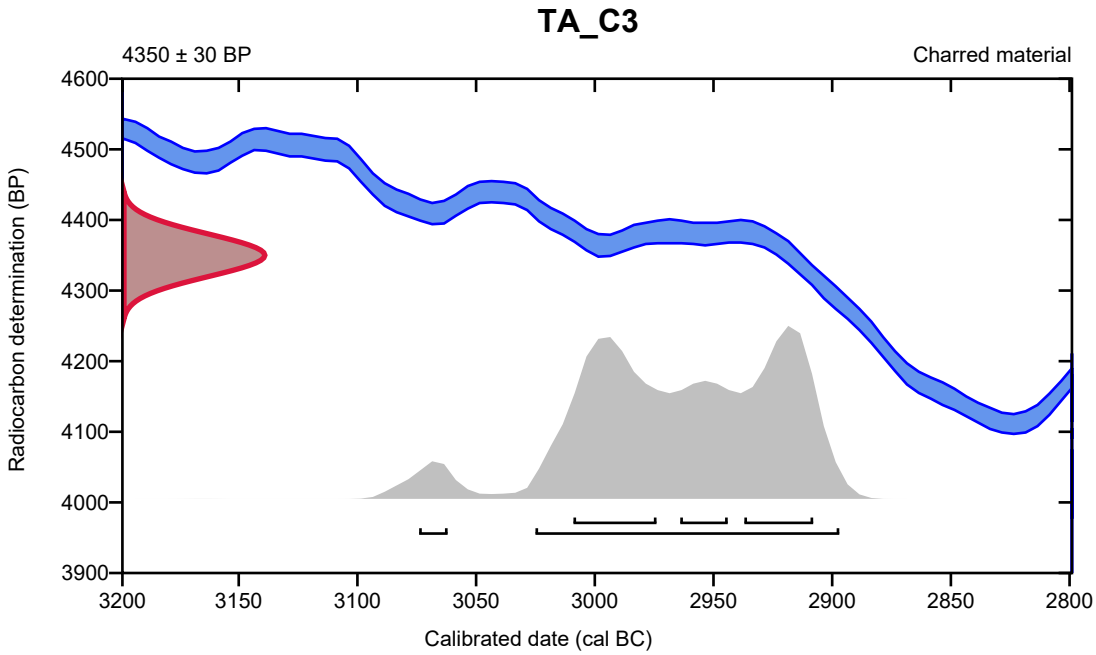

Database used

INTCAL20

References

References to Probability Method

Bronk Ramsey, C. (2009). Bayesian analysis of radiocarbon dates. Radiocarbon, 51(1), 337-360.

References to Database INTCAL20

Reimer, et al., 2020, Radiocarbon 62(4):725-757.

Beta Analytic, Inc.
4985 SW 74th Court
Miami, FL 33155 USA
Tel: 305-667-5167
Fax: 305-663-0964
info@betalabservices.com

ISO/IEC 17025:2017-Accredited Testing Laboratory

REPORT OF RADIOCARBON DATING ANALYSES

Paolo Boncio

Universita G.D Annunzio Chieti Pescara

Report Date: August 24, 2022

Material Received: August 04, 2022

Laboratory Number	Sample Code Number	Conventional Radiocarbon Age (BP) or Percent Modern Carbon (pMC) & Stable Isotopes	
Beta - 635168	**TA_C6**	**1450 +/- 30 BP**	IRMS δ13C: -24.6 o/oo
(95.4%)	**571 - 651 cal AD**	**(1379 - 1299 cal BP)**	

Submitter Material: Charcoal
Pretreatment: (charred material) acid/alkali/acid
Analyzed Material: Charred material
Analysis Service: AMS-Standard delivery
Percent Modern Carbon: 83.48 +/- 0.31 pMC
Fraction Modern Carbon: 0.8348 +/- 0.0031
D14C: -165.15 +/- 3.12 o/oo
Δ14C: -172.39 +/- 3.12 o/oo (1950:2022)
Measured Radiocarbon Age: (without d13C correction): 1440 +/- 30 BP
Calibration: BetaCal4.20: HPD method: INTCAL20

Results are ISO/IEC-17025:2017 accredited. No sub-contracting or student labor was used in the analyses. All work was done at Beta in 4 in-house NEC accelerator mass spectrometers and 4 Thermo IRMSs. The "Conventional Radiocarbon Age" was calculated using the Libby half-life (5568 years), is corrected for total isotopic fraction and was used for calendar calibration where applicable. The Age is rounded to the nearest 10 years and is reported as radiocarbon years before present (BP), "present" = AD 1950. Results greater than the modern reference are reported as percent modern carbon (pMC). The modern reference standard was 95% the 14C signature of NIST SRM-4990C (oxalic acid). Quoted errors are 1 sigma counting statistics. Calculated sigmas less than 30 BP on the Conventional Radiocarbon Age are conservatively rounded up to 30. d13C values are on the material itself (not the AMS d13C). d13C and d15N values are relative to VPDB. References for calendar calibrations are cited at the bottom of calibration graph pages.

Calibration of Radiocarbon Age to Calendar Years

(High Probability Density Range Method (HPD): INTCAL20)

(Variables: d13C = -24.6 o/oo)

Laboratory number **Beta-635168**

Conventional radiocarbon age **1450 ± 30 BP**

95.4% probability

(95.4%) 571 - 651 cal AD (1379 - 1299 cal BP)

68.2% probability

(68.2%) 598 - 643 cal AD (1352 - 1307 cal BP)

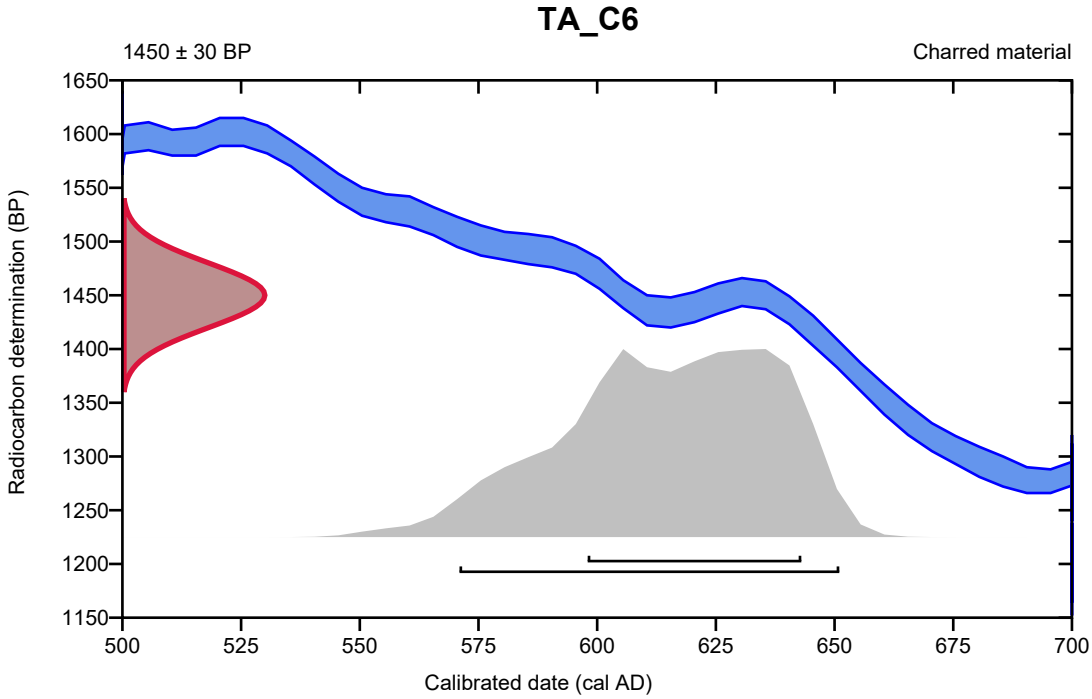

Database used

INTCAL20

References

References to Probability Method

Bronk Ramsey, C. (2009). Bayesian analysis of radiocarbon dates. Radiocarbon, 51(1), 337-360.

References to Database INTCAL20

Reimer, et al., 2020, Radiocarbon 62(4):725-757.

Beta Analytic Radiocarbon Dating Laboratory

4985 S.W. 74th Court, Miami, Florida 33155 • Tel: (305)667-5167 • Fax: (305)663-0964 • Email: beta@radiocarbon.com

Beta Analytic, Inc.
4985 SW 74th Court
Miami, FL 33155 USA
Tel: 305-667-5167
Fax: 305-663-0964
info@betalabservices.com

ISO/IEC 17025:2017-Accredited Testing Laboratory

REPORT OF RADIOCARBON DATING ANALYSES

Paolo Boncio

Universita G.D Annunzio Chieti Pescara

Report Date: August 24, 2022

Material Received: August 04, 2022

Laboratory Number	Sample Code Number	Conventional Radiocarbon Age (BP) or Percent Modern Carbon (pMC) & Stable Isotopes	
Beta - 635169	**TA_C8**	**4500 +/- 30 BP**	IRMS δ13C: -25.6 o/oo

(95.4%) 3351 - 3096 cal BC (5300 - 5045 cal BP)

Submitter Material: Charcoal
Pretreatment: (charred material) acid/alkali/acid
Analyzed Material: Charred material
Analysis Service: AMS-Standard delivery
Percent Modern Carbon: 57.11 +/- 0.21 pMC
Fraction Modern Carbon: 0.5711 +/- 0.0021
D14C: -428.90 +/- 2.13 o/oo
Δ14C: -433.85 +/- 2.13 o/oo (1950:2022)
Measured Radiocarbon Age: (without d13C correction): 4510 +/- 30 BP
Calibration: BetaCal4.20: HPD method: INTCAL20

Results are ISO/IEC-17025:2017 accredited. No sub-contracting or student labor was used in the analyses. All work was done at Beta in 4 in-house NEC accelerator mass spectrometers and 4 Thermo IRMSs. The "Conventional Radiocarbon Age" was calculated using the Libby half-life (5568 years), is corrected for total isotopic fraction and was used for calendar calibration where applicable. The Age is rounded to the nearest 10 years and is reported as radiocarbon years before present (BP), "present" = AD 1950. Results greater than the modern reference are reported as percent modern carbon (pMC). The modern reference standard was 95% the 14C signature of NIST SRM-4990C (oxalic acid). Quoted errors are 1 sigma counting statistics. Calculated sigmas less than 30 BP on the Conventional Radiocarbon Age are conservatively rounded up to 30. d13C values are on the material itself (not the AMS d13C). d13C and d15N values are relative to VPDB. References for calendar calibrations are cited at the bottom of calibration graph pages.

Calibration of Radiocarbon Age to Calendar Years

(High Probability Density Range Method (HPD): INTCAL20)

(Variables: d13C = -25.6 o/oo)

Laboratory number **Beta-635169**

Conventional radiocarbon age **4500 ± 30 BP**

95.4% probability

(95.4%)	3351 - 3096 cal BC	(5300 - 5045 cal BP)

68.2% probability

(39.1%)	3194 - 3104 cal BC	(5143 - 5053 cal BP)
(13.8%)	3241 - 3210 cal BC	(5190 - 5159 cal BP)
(10.5%)	3337 - 3313 cal BC	(5286 - 5262 cal BP)
(4.8%)	3297 - 3285 cal BC	(5246 - 5234 cal BP)

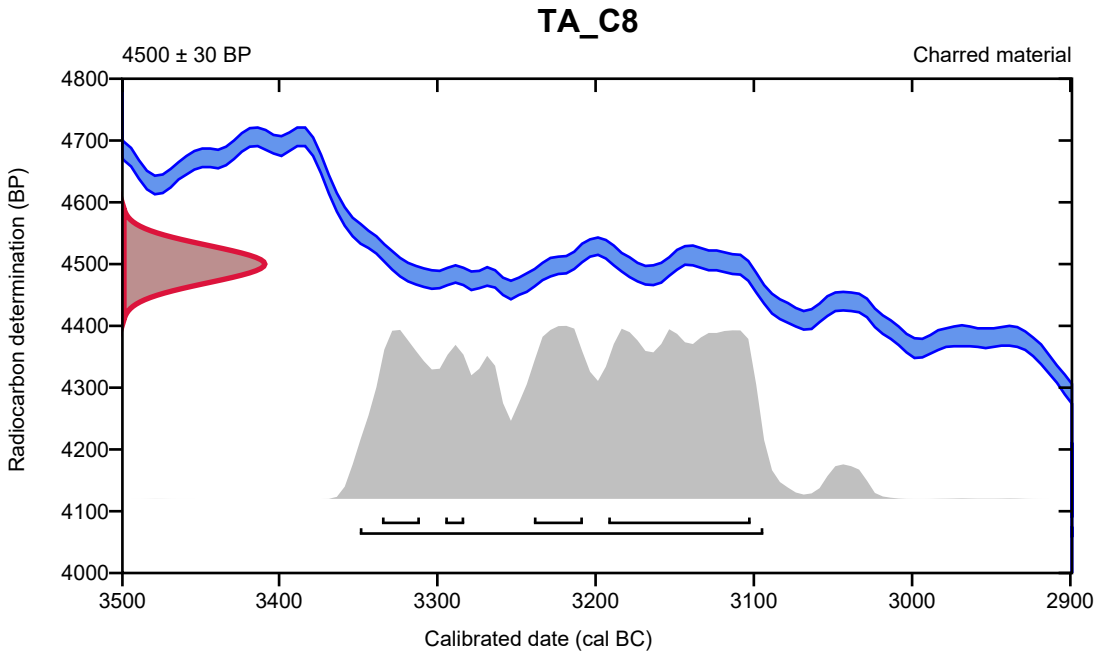

Database used

INTCAL20

References

References to Probability Method

Bronk Ramsey, C. (2009). Bayesian analysis of radiocarbon dates. Radiocarbon, 51(1), 337-360.

References to Database INTCAL20

Reimer, et al., 2020, Radiocarbon 62(4):725-757.

Beta Analytic Radiocarbon Dating Laboratory

4985 S.W. 74th Court, Miami, Florida 33155 • Tel: (305)667-5167 • Fax: (305)663-0964 • Email: beta@radiocarbon.com

Beta Analytic, Inc.
4985 SW 74th Court
Miami, FL 33155 USA
Tel: 305-667-5167
Fax: 305-663-0964
info@betalabservices.com

ISO/IEC 17025:2017-Accredited Testing Laboratory

REPORT OF RADIOCARBON DATING ANALYSES

Paolo Boncio

Universita G.D Annunzio Chieti Pescara

Report Date: January 03, 2022

Material Received: December 09, 2021

Laboratory Number	Sample Code Number	Conventional Radiocarbon Age (BP) or Percent Modern Carbon (pMC) & Stable Isotopes	
Beta - 612441	**Tod_C01bis**	**6270 +/- 30 BP**	IRMS δ13C:b-24.4 o/oo

(91.0%)	**5318 - 5207 cal BC**	**(7267 - 7156 cal BP)**
(4.0%)	**5162 - 5125 cal BC**	**(7111 - 7074 cal BP)**
(0.4%)	**5089 - 5084 cal BC**	**(7038 - 7033 cal BP)**

Submitter Material: Organic Sediment/Gyttja
Pretreatment: (organic sediment) acid washes
Analyzed Material: Organic sediment
Analysis Service: AMS-Standard delivery
Percent Modern Carbon: 45.82 +/- 0.17 pMC
Fraction Modern Carbon: 0.4582 +/- 0.0017
D14C: -541.84 +/- 1.71 o/oo
Δ14C: -545.81 +/- 1.71 o/oo (1950:2022)
Measured Radiocarbon Age: (without d13C correction): 6260 +/- 30 BP
Calibration: BetaCal4.20: HPD method: INTCAL20

Results are ISO/IEC-17025:2017 accredited. No sub-contracting or student labor was used in the analyses. All work was done at Beta in 4 in-house NEC accelerator mass spectrometers and 4 Thermo IRMSs. The "Conventional Radiocarbon Age" was calculated using the Libby half-life (5568 years), is corrected for total isotopic fraction and was used for calendar calibration where applicable. The Age is rounded to the nearest 10 years and is reported as radiocarbon years before present (BP), "present" = AD 1950. Results greater than the modern reference are reported as percent modern carbon (pMC). The modern reference standard was 95% the 14C signature of NIST SRM-4990C (oxalic acid). Quoted errors are 1 sigma counting statistics. Calculated sigmas less than 30 BP on the Conventional Radiocarbon Age are conservatively rounded up to 30. d13C values are on the material itself (not the AMS d13C). d13C and d15N values are relative to VPDB. References for calendar calibrations are cited at the bottom of calibration graph pages.

Calibration of Radiocarbon Age to Calendar Years

(High Probability Density Range Method (HPD): INTCAL20)

(Variables: d13C = -24.4 o/oo)

Laboratory number **Beta-612441**

Conventional radiocarbon age **6270 ± 30 BP**

95.4% probability

(91%)	5318 - 5207 cal BC	(7267 - 7156 cal BP)
(4%)	5162 - 5125 cal BC	(7111 - 7074 cal BP)
(0.4%)	5089 - 5084 cal BC	(7038 - 7033 cal BP)

68.2% probability

(57.2%)	5303 - 5250 cal BC	(7252 - 7199 cal BP)
(11%)	5226 - 5214 cal BC	(7175 - 7163 cal BP)

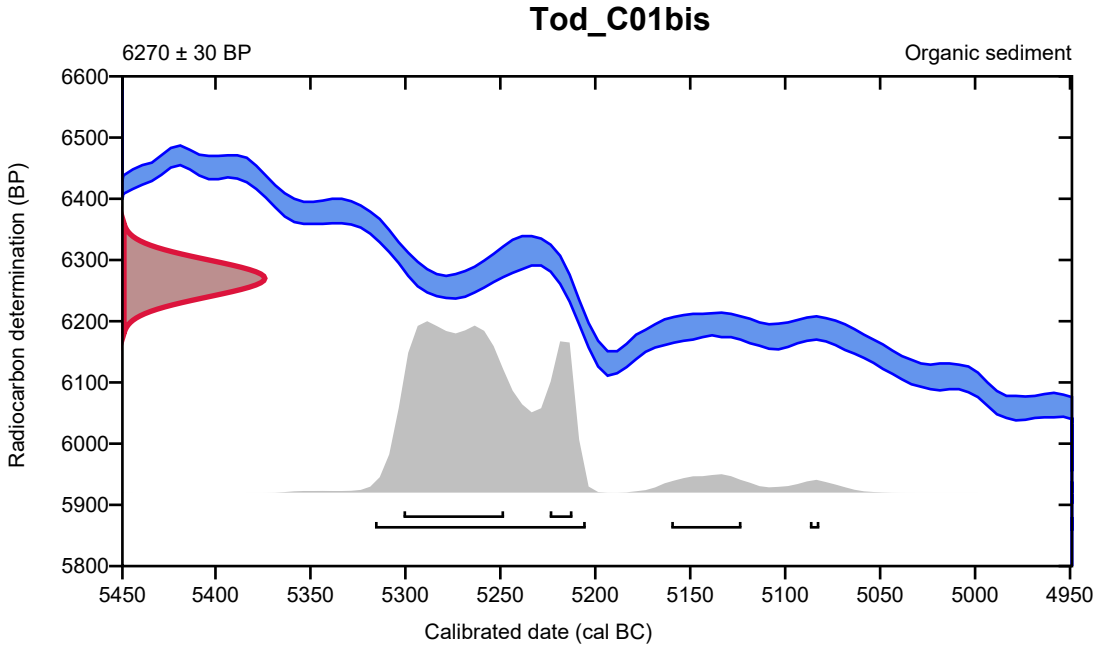

Database used

INTCAL20

References

References to Probability Method

Bronk Ramsey, C. (2009). Bayesian analysis of radiocarbon dates. Radiocarbon, 51(1), 337-360.

References to Database INTCAL20

Reimer, et al., 2020, Radiocarbon 62(4):725-757.

Beta Analytic Radiocarbon Dating Laboratory

4985 S.W. 74th Court, Miami, Florida 33155 • Tel: (305)667-5167 • Fax: (305)663-0964 • Email: beta@radiocarbon.com

Beta Analytic, Inc.
4985 SW 74th Court
Miami, FL 33155 USA
Tel: 305-667-5167
Fax: 305-663-0964
info@betalabservices.com

ISO/IEC 17025:2017-Accredited Testing Laboratory

REPORT OF RADIOCARBON DATING ANALYSES

Paolo Boncio

Universita G.D Annunzio Chieti Pescara

Report Date: January 03, 2022

Material Received: December 09, 2021

Laboratory Number	Sample Code Number	Conventional Radiocarbon Age (BP) or Percent Modern Carbon (pMC) & Stable Isotopes	
Beta - 612442	**Tod_C02**	**4710 +/- 30 BP**	IRMS δ13C: -24.3 o/oo

(54.8%)	**3468 - 3373 cal BC**	**(5417 - 5322 cal BP)**
(24.1%)	**3534 - 3489 cal BC**	**(5483 - 5438 cal BP)**
(14.9%)	**3626 - 3576 cal BC**	**(5575 - 5525 cal BP)**
(1.6%)	**3571 - 3561 cal BC**	**(5520 - 5510 cal BP)**

Submitter Material: Organic Sediment/Gyttja
Pretreatment: (organic sediment) acid washes
Analyzed Material: Organic sediment
Analysis Service: AMS-Standard delivery
Percent Modern Carbon: 55.64 +/- 0.21 pMC
Fraction Modern Carbon: 0.5564 +/- 0.0021
D14C: -443.64 +/- 2.08 o/oo
Δ14C: -448.46 +/- 2.08 o/oo (1950:2022)
Measured Radiocarbon Age: (without d13C correction): 4700 +/- 30 BP
Calibration: BetaCal4.20: HPD method: INTCAL20

Results are ISO/IEC-17025:2017 accredited. No sub-contracting or student labor was used in the analyses. All work was done at Beta in 4 in-house NEC accelerator mass spectrometers and 4 Thermo IRMSs. The "Conventional Radiocarbon Age" was calculated using the Libby half-life (5568 years), is corrected for total isotopic fraction and was used for calendar calibration where applicable. The Age is rounded to the nearest 10 years and is reported as radiocarbon years before present (BP), "present" = AD 1950. Results greater than the modern reference are reported as percent modern carbon (pMC). The modern reference standard was 95% the 14C signature of NIST SRM-4990C (oxalic acid). Quoted errors are 1 sigma counting statistics. Calculated sigmas less than 30 BP on the Conventional Radiocarbon Age are conservatively rounded up to 30. d13C values are on the material itself (not the AMS d13C). d13C and d15N values are relative to VPDB. References for calendar calibrations are cited at the bottom of calibration graph pages.

Calibration of Radiocarbon Age to Calendar Years

(High Probability Density Range Method (HPD): INTCAL20)

(Variables: d13C = -24.3 o/oo)

Laboratory number **Beta-612442**

Conventional radiocarbon age **4710 ± 30 BP**

95.4% probability

(54.8%)	3468 - 3373 cal BC	(5417 - 5322 cal BP)
(24.1%)	3534 - 3489 cal BC	(5483 - 5438 cal BP)
(14.9%)	3626 - 3576 cal BC	(5575 - 5525 cal BP)
(1.6%)	3571 - 3561 cal BC	(5520 - 5510 cal BP)

68.2% probability

(44.9%)	3439 - 3378 cal BC	(5388 - 5327 cal BP)
(21.1%)	3527 - 3496 cal BC	(5476 - 5445 cal BP)
(2.2%)	3451 - 3446 cal BC	(5400 - 5395 cal BP)

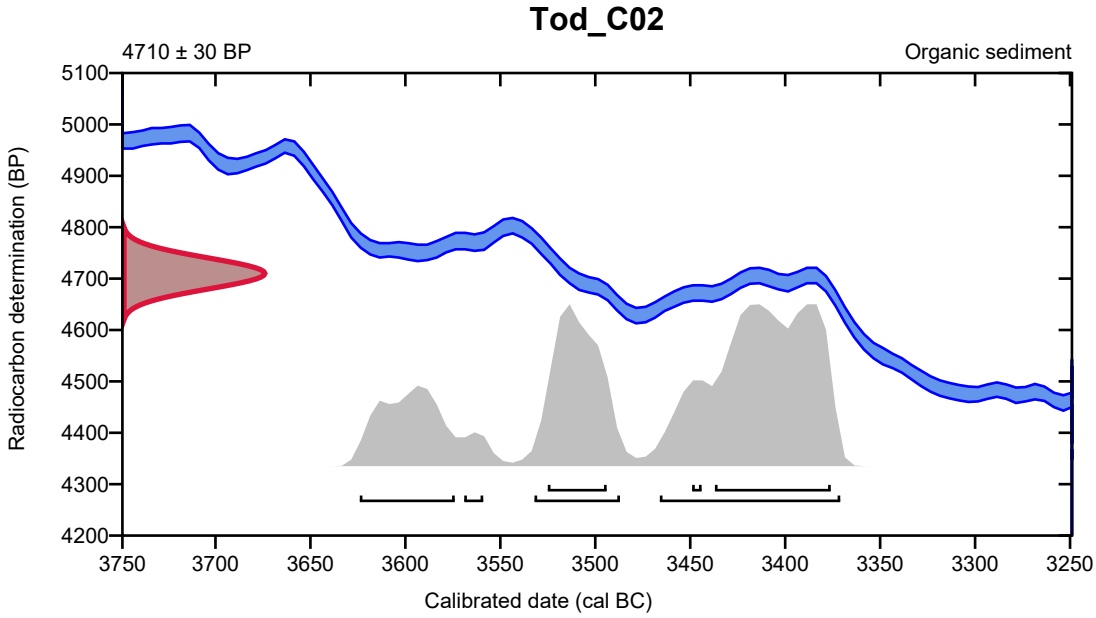

Database used

INTCAL20

References

References to Probability Method

Bronk Ramsey, C. (2009). Bayesian analysis of radiocarbon dates. Radiocarbon, 51(1), 337-360.

References to Database INTCAL20

Reimer, et al., 2020, Radiocarbon 62(4):725-757.

Beta Analytic, Inc.
4985 SW 74th Court
Miami, FL 33155 USA
Tel: 305-667-5167
Fax: 305-663-0964
info@betalabservices.com

ISO/IEC 17025:2017-Accredited Testing Laboratory

REPORT OF RADIOCARBON DATING ANALYSES

Paolo Boncio

Universita G.D Annunzio Chieti Pescara

Report Date: January 03, 2022

Material Received: December 09, 2021

Laboratory Number	Sample Code Number	Conventional Radiocarbon Age (BP) or Percent Modern Carbon (pMC) & Stable Isotopes	
Beta - 612443	**Tod_C03**	**2730 +/- 30 BP**	IRMS δ13C: -23.9 o/oo
(95.4%)	**928 - 810 cal BC**	**(2877 - 2759 cal BP)**	

Submitter Material: Organic Sediment/Gyttja
Pretreatment: (organic sediment) acid washes
Analyzed Material: Organic sediment
Analysis Service: AMS-Standard delivery
Percent Modern Carbon: 71.19 +/- 0.27 pMC
Fraction Modern Carbon: 0.7119 +/- 0.0027
D14C: -288.12 +/- 2.66 o/oo
Δ14C: -294.30 +/- 2.66 o/oo (1950:2022)
Measured Radiocarbon Age: (without d13C correction): 2710 +/- 30 BP
Calibration: BetaCal4.20: HPD method: INTCAL20

Results are ISO/IEC-17025:2017 accredited. No sub-contracting or student labor was used in the analyses. All work was done at Beta in 4 in-house NEC accelerator mass spectrometers and 4 Thermo IRMSs. The "Conventional Radiocarbon Age" was calculated using the Libby half-life (5568 years), is corrected for total isotopic fraction and was used for calendar calibration where applicable. The Age is rounded to the nearest 10 years and is reported as radiocarbon years before present (BP), "present" = AD 1950. Results greater than the modern reference are reported as percent modern carbon (pMC). The modern reference standard was 95% the 14C signature of NIST SRM-4990C (oxalic acid). Quoted errors are 1 sigma counting statistics. Calculated sigmas less than 30 BP on the Conventional Radiocarbon Age are conservatively rounded up to 30. d13C values are on the material itself (not the AMS d13C). d13C and d15N values are relative to VPDB. References for calendar calibrations are cited at the bottom of calibration graph pages.

Calibration of Radiocarbon Age to Calendar Years

(High Probability Density Range Method (HPD): INTCAL20)

(Variables: d13C = -23.9 o/oo)

Laboratory number **Beta-612443**

Conventional radiocarbon age **2730 ± 30 BP**

95.4% probability

(95.4%) 928 - 810 cal BC (2877 - 2759 cal BP)

68.2% probability

(68.2%) 900 - 831 cal BC (2849 - 2780 cal BP)

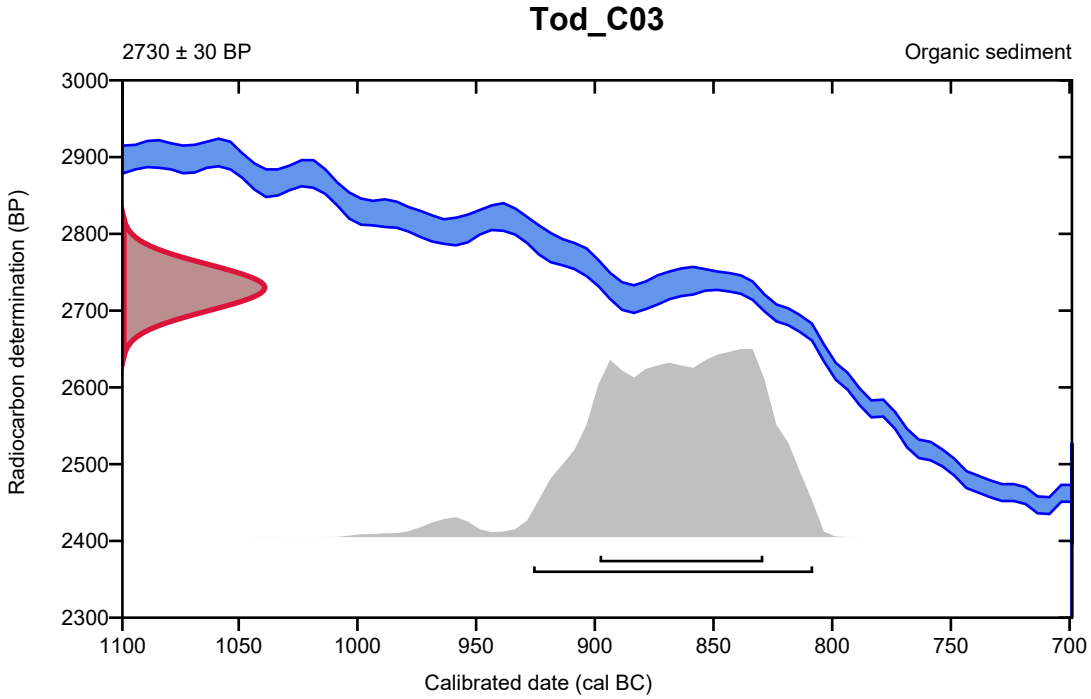

Database used

INTCAL20

References

References to Probability Method

Bronk Ramsey, C. (2009). Bayesian analysis of radiocarbon dates. Radiocarbon, 51(1), 337-360.

References to Database INTCAL20

Reimer, et al., 2020, Radiocarbon 62(4):725-757.

Beta Analytic, Inc.
4985 SW 74th Court
Miami, FL 33155 USA
Tel: 305-667-5167
Fax: 305-663-0964
info@betalabservices.com

ISO/IEC 17025:2017-Accredited Testing Laboratory

REPORT OF RADIOCARBON DATING ANALYSES

Paolo Boncio

Universita G.D Annunzio Chieti Pescara

Report Date: January 03, 2022

Material Received: December 09, 2021

Laboratory Number	Sample Code Number	Conventional Radiocarbon Age (BP) or Percent Modern Carbon (pMC) & Stable Isotopes	
Beta - 612444	**Tod_C04**	**300 +/- 30 BP**	IRMS δ13C: -24.9 o/oo

(69.3%)	**1495 - 1602 cal AD**	**(455 - 348 cal BP)**
(26.1%)	**1610 - 1656 cal AD**	**(340 - 294 cal BP)**

Submitter Material: Organic Sediment/Gyttja
Pretreatment: (organic sediment) acid washes
Analyzed Material: Organic sediment
Analysis Service: AMS-Standard delivery
Percent Modern Carbon: 96.33 +/- 0.36 pMC
Fraction Modern Carbon: 0.9633 +/- 0.0036
D14C: -36.66 +/- 3.60 o/oo
Δ14C: -45.01 +/- 3.60 o/oo (1950:2022)
Measured Radiocarbon Age: (without d13C correction): 300 +/- 30 BP
Calibration: BetaCal4.20: HPD method: INTCAL20

Results are ISO/IEC-17025:2017 accredited. No sub-contracting or student labor was used in the analyses. All work was done at Beta in 4 in-house NEC accelerator mass spectrometers and 4 Thermo IRMSs. The "Conventional Radiocarbon Age" was calculated using the Libby half-life (5568 years), is corrected for total isotopic fraction and was used for calendar calibration where applicable. The Age is rounded to the nearest 10 years and is reported as radiocarbon years before present (BP), "present" = AD 1950. Results greater than the modern reference are reported as percent modern carbon (pMC). The modern reference standard was 95% the 14C signature of NIST SRM-4990C (oxalic acid). Quoted errors are 1 sigma counting statistics. Calculated sigmas less than 30 BP on the Conventional Radiocarbon Age are conservatively rounded up to 30. d13C values are on the material itself (not the AMS d13C). d13C and d15N values are relative to VPDB. References for calendar calibrations are cited at the bottom of calibration graph pages.

Calibration of Radiocarbon Age to Calendar Years

(High Probability Density Range Method (HPD): INTCAL20)

(Variables: d13C = -24.9 o/oo)

Laboratory number **Beta-612444**

Conventional radiocarbon age **300 ± 30 BP**

95.4% probability

(69.3%)	1495 - 1602 cal AD	(455 - 348 cal BP)
(26.1%)	1610 - 1656 cal AD	(340 - 294 cal BP)

68.2% probability

(50.2%)	1521 - 1578 cal AD	(429 - 372 cal BP)
(18%)	1623 - 1645 cal AD	(327 - 305 cal BP)

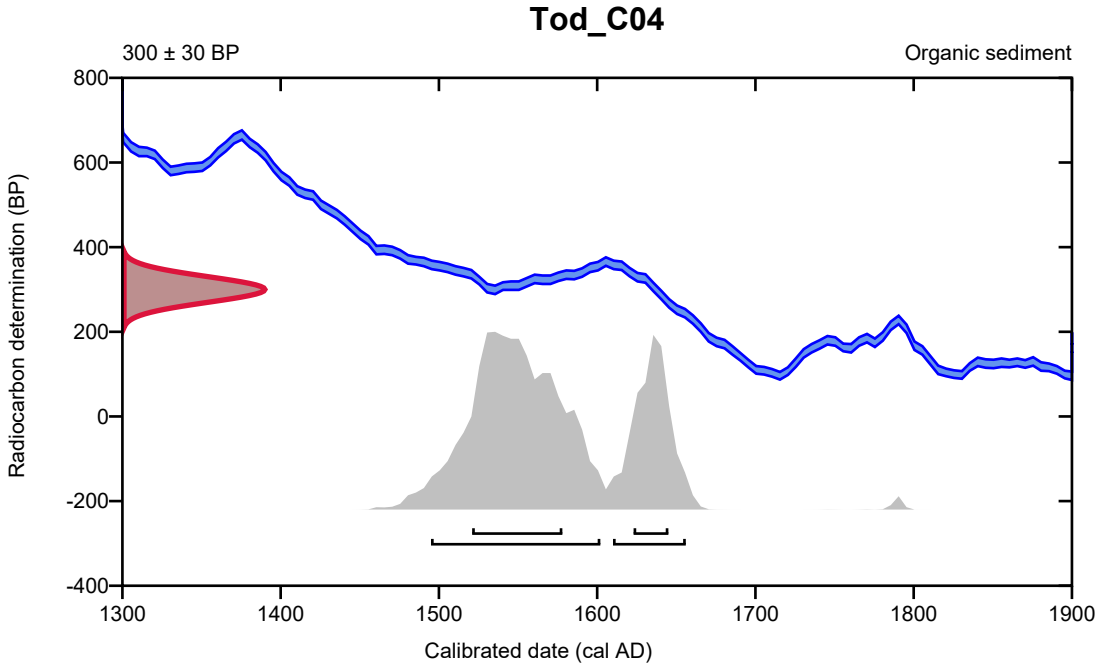

Database used

INTCAL20

References

References to Probability Method

Bronk Ramsey, C. (2009). Bayesian analysis of radiocarbon dates. Radiocarbon, 51(1), 337-360.

References to Database INTCAL20

Reimer, et al., 2020, Radiocarbon 62(4):725-757.

Beta Analytic, Inc.
4985 SW 74th Court
Miami, FL 33155 USA
Tel: 305-667-5167
Fax: 305-663-0964
info@betalabservices.com

ISO/IEC 17025:2017-Accredited Testing Laboratory

REPORT OF RADIOCARBON DATING ANALYSES

Paolo Boncio

Universita G.D Annunzio Chieti Pescara

Report Date: January 03, 2022

Material Received: December 09, 2021

Laboratory Number	Sample Code Number	Conventional Radiocarbon Age (BP) or Percent Modern Carbon (pMC) & Stable Isotopes	
Beta - 612445	**Tod_C05**	**470 +/- 30 BP**	IRMS δ13C: -24.3 o/oo
(95.4%)	**1408 - 1460 cal AD**	**(542 - 490 cal BP)**	

Submitter Material: Organic Sediment/Gyttja
Pretreatment: (organic sediment) acid washes
Analyzed Material: Organic sediment
Analysis Service: AMS-Standard delivery
Percent Modern Carbon: 94.32 +/- 0.35 pMC
Fraction Modern Carbon: 0.9432 +/- 0.0035
D14C: -56.83 +/- 3.52 o/oo
Δ14C: -65.01 +/- 3.52 o/oo (1950:2022)
Measured Radiocarbon Age: (without d13C correction): 460 +/- 30 BP
Calibration: BetaCal4.20: HPD method: INTCAL20

Results are ISO/IEC-17025:2017 accredited. No sub-contracting or student labor was used in the analyses. All work was done at Beta in 4 in-house NEC accelerator mass spectrometers and 4 Thermo IRMSs. The "Conventional Radiocarbon Age" was calculated using the Libby half-life (5568 years), is corrected for total isotopic fraction and was used for calendar calibration where applicable. The Age is rounded to the nearest 10 years and is reported as radiocarbon years before present (BP), "present" = AD 1950. Results greater than the modern reference are reported as percent modern carbon (pMC). The modern reference standard was 95% the 14C signature of NIST SRM-4990C (oxalic acid). Quoted errors are 1 sigma counting statistics. Calculated sigmas less than 30 BP on the Conventional Radiocarbon Age are conservatively rounded up to 30. d13C values are on the material itself (not the AMS d13C). d13C and d15N values are relative to VPDB. References for calendar calibrations are cited at the bottom of calibration graph pages.

BetaCal 4.20

Calibration of Radiocarbon Age to Calendar Years

(High Probability Density Range Method (HPD): INTCAL20)

(Variables: d13C = -24.3 o/oo)

Laboratory number **Beta-612445**

Conventional radiocarbon age **470 ± 30 BP**

95.4% probability

(95.4%) 1408 - 1460 cal AD (542 - 490 cal BP)

68.2% probability

(68.2%) 1424 - 1448 cal AD (526 - 502 cal BP)

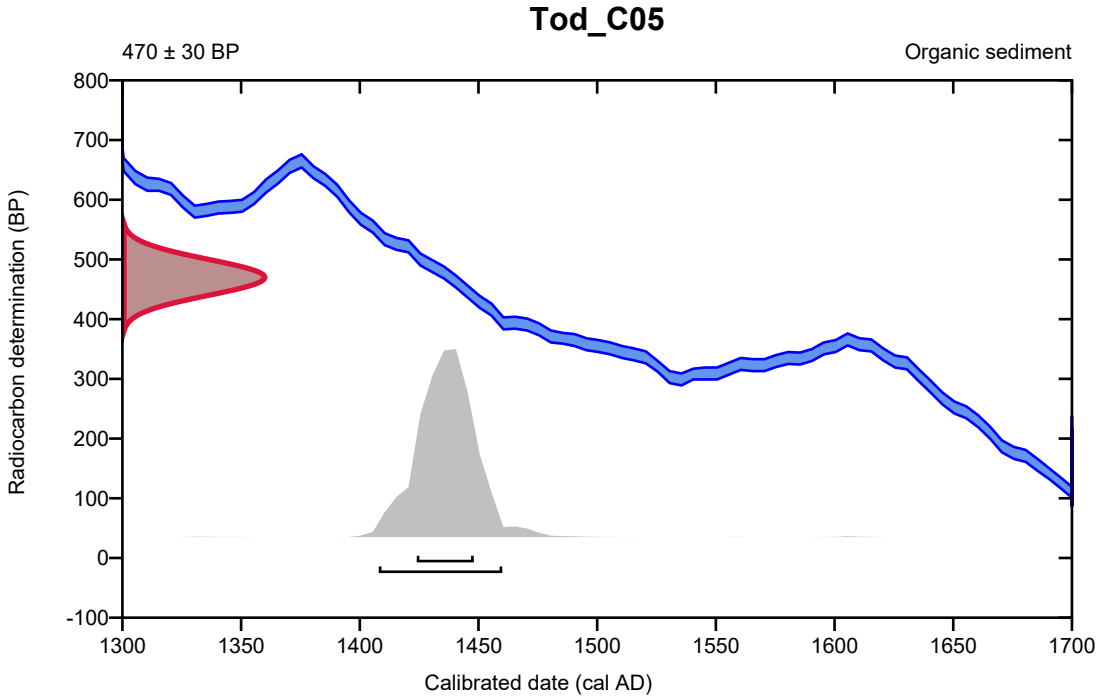

Database used

INTCAL20

References

References to Probability Method

Bronk Ramsey, C. (2009). Bayesian analysis of radiocarbon dates. Radiocarbon, 51(1), 337-360.

References to Database INTCAL20

Reimer, et al., 2020, Radiocarbon 62(4):725-757.

Beta Analytic Radiocarbon Dating Laboratory

4985 S.W. 74th Court, Miami, Florida 33155 • Tel: (305)667-5167 • Fax: (305)663-0964 • Email: beta@radiocarbon.com

Beta Analytic, Inc.
4985 SW 74th Court
Miami, FL 33155 USA
Tel: 305-667-5167
Fax: 305-663-0964
info@betalabservices.com

ISO/IEC 17025:2017-Accredited Testing Laboratory

REPORT OF RADIOCARBON DATING ANALYSES

Paolo Boncio

Universita G.D Annunzio Chieti Pescara

Report Date: August 24, 2022

Material Received: August 04, 2022

Laboratory Number	Sample Code Number	Conventional Radiocarbon Age (BP) or Percent Modern Carbon (pMC) & Stable Isotopes	
Beta - 635171	**Tod_C06**	**1260 +/- 30 BP**	IRMS δ13C: -24.4 o/oo
(73.9%)	**668 - 776 cal AD**	**(1282 - 1174 cal BP)**	
(17.8%)	**786 - 830 cal AD**	**(1164 - 1120 cal BP)**	
(3.8%)	**853 - 874 cal AD**	**(1097 - 1076 cal BP)**	

Submitter Material: Organic Sediment/Gyttja
Pretreatment: (organic sediment) acid washes
Analyzed Material: Organic sediment
Analysis Service: AMS-Standard delivery
Percent Modern Carbon: 85.48 +/- 0.32 pMC
Fraction Modern Carbon: 0.8548 +/- 0.0032
D14C: -145.17 +/- 3.19 o/oo
Δ14C: -152.58 +/- 3.19 o/oo (1950:2022)
Measured Radiocarbon Age: (without d13C correction): 1250 +/- 30 BP
Calibration: BetaCal4.20: HPD method: INTCAL20

Results are ISO/IEC-17025:2017 accredited. No sub-contracting or student labor was used in the analyses. All work was done at Beta in 4 in-house NEC accelerator mass spectrometers and 4 Thermo IRMSs. The "Conventional Radiocarbon Age" was calculated using the Libby half-life (5568 years), is corrected for total isotopic fraction and was used for calendar calibration where applicable. The Age is rounded to the nearest 10 years and is reported as radiocarbon years before present (BP), "present" = AD 1950. Results greater than the modern reference are reported as percent modern carbon (pMC). The modern reference standard was 95% the 14C signature of NIST SRM-4990C (oxalic acid). Quoted errors are 1 sigma counting statistics. Calculated sigmas less than 30 BP on the Conventional Radiocarbon Age are conservatively rounded up to 30. d13C values are on the material itself (not the AMS d13C). d13C and d15N values are relative to VPDB. References for calendar calibrations are cited at the bottom of calibration graph pages.

Calibration of Radiocarbon Age to Calendar Years

(High Probability Density Range Method (HPD): INTCAL20)

(Variables: d13C = -24.4 o/oo)

Laboratory number **Beta-635171**

Conventional radiocarbon age **1260 ± 30 BP**

95.4% probability

(73.9%)	668 - 776 cal AD	(1282 - 1174 cal BP)
(17.8%)	786 - 830 cal AD	(1164 - 1120 cal BP)
(3.8%)	853 - 874 cal AD	(1097 - 1076 cal BP)

68.2% probability

(59.4%)	680 - 746 cal AD	(1270 - 1204 cal BP)
(6.2%)	758 - 768 cal AD	(1192 - 1182 cal BP)
(2.6%)	793 - 798 cal AD	(1157 - 1152 cal BP)

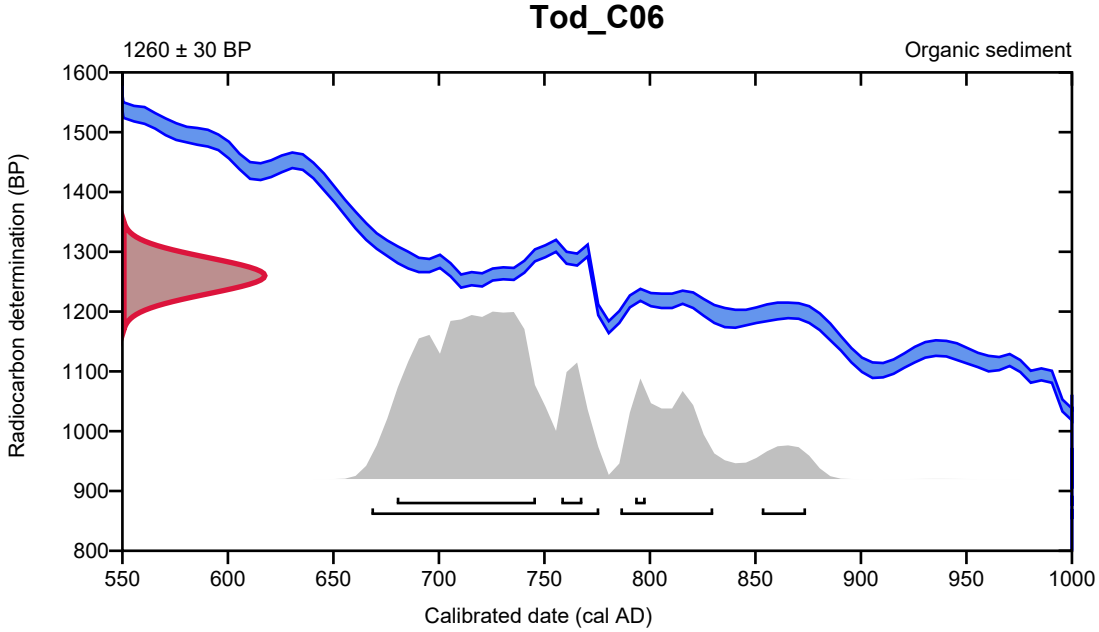

Database used

INTCAL20

References

References to Probability Method

Bronk Ramsey, C. (2009). Bayesian analysis of radiocarbon dates. Radiocarbon, 51(1), 337-360.

References to Database INTCAL20

Reimer, et al., 2020, Radiocarbon 62(4):725-757.

Beta Analytic Radiocarbon Dating Laboratory

4985 S.W. 74th Court, Miami, Florida 33155 • Tel: (305)667-5167 • Fax: (305)663-0964 • Email: beta@radiocarbon.com

Beta Analytic, Inc.
4985 SW 74th Court
Miami, FL 33155 USA
Tel: 305-667-5167
Fax: 305-663-0964
info@betalabservices.com

ISO/IEC 17025:2017-Accredited Testing Laboratory

Quality Assurance Report

This report provides the results of reference materials used to validate radiocarbon analyses prior to reporting. Known-value reference materials were analyzed quasi-simultaneously with the unknowns. Results are reported as expected values vs measured values. Reported values are calculated relative to NISTSRM-1990C and corrected for isotopic fractionation. Results are reported using the direct analytical measure percent modern carbon (pMC) with one relative standard deviation. Agreement between expected and measured values is taken as being within 2 sigma agreement (error x 2) to account for total laboratory error.

Report Date: January 03, 2022
Submitter: Prof. Paolo Boncio

QA MEASUREMENTS

Reference 1	
Expected Value:	0.42 +/- 0.04 pMC
Measured Value:	0.42 +/- 0.03 pMC
Agreement:	Accepted
Reference 2	
Expected Value:	129.41 +/- 0.06 pMC
Measured Value:	129.43 +/- 0.35 pMC
Agreement:	Accepted
Reference 3	
Expected Value:	96.69 +/- 0.50 pMC
Measured Value:	96.63 +/- 0.28 pMC
Agreement:	Accepted

COMMENT: All measurements passed acceptance tests.

Validation: Chris Patrick
Digital signature on file

Date: January 03, 2022

Beta Analytic, Inc.
4985 SW 74th Court
Miami, FL 33155 USA
Tel: 305-667-5167
Fax: 305-663-0964
info@betalabservices.com

ISO/IEC 17025:2017-Accredited Testing Laboratory

REPORT OF RADIOCARBON DATING ANALYSES

Paolo Boncio

Universita G.D Annunzio Chieti Pescara

Report Date: May 16, 2022

Material Received: May 02, 2022

Laboratory Number	Sample Code Number	Conventional Radiocarbon Age (BP) or Percent Modern Carbon (pMC) & Stable Isotopes	
Beta - 626364	**VS_C01**	**20600 +/- 70 BP**	IRMS δ13C: -23.6 o/oo

(95.4%) 23126 - 22626 cal BC (25075 - 24575 cal BP)

Submitter Material: Organic Sediment/Gyttja
Pretreatment: (organic sediment) acid washes
Analyzed Material: Organic sediment
Analysis Service: AMS-Standard delivery
Percent Modern Carbon: 7.70 +/- 0.07 pMC
Fraction Modern Carbon: 0.0770 +/- 0.0007
D14C: -923.04 +/- 0.67 o/oo
Δ14C: -923.71 +/- 0.67 o/oo (1950:2022)
Measured Radiocarbon Age: (without d13C correction): 20580 +/- 70 BP
Calibration: BetaCal4.20: HPD method: INTCAL20

Results are ISO/IEC-17025:2017 accredited. No sub-contracting or student labor was used in the analyses. All work was done at Beta in 4 in-house NEC accelerator mass spectrometers and 4 Thermo IRMSs. The "Conventional Radiocarbon Age" was calculated using the Libby half-life (5568 years), is corrected for total isotopic fraction and was used for calendar calibration where applicable. The Age is rounded to the nearest 10 years and is reported as radiocarbon years before present (BP), "present" = AD 1950. Results greater than the modern reference are reported as percent modern carbon (pMC). The modern reference standard was 95% the 14C signature of NIST SRM-4990C (oxalic acid). Quoted errors are 1 sigma counting statistics. Calculated sigmas less than 30 BP on the Conventional Radiocarbon Age are conservatively rounded up to 30. d13C values are on the material itself (not the AMS d13C). d13C and d15N values are relative to VPDB. References for calendar calibrations are cited at the bottom of calibration graph pages.

Calibration of Radiocarbon Age to Calendar Years

(High Probability Density Range Method (HPD): INTCAL20)

(Variables: d13C = -23.6 o/oo)

Laboratory number **Beta-626364**

Conventional radiocarbon age **20600 ± 70 BP**

95.4% probability

(95.4%) 23126 - 22626 cal BC (25075 - 24575 cal BP)

68.2% probability

(68.2%) 23011 - 22746 cal BC (24960 - 24695 cal BP)

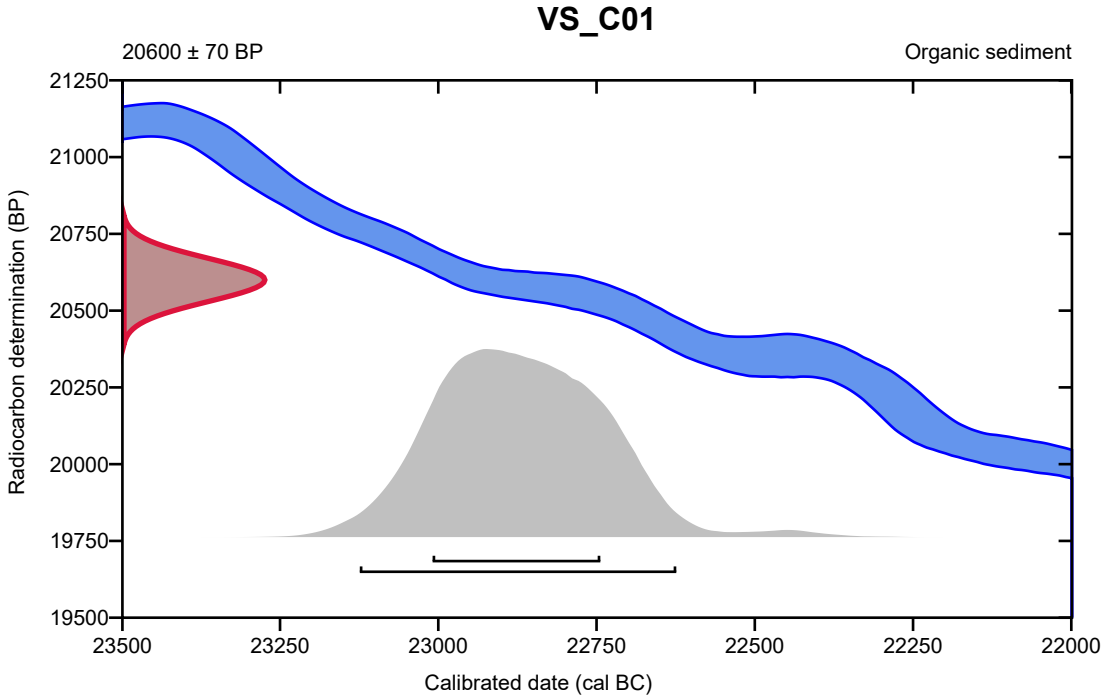

Database used

INTCAL20

References

References to Probability Method

Bronk Ramsey, C. (2009). Bayesian analysis of radiocarbon dates. Radiocarbon, 51(1), 337-360.

References to Database INTCAL20

Reimer, et al., 2020, Radiocarbon 62(4):725-757.

Beta Analytic, Inc.
4985 SW 74th Court
Miami, FL 33155 USA
Tel: 305-667-5167
Fax: 305-663-0964
info@betalabservices.com

ISO/IEC 17025:2017-Accredited Testing Laboratory

REPORT OF RADIOCARBON DATING ANALYSES

Paolo Boncio

Universita G.D Annunzio Chieti Pescara

Report Date: May 16, 2022

Material Received: May 02, 2022

Laboratory Number	Sample Code Number	Conventional Radiocarbon Age (BP) or Percent Modern Carbon (pMC) & Stable Isotopes	
Beta - 626365	**VS_C12**	**11910 +/- 40 BP**	IRMS δ13C: -23.6 o/oo

(82.0%)	**11864 - 11656 cal BC**	**(13813 - 13605 cal BP)**
(10.7%)	**12054 - 11991 cal BC**	**(14003 - 13940 cal BP)**
(2.7%)	**11908 - 11882 cal BC**	**(13857 - 13831 cal BP)**

Submitter Material: Organic Sediment/Gyttja
Pretreatment: (organic sediment) acid washes
Analyzed Material: Organic sediment
Analysis Service: AMS-Standard delivery
Percent Modern Carbon: 22.70 +/- 0.11 pMC
Fraction Modern Carbon: 0.2270 +/- 0.0011
D14C: -772.96 +/- 1.13 o/oo
Δ14C: -774.93 +/- 1.13 o/oo (1950:2022)
Measured Radiocarbon Age: (without d13C correction): 11890 +/- 40 BP
Calibration: BetaCal4.20: HPD method: INTCAL20

Results are ISO/IEC-17025:2017 accredited. No sub-contracting or student labor was used in the analyses. All work was done at Beta in 4 in-house NEC accelerator mass spectrometers and 4 Thermo IRMSs. The "Conventional Radiocarbon Age" was calculated using the Libby half-life (5568 years), is corrected for total isotopic fraction and was used for calendar calibration where applicable. The Age is rounded to the nearest 10 years and is reported as radiocarbon years before present (BP), "present" = AD 1950. Results greater than the modern reference are reported as percent modern carbon (pMC). The modern reference standard was 95% the 14C signature of NIST SRM-4990C (oxalic acid). Quoted errors are 1 sigma counting statistics. Calculated sigmas less than 30 BP on the Conventional Radiocarbon Age are conservatively rounded up to 30. d13C values are on the material itself (not the AMS d13C). d13C and d15N values are relative to VPDB. References for calendar calibrations are cited at the bottom of calibration graph pages.

Calibration of Radiocarbon Age to Calendar Years

(High Probability Density Range Method (HPD): INTCAL20)

(Variables: d13C = -23.6 o/oo)

Laboratory number **Beta-626365**

Conventional radiocarbon age **11910 ± 40 BP**

95.4% probability

(82%)	11864 - 11656 cal BC	(13813 - 13605 cal BP)
(10.7%)	12054 - 11991 cal BC	(14003 - 13940 cal BP)
(2.7%)	11908 - 11882 cal BC	(13857 - 13831 cal BP)

68.2% probability

(46.2%)	11855 - 11795 cal BC	(13804 - 13744 cal BP)
(15.5%)	11753 - 11709 cal BC	(13702 - 13658 cal BP)
(6.5%)	11680 - 11663 cal BC	(13629 - 13612 cal BP)

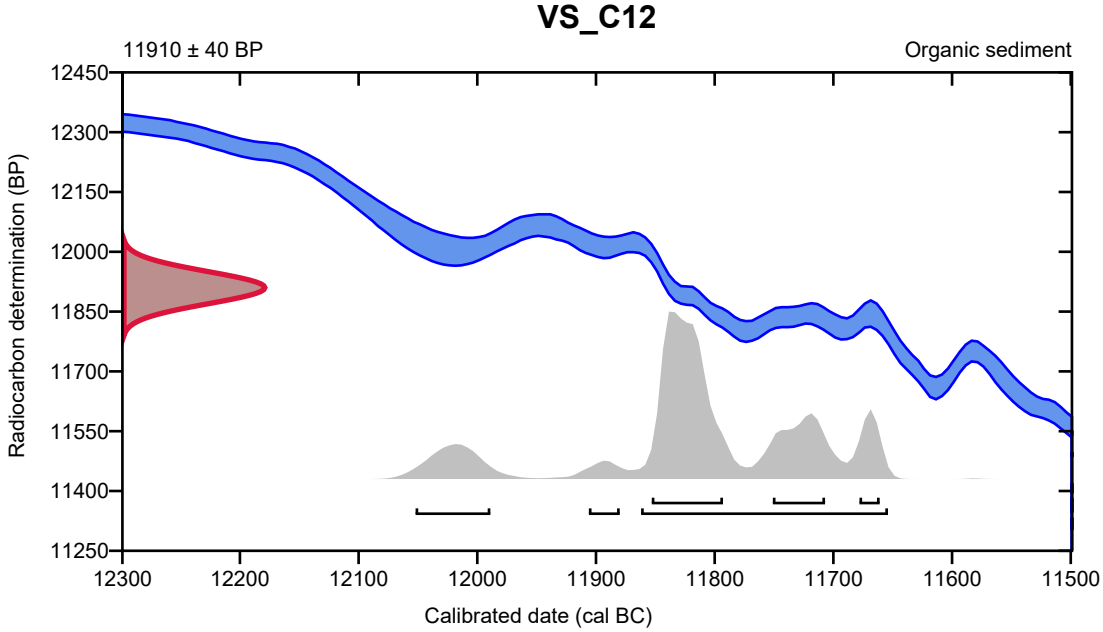

Database used

INTCAL20

References

References to Probability Method

Bronk Ramsey, C. (2009). Bayesian analysis of radiocarbon dates. Radiocarbon, 51(1), 337-360.

References to Database INTCAL20

Reimer, et al., 2020, Radiocarbon 62(4):725-757.

Beta Analytic, Inc.
4985 SW 74th Court
Miami, FL 33155 USA
Tel: 305-667-5167
Fax: 305-663-0964
info@betalabservices.com

ISO/IEC 17025:2017-Accredited Testing Laboratory

REPORT OF RADIOCARBON DATING ANALYSES

Paolo Boncio

Universita G.D Annunzio Chieti Pescara

Report Date: May 16, 2022

Material Received: May 02, 2022

Laboratory Number	Sample Code Number	Conventional Radiocarbon Age (BP) or Percent Modern Carbon (pMC) & Stable Isotopes	
Beta - 626366	**VS_C13**	**12940 +/- 40 BP**	IRMS δ13C: -23.0 o/oo

(95.4%) 13677 - 13351 cal BC (15626 - 15300 cal BP)

Submitter Material: Organic Sediment/Gyttja
Pretreatment: (organic sediment) acid washes
Analyzed Material: Organic sediment
Analysis Service: AMS-Standard delivery
Percent Modern Carbon: 19.97 +/- 0.10 pMC
Fraction Modern Carbon: 0.1997 +/- 0.0010
D14C: -800.29 +/- 0.99 o/oo
Δ14C: -802.02 +/- 0.99 o/oo (1950:2022)
Measured Radiocarbon Age: (without d13C correction): 12910 +/- 40 BP
Calibration: BetaCal4.20: HPD method: INTCAL20

Results are ISO/IEC-17025:2017 accredited. No sub-contracting or student labor was used in the analyses. All work was done at Beta in 4 in-house NEC accelerator mass spectrometers and 4 Thermo IRMSs. The "Conventional Radiocarbon Age" was calculated using the Libby half-life (5568 years), is corrected for total isotopic fraction and was used for calendar calibration where applicable. The Age is rounded to the nearest 10 years and is reported as radiocarbon years before present (BP), "present" = AD 1950. Results greater than the modern reference are reported as percent modern carbon (pMC). The modern reference standard was 95% the 14C signature of NIST SRM-4990C (oxalic acid). Quoted errors are 1 sigma counting statistics. Calculated sigmas less than 30 BP on the Conventional Radiocarbon Age are conservatively rounded up to 30. d13C values are on the material itself (not the AMS d13C). d13C and d15N values are relative to VPDB. References for calendar calibrations are cited at the bottom of calibration graph pages.

Calibration of Radiocarbon Age to Calendar Years

(High Probability Density Range Method (HPD): INTCAL20)

(Variables: d13C = -23.0 o/oo)

Laboratory number **Beta-626366**

Conventional radiocarbon age **12940 ± 40 BP**

95.4% probability

(95.4%) 13677 - 13351 cal BC (15626 - 15300 cal BP)

68.2% probability

(68.2%) 13619 - 13428 cal BC (15568 - 15377 cal BP)

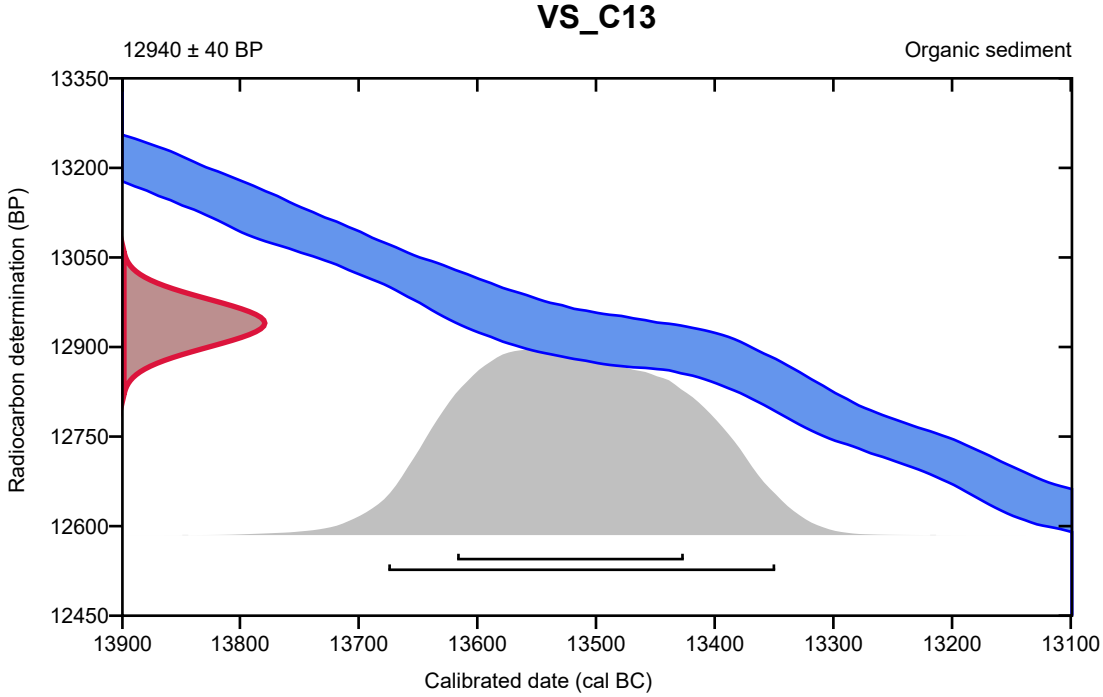

Database used

INTCAL20

References

References to Probability Method

Bronk Ramsey, C. (2009). Bayesian analysis of radiocarbon dates. Radiocarbon, 51(1), 337-360.

References to Database INTCAL20

Reimer, et al., 2020, Radiocarbon 62(4):725-757.

Beta Analytic Radiocarbon Dating Laboratory

4985 S.W. 74th Court, Miami, Florida 33155 • Tel: (305)667-5167 • Fax: (305)663-0964 • Email: beta@radiocarbon.com

Beta Analytic, Inc.
4985 SW 74th Court
Miami, FL 33155 USA
Tel: 305-667-5167
Fax: 305-663-0964
info@betalabservices.com

ISO/IEC 17025:2017-Accredited Testing Laboratory

Quality Assurance Report

This report provides the results of reference materials used to validate radiocarbon analyses prior to reporting. Known-value reference materials were analyzed quasi-simultaneously with the unknowns. Results are reported as expected values vs measured values. Reported values are calculated relative to NISTSRM-1990C and corrected for isotopic fractionation. Results are reported using the direct analytical measure percent modern carbon (pMC) with one relative standard deviation. Agreement between expected and measured values is taken as being within 2 sigma agreement (error x 2) to account for total laboratory error.

Report Date: May 16, 2022
Submitter: Prof. Paolo Boncio

QA MEASUREMENTS

Reference 1	
Expected Value:	129.41 +/- 0.06 pMC
Measured Value:	129.43 +/- 0.37 pMC
Agreement:	Accepted
Reference 2	
Expected Value:	96.69 +/- 0.50 pMC
Measured Value:	96.78 +/- 0.29 pMC
Agreement:	Accepted
Reference 3	
Expected Value:	0.42 +/- 0.04 pMC
Measured Value:	0.42 +/- 0.04 pMC
Agreement:	Accepted

COMMENT: All measurements passed acceptance tests.

Validation: Chris Patrick
Digital signature on file

Date: May 16, 2022

Plateforme Nationale LMC14

CEA Saclay - Bât. 450 - Porte 4E - 91191 GIF sur YVETTE Cedex

Série : Baize220110 - Demandeur : BAIZE Stéphane - Nombre : 5

Numéro	Référence	Nature	mg C	Delta C13	pMC *	Âge BP	
SacA65888	VS_C02	bulk	1.07	-23.6	19.31 ± 0.148	13210 ± 60	
SacA65889	VS_C03	bulk	0.98	-23.9	16.789 ± 0.145	14330 ± 70	
SacA65890	VS_C06bis	bulk	1.07	-25.8	49.498 ± 0.201	5650 ± 35	
SacA65891	VS_C07	bulk	1.66	-24.4	78.048 ± 0.21	1990 ± 30	
SacA65892	VS_C08	bulk	1.09	-19.1	51.5 ± 0.18	5330 ± 30	

*** Corrigé du fractionnement**

Blanc soustrait *Sans blanc soustrait*

Blanc	Echantillon moderne	Indiscernable du bruit de fond	Age apparent
Echec au Traitement ou à la Mesure	Echantillon refait		

Contact administratif : **Valérie SETTI**

Tél : 01 69 08 14 60 - Fax : 01 69 08 15 17

@ : valerie.setti@cea.fr

Contact scientifique : **Christophe MOREAU**

Tél : 01 69 08 14 05

@ : christophe-r.moreau@cea.fr

Calibration of the uncalibrated ages of the samplse analysed by the Laboratory Plateforme Nationale LMC14 (France) using OxCal v4.4 (Bronk Ramsey 2021) and the IntCal20 atmospheric calibration model (Reimer et al, 2020)

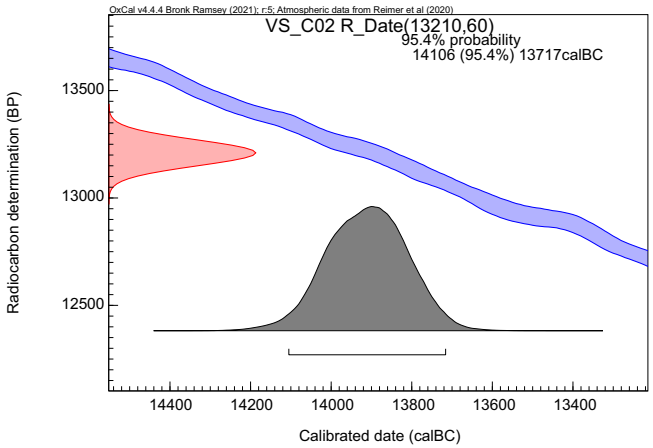

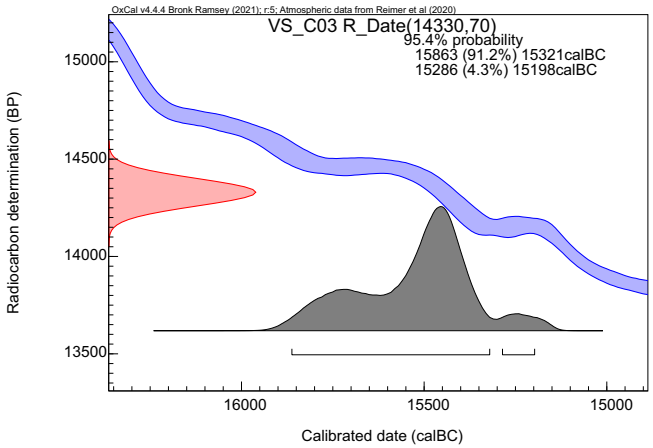

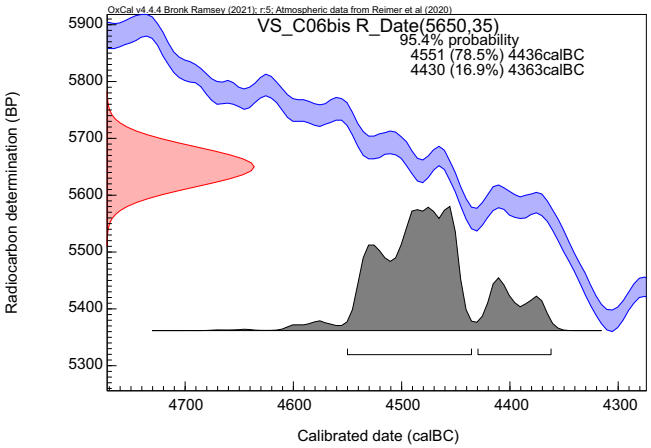

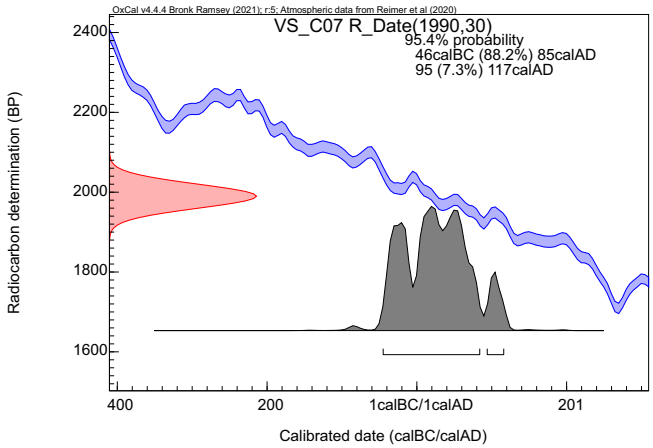

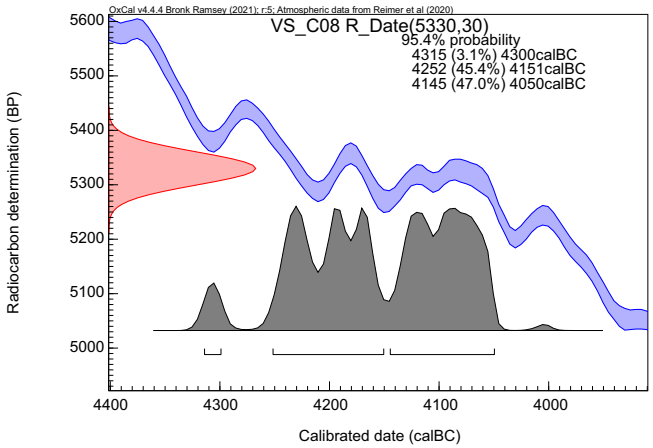

Name	Conventional Age (BP)	Calibrated Age (BC/AD)
VS_C02	13210 ± 60	14106 - 13717 BC (95.4%)
VS_C03	14330 ± 70	15863 - 15321 BC (91.2%) 15286 - 15198 BC (4.3%)
VS_C06bis	5650 ± 35	4551 - 4436 BC (78.5%) 4430 - 4363 BC (16.9%)
VS_C07	1990 ± 30	46 - 85 AD (88.2%) 95 - 117 AD (7.3%)
VS_C08	5330 ± 30	4315 - 4300 BC (3.1%) 4252 - 4151 BC (45.4%) 4145 - 4050 BC (47%)